

2-P (MIX)

N74-28003

NASA TECHNICAL TRANSLATION

NASA TT F 15,535

SPACE STUDIES IN THE UKRAINE

No. 1

SPACE MATERIALS STUDIES AND TECHNOLOGY

G. S. Pisarenko

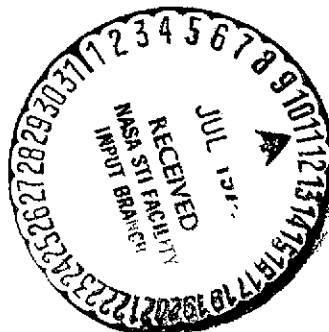
Editor

Translation of "Kosmicheskiye issledovaniya na Ukraine, Vypusk 1, Kosmicheskoye materialovedeniye i tekhnologiya," Kiev, "Naukova Dumka" Publisher, 1973, 104 pp.

(NASA-TT-F-15535) SPACE STUDIES IN THE
UKRAINE. NUMBER 1: SPACE MATERIALS
STUDIES AND TECHNOLOGY (Scientific
Translation Service) 207 p HC \$13.50

N74-28003
THRU
N74-28019
Unclass
42009

CSCL 11D G3/18



NATIONAL AERONAUTICS AND SPACE ADMINISTRATION
WASHINGTON, D. C. 20546 JUNE 1974

207

1. Report No. NASA TT F-15,535		2. Government Accession No.		3. Recipient's Catalog No.	
4. Title and Subtitle SPACE STUDIES IN THE UKRAINE No. 1. SPACE MATERIALS STUDIES AND TECHNOLOGY				5. Report Date June, 1974	
				6. Performing Organization Code	
7. Author(s) G.S. Pisarenko, Editor				8. Performing Organization Report No.	
				10. Work Unit No.	
9. Performing Organization Name and Address SCITRAN Box 5456 Santa Barbara, CA 93108				11. Contract or Grant No. NASw-2483	
				13. Type of Report and Period Covered Translation	
12. Sponsoring Agency Name and Address National Aeronautics and Space Administration Washington, D.C. 20546				14. Sponsoring Agency Code	
15. Supplementary Notes Translation of "Kosmicheskoye issledovaniye na Ukraine, Vypusk 1, Kosmicheskoye materialovedeniye i tekhnologiya", Kiev, "Naukova Dumka" Publisher, 1973, 104 pp.					
16. Abstract This volume presents results of studies of the physical and mechanical properties of constructional materials in vacuum at low and high temperatures. The peculiarities of the processes of friction and wear, metal failure under short-term static and long-term alternating loads in conditions similar to those of space are examined. Equipment is described which makes it possible to carry out the technological operations of metal melting welding, brazing, and vacuum deposition under conditions simulating space. The problems of unsteady heat transport and heat transfer for bodies of different shape in space are solved. These solutions may be used for thermal and strength calculations of spacecraft structure and thermal protection.					
17. Key Words (Selected by Author(s))				18. Distribution Statement Unclassified - Unlimited	
19. Security Classif. (of this report) Unclassified		20. Security Classif. (of this page) Unclassified		21. No. of Pages 207	
				22. Price	

ANNOTATION

This volume presents results of studies of the physical and mechanical properties of constructional materials in vacuum at low and high temperatures. We examine the peculiarities of the processes of friction and wear, metal failure under short-term static and long-term alternating loads in conditions similar to those of space. Equipment is described which makes it possible to carry out the technological operations of metal melting welding, brazing, and vacuum deposition under conditions simulating space. We solve the problems of unsteady heat transport and heat transfer for bodies of different shape in space; these solutions may be used for thermal and strength calculations of spacecraft structure and thermal protection.

While directed toward scientists, the volume may be useful to engineers and technicians, designers, and also students in the upper divisions.

FROM THE EDITORS

The study and development of regions of the Universe near the Earth and those more distant is one of the urgent modern problems of natural science. The new information on the structure and properties of space surrounding the Earth which has been obtained by automatic and manned vehicles is expanding the theoretical basis for material production, facilitating more complete development of the riches of nature, and advancing many fields of science and engineering. Space studies are contributing to the improvement of global communications and telecommunication facilities. The creation of the means for conquest of space leads to the necessity for carrying out a broad range of studies and improving industrial production. The creation of orbital space labs and vehicles for landing on the Moon, Venus, and Mars required the development of a highly diversified industry and the practical application of all the latest achievements of mechanics, materials science, and electronics. Launching of crews into space voyages lasting several days stimulated the development of biology and medicine.

Space studies are complex operations in regard to technique and methodology and require integration of the efforts of scientists of various specialities — physicists, chemists, mechanicians, astronmers, biologists, doctors, and so on. Extensive work in this field is being carried out in the Ukraine. Research on integrated study of the properties of space matter and the magnetic, radiation, and thermal fields and processes in the universe are being carried out at the Academy of Sciences of the UkSSR, in the departments and laboratories of the universities, and in various scientific and engineering organizations.

Studies are being made of the behavior of various substances and materials, the efficiency of mechanisms and instruments, the life activity of organisms subjected to weightlessness, active media, and superlow temperatures. New equipment is being developed for space studies and remote and direct measurement methods are being evolved. The data obtained as a result of theoretical and experimental studies are analyzed, new relationships are identified, and the directions for further study are determined.

The Commission on Space Studies of the Academy of Sciences of the UkSSR was created in 1968 to correlate space study activities in the Ukraine, coordinate the activity of the institutes, universities, departments, laboratories, and individual specialists in order to resolve the most urgent problems. This commission included the leading scientists and specialists. The commission has correlated space study activities in the Ukraine and gathered data concerning the direction and results of solution of important individual problems. This commission cooperates closely with the Commission on Study and Use of Outer Space of the Academy of Sciences of the USSR, the Intercosmos Commission, and the Institute of Space Problems of the Academy of Sciences of the USSR.

The present volume presents, in a systematized format, the most interesting and scientifically practically important results of recent studies in astrophysics, geophysics, heliophysics, space mechanics and control systems, radioastronomy, space materials science, and thermophysics performed in the scientific establishments of the Ukraine.

The first volumes of the collection include studies devoted to theoretical questions of the spacecraft dynamics and spacecraft navigation and control. The peculiarities of the physical

and chemical properties of metals in vacuum at superlow temperatures are examined. Important articles are devoted to questions of space technology — metal melting, welding, and vacuum deposition, and metal casting under weightlessness and high vacuum conditions. The thermophysics of the processes of spacecraft interaction with the surrounding medium is investigated. Methods are developed for calculating the hydrodynamic and heat exchange processes which take place during filling, pressurizing, and emptying of cryogenic vessels. The questions of radiative heating and cooling under space conditions and calculation of the thermal stresses in spacecraft structures are examined.

Several articles cover the study of solar-terrestrial relationships and heliophysics and radiophysical study of space near the Earth. A general survey is given of the activity of the astronomical observatory of Kharkov State University, the leading center of planetary astrophysics in the Soviet Union.

The studies on space biology and medicine published here are of considerable interest. These studies examine the extremal effects on the human organism of factors encountered in space flight and investigate the possibilities for water conservation and regeneration and algae cultivation in closed systems.

Beginning with the first volume and continuing in the future, we intend to publish articles in individual thematic volumes directed toward a definite circle of specialists. The articles on space studies in the Ukraine published in 1973 have been combined into four thematic volumes: Space Material Science and Technology, Space Mechanics and Control Systems, Space Physics and Astronomy, and Space Biology and Medicine.

The volumes will be published systematically in the future as more data are accumulated.

The Commission on Space Studies of the AS UkSSR and the editorial board of the collection "Space Studies in the Ukraine" believe that the data being published will aid in improving the coordination of scientific studies in space and will also inform scientific and industrial personnel and all specialists interested in questions of outer space development on the trends and results of studies conducted in this important scientific field.

— G. S. Pisarenko, Academician of the AS UkSSR

TABLE OF CONTENTS

	Page
ANNOTATION	iii
FROM THE EDITORS	iv
B. Ye. Paton, V. Ye. Paton, D. A. Dudko, V. N. Bernadskiy, G. P. Dubenko, V. F. Lapchinskiy, V. V. Stesin, A. A. Zagrebel'nyy, Yu. N. Lankin, Yu. A. Masalov, O. S. Tsygankov, V. M. Boychuk STAND FOR STUDYING TECHNOLOGICAL PROCESSES UNDER CONDITIONS SIMULATING SPACE	1 ✓
V. S. Dvernyakov, I. N. Frantsevich, V. V. Pasichnyy, N. A. Shiganov, Yu. I. Korunov, I. Ye. Kasich-Pilipenko STUDY OF THE POSSIBILITY OF USING SOLAR RADIANT ENERGY FOR WELDING AND BRAZING METALS	9 ✓
B. I. Verkin, I. M. Lyubarskiy, N. M. Grinberg, L. F. Yakovenko SERVICE LIFE OF METALS AT LOW TEMPERATURES	19 ✓
V. P. Latenko, T. V. Sil'chenko, V. A. Tikhonov, V. P. Mal'tsv, V. P. Korablin MAGNESIUM-LITHIUM CASTING ALLOYS	35 ✓
B. I. Verkin, I. M. Lyubarskiy, V. M. Boychuk, N. M. Grinberg, A. I. Alekseyev FATIGUE LIFE OF METALS UNDER CYCLIC LOADING IN VACUUM	45 ✓
V. F. Udovenko, G. N. Presnyakova INFLUENCE OF LOW TEMPERATURES ON FRICTION AND WEAR	65 ✓
I. M. Lyubarskiy, A. A. Guslyakov, A. V. Ashukin, V. I. Kuleba INFLUENCE OF DEGREE OF AMBIENT MEDIUM RAREFACTION ON DEFORMATION OF COPPER AND ALUMINUM	76 ✓
B. I. Verkin, I. M. Lyubarskiy, V. F. Udovenko A. A. Guslyakov FRICTION AND WEAR CHARACTERISTICS OF CARBON STEELS IN VACCUM	83 ✓

N. V. Chistop'yánova, V. L. Chumakov THERMAL REGIME AND TEMPERATURE STRESSES IN BODIES DURING THERMORADIATIONAL HEATING	88 ✓
B. I. Verkin, I. M. Lyubraskiy, V. F. Udovenko, L. N. Sentyurikhina EFFECTIVENESS OF SOLID LUBRICANT COATINGS FOR FRICTION IN HARD VACUUM (10^{-9} tor)	99 ✓
V. S. Novikov, V. L. Chumakov TRANSIENT COOLING OF SOLID BODIES OF CLASSICAL FORM BY RADIATION	113 ✓
V. G. Babskiy, I. L. Sklovskaya, Yu. B. Sklovskiy THERMOCAPILLARY CONVECTION IN WEIGHTLESS CONDITIONS	121 ✓
Yu. A. Kirichenko HEAT TRANSFER WITH NUCLEATE BOILING OF LIQUIDS UNDER WEAK MASS FORCE FIELD CONDITIONS	131 ✓
V. S. Novikov, V. L. Chumakov RADIATIVE COOLING OF BODIES OF ARBITRARY SHAPE AND VARIABLE VOLUME IN VACUUM	160 ✓
V. S. Novikov, V. L. Chumakov NONLINEAR UNSTEADY CONTACT HEAT CONDUCTION OF TWO-LAYER SHELLS IN THE PRESENCE OF THERMAL RADIATION	169 ✓
I. S. Zhitomirskiy, V. I. Pestryakov CALCULATION OF THE HYDRODYNAMIC AND HEAT TRANSFER PROCESSES OCCURRING DURING FILLING, PRESSURIZING, AND EMPTYING OF CRYOGENIC VESSELS	178 ✓

STAND FOR STUDYING TECHNOLOGICAL PROCESSES
UNDER CONDITIONS SIMULATING SPACE

B. Ye. Paton, V. Ye. Paton, D. A. Dudko, V. N. Bernadskiy,
G. P. Dubenko, V. F. Lapchinskiy, V. V. Stesin,
A. A. Zagrebel'nyy, Yu. N. Lankin, Yu. A. Masalov,
O. S. Tsygankov and V. M. Boychuk

A test stand for conducting processing experiments under conditions simulating space is described. The stand was developed at the Ye. O. Paton Electric Welding Institute of the UkSSR. The most important units of the stand are discussed. Tests of the stand and research studies using the stand showed that it is a reliable and universal research facility and makes it possible to study processes such as metal melting, welding, and deposition.

The ever-expanding space study front raises as one of the 15* important problems, that of performing in space various technological operations (melting of metals, welding, vacuum deposition, casting of various detail parts, growing of monocrystals, and so on). This problem is particularly important at the present time, when programs to create permanent orbital scientific laboratories are being carried out both in the USSR and abroad.

Any scientific experiment in space, including a technological experiment, requires careful preparation on the Earth and this preparation is the more effective the more nearly we are able to simulate space conditions — weightlessness, hard vacuum, and the unique thermal regime of the object under study and the experimental installations [1]. A stand for conducting technological experiments under conditions simulating those of space was constructed for the first time at the E. O. Paton Electric Welding Institute of the Academy of Sciences of the UkSSR. In

*Numbers in the margin indicate pagination of foreign text.

designing the stand, the problem was posed of simulating the first two conditions, assuming that, if necessary, the experiment thermal regime could be established with the aid of thermal regulating devices.

The basic difficulties in developing such a stand are associated primarily with the fact that it must satisfy at a minimum the following requirements;

1. In conjunction with a flying laboratory, it must permit repeated operation under short-term weightless conditions.

2. It must simulate, for a period of one to two hours, the vacuum characteristic of the space surrounding the orbital manned spacecraft.

3. While being self-contained, it must have minimal weight and size and maximal reliability.

4. It must provide the greatest possible flexibility with a view to performing various technological experiments, particularly in regard to welding, vacuum deposition, and cutting of metals.

5. It must have equipment for reliable recording of the progress of the experiments.

6. It must provide reliable restraint of the operator relative to the stand with maximal convenience in control and observation of the experiment.

In addition, the stand must meet the requirements imposed on test equipment installed aboard flying laboratories. The solution of these problems is best examined by considering the most important individual functional units of the stand.

Reproduced from
best available copy.

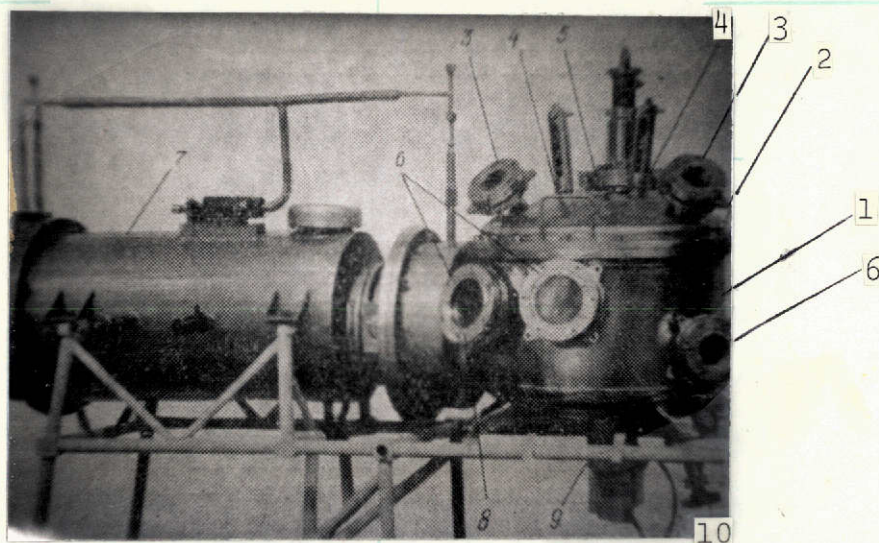


Figure 1. Working chamber with high-vacuum evacuation system.

The working chamber 1 with interchangeable technological systems is a stainless steel vacuum-tight cylindrical vessel 500 mm in diameter, capacity about 100 liters with spherical bottom and spherical hinged cover 2 (Figure 1). The chamber body is equipped with a neck 8 for connection to the high-vacuum pumping unit 7, vacuum valve 10, sealed feedthrough 9 for transmission of rotation onto the chamber, and ports 6 for observation and taking movies. The hinged chamber cover has a neck 5 with bellows compensator for installing the interchangeable technological systems, ports 3 for taking movies, and sealed feedthrough 4 for the pressure sensors.

The chamber is equipped for installation of various heat sources (electron beam, plasma, and consumable-electrode arc) of about 1 kVA power, which permit performing welding, vacuum deposition, and melting of small metal volumes. Each of these systems is miniaturized and capable of operating reliably in vacuum.

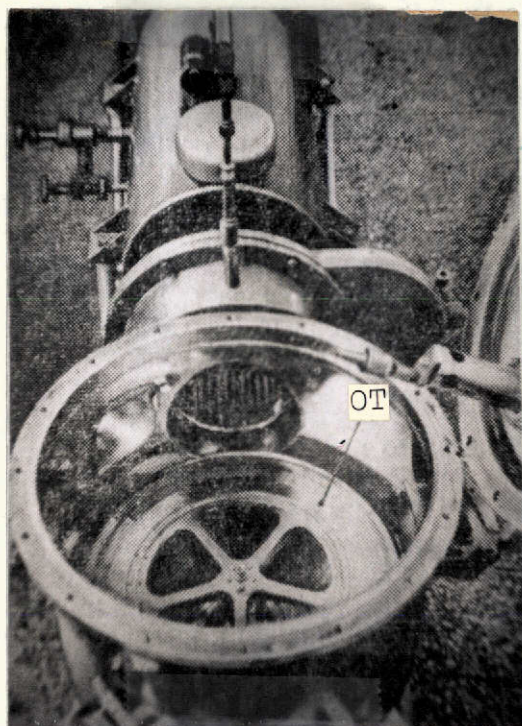


Figure 2. Working chamber with cover open.

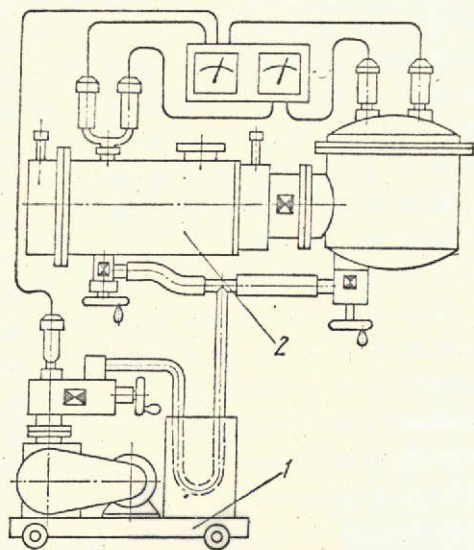


Figure 3. Schematic of test stand vacuum pumping system.

On the bottom of the chamber (Figure 2), there is located the object table, which permits the installation of either specimens to be welded or crucibles for melting metals or vacuum deposition, as desired. The table can be rotated at various speeds around the vertical axis, thereby providing displacement of the specimens being welded relative to the heat source.

The vacuum pumping system (Figure 3), consisting of the roughing pump 1 and special high-vacuum pumping unit 2, is used to create and maintain the required vacuum in the working chamber. The roughing unit consists of a VN-2 mechanical pump with 36 V motor equipped with nitrogen trap and vacuum valve. It functions only during ground preflight preparation and is fed from the airfield alternating current network.

Considerable difficulty arose in selecting the high vacuum unit. Vapor jet pumps are not suitable for operation under high load factor and weightless conditions.

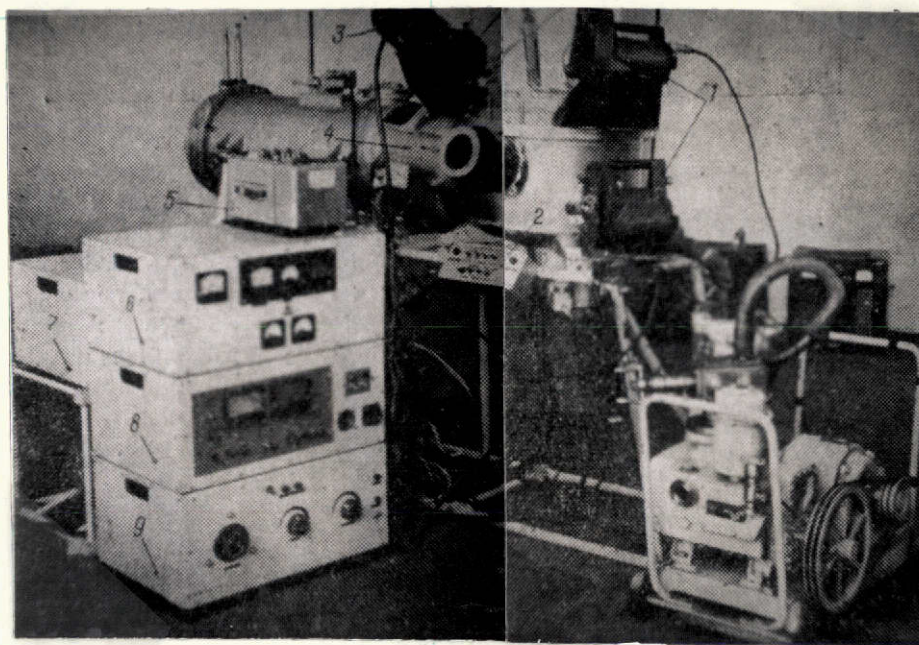


Figure 4. General view of test stand.

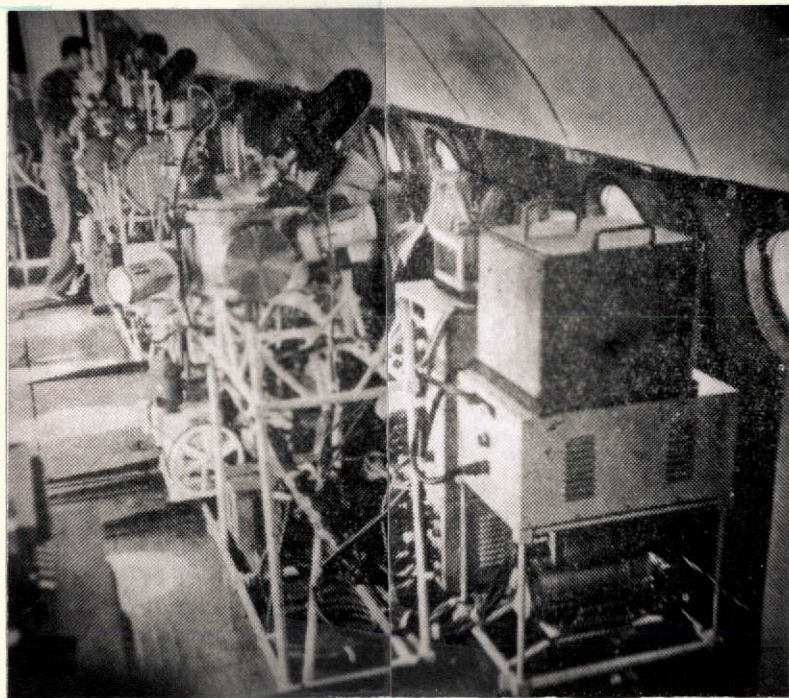
Ion sorption, molecular, and electro-discharge high-vacuum pumps cannot be used since they are heavy and bulky. Therefore, the Physico-Technical Institute of Low Temperatures (FTINT) of the AS UkSSR developed a special combined adsorption-getter high-vacuum pump for the test stand, in which activated charcoal cooled by liquid nitrogen is used to absorb argon and air, freshly deposited titanium film is used to absorb hydrogen, and a notrigen trap is used to freeze out the water vapor and carbon dioxide.

The limiting system vacuum is $(1 - 3)10^{-7}$ tor. A pressure in the range of $5 \cdot 10^{-5} - 10^{-6}$ tor is maintained in the working chamber in the course of the experiment, depending on the test conditions. This high vacuum system does not require electric power during operation, which is a considerable advantage under flying laboratory conditions.

The test stand is equipped with a *recording system* (Figure 4) to record the progress of the experiments. The experimental conditions are recorded by a K-12-21 12-channel oscillograph 5 which records the indications of the vacuum and load factor sensors and also the voltage, current, and several other process parameters. Throughout the entire experiment, movies are taken of the working zone using an AKS-2 movie camera 3 (film width 35 mm, frame frequency 24 frames per second, power from aircraft 27 V dc source). The phenomena of most interest are recorded by two SKS-1M high-speed movie cameras 1 (film width 16 mm, 300 to 78 5000 frames per second, power supplied from special source which is part of the combined test stand). A special illuminator 4 is provided for taking movies.

The possibility of space-time analysis is provided by the presence in the working zone of scale markers and time markers which are recorded synchronously on the oscillogram and movie film. The timing markers operate on two fixed frequencies — 1.2 and 10 Hz [2].

The test stand controls are mounted in several interchangeable functional blocks and on the control panel. The general control 9, instrumentation 8, and power supply 7 blocks operate continuously during all technological process testing. The control blocks 6 for each technological process are interchangeable. The system is controlled from the special panel 2. The maximal possible control automation is provided to facilitate operate functioning in flight. As a rule, the operator need only perform initial activation of the system and activation of the high-speed movie cameras to conduct the experiment, all the remaining operations are performed automatically. The operator can alter the test conditions in the course of the experiment.



Reproduced from
best available copy.

Figure 5. Arrangement of the test stand in the flying laboratory cabin.

The arrangement of the test stand in the flying laboratory cabin (Figure 5) is determined by the specific experimental conditions. The work stations of the operator and his assistant are located opposite the central illuminator of the working chamber, below which the control panel is mounted on a frame. The station is equipped with a table for writing notes, receptacle for film cassettes, leg straps and seat belt to restrain the operator's body. For convenience of reloading in flight, the SKS-1M movie cameras are located to the right of the operator and the AKS-2 movie camera and oscillograph are located to his left. The stand, as installed in the flying laboratory cabin, has dimensions of 2000 x 1450 x 1300 mm and weighs 550 kg.

The test stand made it possible to perform many important studies concerning the development of various technological processes in application to space conditions. We investigated /9 the basic relations governing welding and cutting of thin metal sheets and demonstrated the possibility, in principle, of melting small volumes of metal and vacuum deposition of metallic coatings under weightless conditions. Extensive experience in operating the stand confirmed completely the correctness of the basic engineering solutions adopted in its development. The presence of the bellows-type sealed feedthrough for installing the interchangeable technological systems makes it possible to recommend the stand for studying extremely varied technological processes. For example, with only slight structural modifications, the stand can be adapted for studying the processes of metal cutting, precision casting, and other operations in vacuum and weightlessness.

REFERENCES

1. Paton, B. Ye., and V. N. Kubasov. Avtomaticheskaya svarka, No. 5, 1970.
2. Masalov, Yu. A., Yu. N. Lankin, and D. A. Sheykovskiy. Avtomaticheskaya svarka, Vol. 3, 1968.

STUDY OF THE POSSIBILITY OF USING SOLAR RADIANT ENERGY
FOR WELDING AND BRAZING METALS

V. S. Dvernyakov, I. N. Frantsevich, V. V. Pasichnyy,
N. A. Shiganov, Yu. I. Korunov and I. Ye. Kasich-Pilipenko

An analysis is made of the solar spectrum comparison at the surface of the Earth, a facility for creating concentrated solar radiant energy flux is described, and data on its energetic capabilities are presented. The technology of solar welding by the fusion technique using the diffusion phenomenon and also joining by high-temperature brazing are examined. The use of concentrated solar radiant energy for welding and brazing metals and alloys is shown, using as examples the stainless (Cr18Ni10Ti) and titanium (OT4) alloys, and results of mechanical tests and microscopic and macroscopic studies are presented.

The use of concentrated solar energy for performing several 9 technological operations (welding, brazing, and so on) is of tremendous interest, both in the Soviet Union and abroad.

In this connection, we have studied the possibility and effectiveness of using solar radiant energy to obtain permanent bonds of various metals. The possibility of obtaining welded and brazed joints under space conditions, where favorable natural factors are present, was found to be promising.

A special solar furnace SGU-5 (Figure 1) has been designed and constructed at the Institute of Material Science Problems of the AS UkSSR in order to simulate, under terrestrial conditions, the processes of solar welding, brazing, and heat treatment, and also in order to resolve many questions which may arise under space conditions.

As is well known, more than 99% of all the energy radiated by the Sun falls in the spectral interval $\lambda = 0.1 - 4 \mu$. Solar radiation is termed shortwave in contrast with the infrared (longwave) radiation of the Earth and atmosphere. Observations show that the solar radiation reaching the surface of the Earth

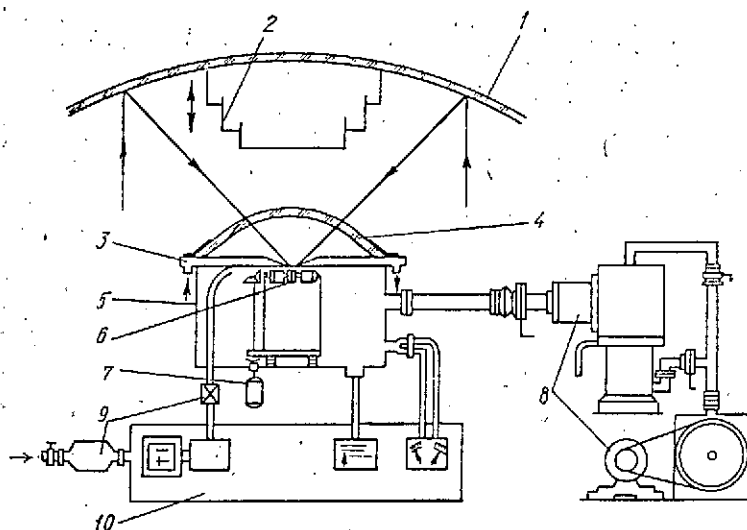


Figure 1. Schematic of SGU-5 system.

1- concentrator; 2- power regulator; 3- diaphragm; 4- quartz glass; 5- vacuum chamber; 6- specimen; 7- specimen rotation motor; 8- vacuum unit; 9- inflow system; 10- monitoring instruments.

cuts off abruptly at a wavelength of about 0.3μ , which is explained by absorption of the solar spectrum by ozone. The primary oxygen absorption bands lie in the far UV region ($\lambda = 0.13 - 0.24 \mu$).

With the Sun at the zenith, 4% of all solar radiation is UV, 46% is visible, 50% is IR; with the Sun 30° above the horizon the percentages are 3, 44, and 53%, respectively. With the Sun on the horizon, there is no UV radiation and the entire flux consists of visible (28%) and IR (72%) radiation.

The magnitude of the thermal flux density and temperature in the focal volume of the solar furnace are influenced by: a) mirror surface reflectivity (usually $R_m = 0.8$ for new mirrors and $R_m = 0.5$ for old); b) mirror optical precision h ; c) mirror angular aperture α ; d) degree of concentration C ; e) direct solar radiation intensity P_0 ; f) Sun tracking accuracy (diffuseness of the focal spot).

We used the paraboloid of a military projector unit as the /10 radiant energy concentrator in the system; the paraboloid had the following parameters:

Diameter D, m	2
Focal length f, mm	850
Aperture angle α , deg	120
Theoretical focal spot diameter d, mm	8.4
Mirror surface reflectivity, R_m	0.8
Fabrication accuracy h	4

For normal solar radiation $1 \text{ cal/cm}^2/\text{min}$, the concentrator provides about $20,000 \text{ cal/cm}^2/\text{min}$ at the focal spot with diameter 8 mm. With this radiant flux density, the blackbody temperature equivalent to the energy in the focal spot exceeds 3500° K .

The vacuum system consists of a vacuum chamber and evacuation unit. The vacuum chamber is equipped with a quartz glass cover whose external shape is the same as that of the chamber to reduce reflection losses. The chamber is mounted on the optical axis of the paraboloid in its focal plane with the aid of radial rods. The chamber contains a water-cooled interchangeable diaphragm, mechanism for holding and rotating the specimen with alignment of the edge being welded in the focal plane, and sensors for monitoring vacuum and temperature.

The interchangeable water-cooled diaphragms limit the radiant flux cross section area, passing the central portion. This reduces the overall thermal flux, narrows the zone of thermal flux distribution over the specimen, and ensures supply of the most highly concentrated radiant flux to the edges being welded.

The VA-05-4 vacuum unit consists of the VN-2 oil forevacuum pump and the N5S vapor jet pump. The unit is mounted on the projector frame and connected with the vacuum chamber by tubes, coupling, and bellows. The vacuum system provides 10^{-4} mm Hg in the welding chamber and maintains the vacuum in the 10^{-3} mm Hg range during the ten minute welding period.

The vacuum chamber can also be used for welding in a controlled atmosphere (in inert or active gases or in mixtures of inert and active gases, which are fed into the chamber under some differential pressure). In this case, the vacuum unit is disconnected and blocked off.

/11

The specimen mount provides for rotation of cylindrical specimens 50 mm in diameter and 70 mm long. The electric drive mechanism is located on the container case. The rotation rate is regulated continuously in the range from 0.2 to 1 rpm, which, for a 50 mm specimen diameter, provides movement of the edges being welded at a speed of 1.8 to 9.4 meters per hour.

The unit is equipped with instrumentation to measure solar radiation, specimen temperature, and vacuum level. It is equipped with a system for automatic Sun tracking with an accuracy of ± 10 angular minutes. The system is of the azimuth-zenith type with separate drive for rotating the reflector around the vertical and horizontal axes and consists of the following components: 1) electric power supply; 2) sensor unit; 3) electronic and electromagnetic amplifiers; 4) electric drive.

The input radiant flux power and degree of concentration were varied by special devices — interchangeable cooled diaphragms and a screening cylinder. The flux density variation range can be varied over quite wide limits depending on the

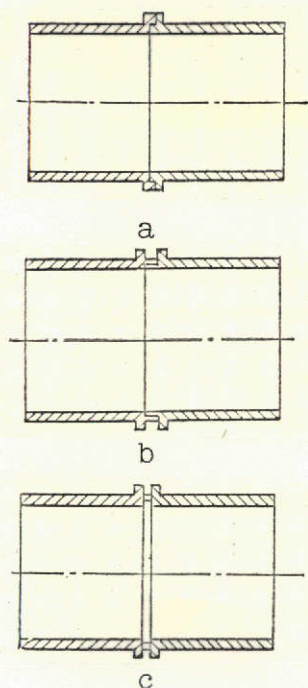


Figure 2. Preparation of specimens for pressure welding (a), flux brazing (b), and diffusion welding (c).

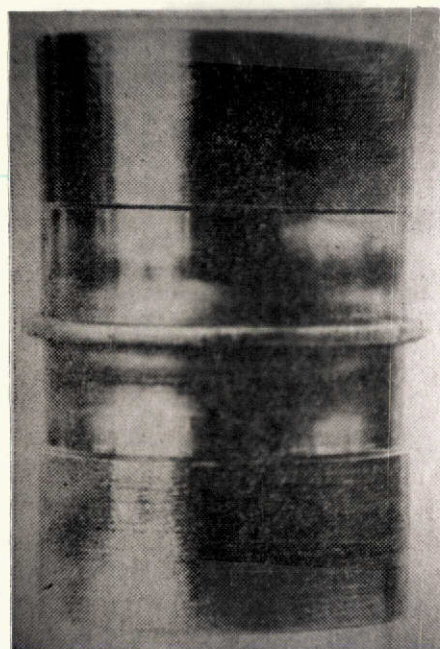


Figure 3. External view of specimen after pressure welding.

problem posed: welding, brazing, solid state diffusion welding, local heat treatment.

The radiant thermal fluxes were measured by a water-cooled calorimeter. The calorimetric measurement technique was described in detail in [1, 2]. The measurement errors obtained with a calorimeter of this type are ± 5 [2].

The thermal characteristics were obtained using air. Since the welding and brazing experiments using SGU-5 are made in a vacuum chamber with optically transparent glass which scatters part of the incoming energy, an evaluation was made of these losses. The measurements showed that the use of hemispherical pure quartz, molybdenum, and pyrex glasses 2 — 5 mm thick reduce the radiant flux by 18 — 20%.

We must remember that, during the welding process, the products of condensation deposit on the inner surface of the glass and reduce its optical properties markedly. For example, measurements showed that quartz glass absorbs up to 50% of the energy after operating for five minutes while welding 1Cr18Ni10Ti steel specimens. Upon longer operation (more than 8 — 10 min), /12 the amount of energy transmitted by the glass becomes negligible.

The welding and brazing processes were studied using 1Cr18Ni10Ti steel and OT-4 titanium alloy annular closed locked joints of universal tubular specimens 50 mm in diameter. (Figure 2). Welding was accomplished without added material along a flange of variable thickness in the overhead position. Prior to welding, the chamber was evacuated to 10^{-2} — 10^{-3} mm Hg, during welding the pressure increased somewhat. Depending on the flange thickness and nature of the material, the welding speed varied from 0.7 to 3.5 meters/hour. It was found that concentrated solar rays make it possible to melt and weld steel and titanium alloy with solar radiation $P_0 = 0.04 \text{ W/cm}^2$ and diaphragm opening diameter 12 mm, i.e., with thermal flux density about 300 /13 W/cm^2 . Under outer space conditions, i.e., in the absence of atmosphere and cloud cover, when the Sun's radiant energy intensity is more than 0.14 W/cm^2 , the 300 W/cm^2 intensity can be obtained with considerably smaller focusing mirror than under our experimental conditions. This creates a favorable basis for developing a compact system for welding and brazing under space conditions.

Visual operation of the weld metal melting process showed that the process proceeds without splashing, the weld puddle is quiet with mirror-like surface, the seam does not have the craters which are characteristic of other fusion welding techniques. The absence of craters and excess metal at the point where welding terminates makes it possible to close circular

Reproduced from
best available copy.

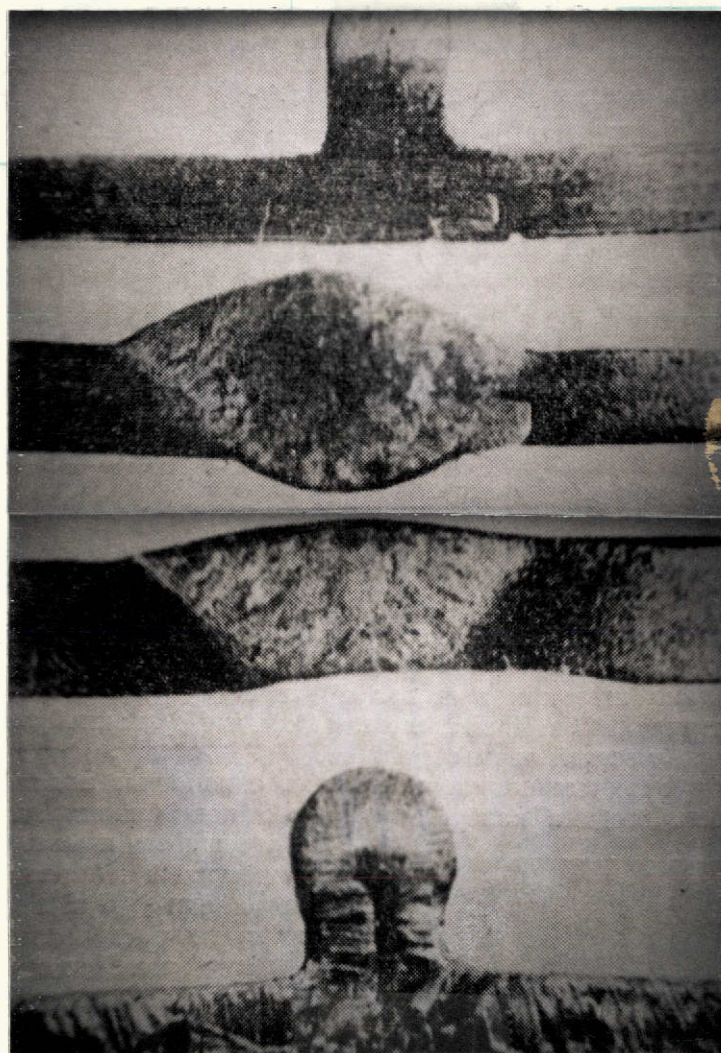


Figure 4. Macrostructure of 1Cr18Ni10Ti alloy welded joints (flange 2 mm, radiation 0.065 W/cm^2 , $v_w = 1.6 \text{ m/hour}$ (a); flange 2 mm, radiation 0.085 W/cm^2 , $v_w = 0.9 \text{ m/hour}$ (b); without flange, radiation 0.08 W/cm^2 , $v_w = 0.9 \text{ m/hour}$ (c); and OT-4 alloy (flange 3 mm, radiation 0.07 W/cm^2 , $v_w = 1.6 \text{ m/hour}$ (d).

seams without using any special techniques for regulating the input thermal power.

The outer surface of steel and titanium alloy welded joints is smooth if specimen movement is uniform (Figure 3). Although the welding was done in the overhead suspended position, this did not influence the weld seam formation quality. Figure 4 showed macrostructures of 1Cr18Ni10Ti and OT-4 alloy welded joints with total flange thickness 2 mm and the structure of a butt-welded 1Cr18Ni10Ti alloy joint without flange (thickness 2.5 mm).

Pneumatic and hydraulic tests and also metallographic studies and x-raying showed that the seam metal is dense without any internal defects. In regard to strength and structure of the seam and the heat-affected zone, the 1Cr18Ni10Ti alloy welded joints made by solar welding are similar to the joints made by argon-arc welding. However, the width of the heat-affected zones of the solar welded joints is considerably greater in comparison with the joints made by argon-arc and electron-beam welding (Figure 5).

The strength of the Cr18Ni10Ti alloy welded joints is 50 kgf/mm^2 , i.e., 90% of the parent metal strength.

The OT-4 alloy welded seam has a structure of equi-axed $\alpha + \beta$ solid solution crystals. The microhardness of the welded joint, measured across the entire plane of the section, is practically the same (230 — 265 H_u). The strength of the OT-4 alloy welded joints is 73 kgf/cm^2 , which is 90% of the parent metal strength.

One technique for joining metals in space which can be performed by solar heating is diffusion welding. Diffusion welding was carried out on OT-4 alloy specimens with low solar radiation, equal to 0.03 W/cm^2 , at which the thermal flux density on the specimen was only 200 W/cm^2 . The pressure on the surfaces being welded was 0.4 kgf/cm^2 .

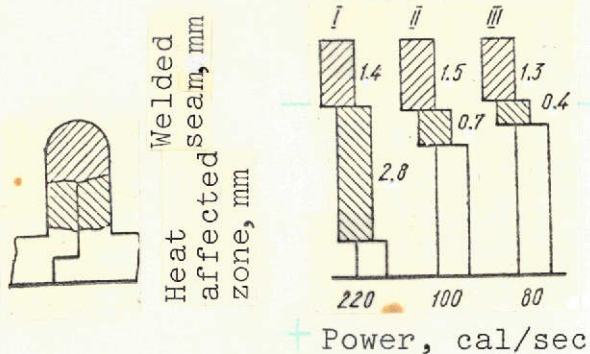


Figure 5. Width of heat-affected zone of 1Cr18Ni10Ti alloy welded joints for different welding techniques.

I- concentrated solar energy;
II- argon arc welding; III- electron beam welding.

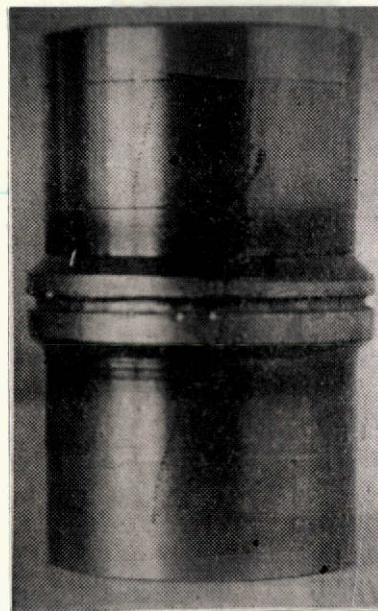


Figure 6. External view of brazed Cr18Ni10Ti alloy joint (PsrMNTs-38 brazing solder, radiation 0.03 W/cm^2).

The results of the weld joint property and microstructure study indicate the theoretical possibility of obtaining high quality bonds by solid state welding.

High temperature brazing was performed on the Cr18Ni10Ti alloy using the PsrMNTs-38 brazing solder by a defocused beam with direct solar radiation 0.03 W/cm^2 . The velocity of the edges being welded was 1.6 meters/hour. Prior to brazing, the edges of the joint were coated with a $(6 - 8)\mu$ thick galvanonickel layer. The brazing solder was placed in the joint between the flanges. Termination of the brazing process was determined visually on the basis of melting of the brazing solder (Figure 6). Study of the seam structure and mechanical properties showed that the brazed joint quality is equivalent to that of joints made using the brazing techniques customary at the present time in industry (furnace brazing, gas torch brazing, and so on).

Studies on use of concentrated solar energy as a heating source for welding and brazing indicate that the use of these methods is promising under both terrestrial and, particularly, space conditions.

REFERENCES

1. Dvernyakov, V. S., and V. V. Pasichnyy. DAN UkSSR, Vol. 6, 1966.
2. Pasichnyy, V. V., and V. S. Dvernyakov. In the book: Samoletostroyeniye i tekhnika vozdushnogo flota (Airplane Construction and Airline Engineering). Kharkov State University Press, Kharkov, Vol. 10, 1967.

SERVICE LIFE OF METALS AT LOW TEMPERATURES

B. I. Verkin, I. M. Lyubarskiy, N. M. Grinberg,
and L. F. Yakovenko

Current concepts of the nature of fatigue failure at low temperatures are presented on the basis of experimental results of various investigators. We examine the fundamental approach to the technique for studying low-temperature fatigue and confirm the necessity for using the same medium at different fatigue test temperatures and also the necessity for taking into account the magnitude of the plastic deformation amplitude. Experimental data of the authors from study of the influence of low temperatures (down to liquid nitrogen temperatures) on the fatigue life of copper and armco-iron in dry air over a wide range of deformations are presented. These results are compared with microscopic and electron microscopic pictures of the surface of the deformed specimens.

Exploration of outer space raises the problem of providing /14 for reliability and long operating life of mechanisms and devices subjected to long term variable loads under these conditions. An essential part of this problem is fatigue failure of metals under low temperature conditions. In this regard, investigators are faced with two types of problems which are intimately related with one another: first, selection of materials which ensure the required operating life under the given conditions and creating methods for evaluating their efficiency; and second, study of the general governing laws and mechanisms of the fatigue process at low temperatures.

To date, most of the studies of fatigue failure at low temperatures contain data of a handbook nature on the temperature dependence of the fatigue limit or restricted fatigue limit for liquid nitrogen, hydrogen, and helium temperatures. These studies have been conducted on a series of constructional and austenitic steels [1, 2], aluminum [1, 3], magnesium [1, 3], and titanium [4, 5, 6] alloys, and also on some pure metals Cu, Ag, Au, Mg, Zn, Fe and others [7]. The result of the studies is the conclusion that, for most of the metals and alloys, the resistance to

fatigue fracture increases with reduction of the temperature to 4.2° K, while Fe and Zn are exceptions to this rule, since they fail in a brittle fashion at 4.2° K [7].

Usually the fatigue life increase at low temperatures is associated with increase of the static strength under these conditions [1 — 7]. However, there is not a unique relation between the fatigue limit increase and the ultimate strength increase [7]. For example, for Cu, Ag, Au, and Cd, the ratio of these characteristics has a maximal value in the temperature region 100° K. This indicates that the damage accumulation process under cyclic deformation is determined by different factors than under static loading, /15

Consequently, when studying the reasons for the endurance increase in the case of fatigue fracture, it is necessary to determine the characteristics and mechanism of the processes which take place during cyclic loading. In addition, increase of the static characteristics does not always take place with reduction of the temperature. In recent years, it has been found that the static characteristics of certain metals are independent of temperature at temperatures of 78 — 1.3° K. We even observe reduction of the yield point of polycrystals or the critical shear stress of monocrystals with reduction of the temperature. This phenomenon has been found in metals with different lattice type: Cu [8], Pb [9], W [10], Nb [11] and others. In this connection, we note that most of the fatigue fracture studies at low temperatures, including those cited above, have a significant procedural drawback. As a rule, the low temperature experiments have been conducted by immersing the specimens in a cooling fluid (nitrogen, hydrogen, helium). When comparing such results with the data obtained at room temperature in air, no account is taken of the different influence on the metal of each of these media. The cooling liquids insulate the specimen from

atmospheric oxygen similar to a vacuum. Therefore, increase of the fatigue life in liquid nitrogen in comparison with the fatigue life under atmospheric conditions may take place because of two factors: temperature reduction and less influence of the medium.

This fact was first noted by Holt and Backofen [12], who conducted experiments in liquid nitrogen and helium and attempted to separate the effects of ambient medium and temperature influence on fatigue life of Cu and Cu-8% Al alloy. In accounting for the influence of the medium, they utilized the idea prevalent in the literature that the reduction of the oxygen partial pressure is associated only with slowing of the crack growth rate and has no influence on structure formation. At the same time, the fatigue life increase from temperature reduction was associated with substructure change — reduced formation of dislocation loops and grain subboundaries. They showed that the fatigue life of Cu and Cu-8% Al increases by 1.6 and 4 times, respectively, while with reduction of chemisorption, the life increases by 15 times.

Although the idea of separating the temperature and environment effects is correct, Holt and Backofen used inadequately justified assumptions. Recent studies [13, 14] have shown that the vacuum influence leads, in turn, to change of the substructure: the fatigue life increase is accompanied by change of the nature of the plastic deformation distribution. The coarse localized slip bands characteristic for deformation under atmospheric conditions are replaced upon pressure reduction by fine, densely distributed slip bands. Moreover, it has been found [15] that the influence of vacuum on Cu fatigue life is more significant in the initial stages of the fatigue process than in the crack propagation period.

Thus, when conducting experiments under different temperature conditions and in different media, it is impossible to evaluate uniquely the action of one of these factors. In order to obtain reliable data on the temperature influence, comparative tests must be conducted in an identical controllable medium. Such media may be dry air (at not too low temperatures) or vacuum. In order to evaluate the influence of low temperatures, we must consider the very complex influence of vacuum on fatigue life and the plastic deformation accumulation process [13 — 15]. In such experiments, cooling of the specimens must be accomplished by heat removal into a vessel filled with a cryogenic liquid. This low temperature test technique is also of interest because of the fact that it permits better simulation of the actual conditions to which the actual components and parts of machines are exposed. The facilities for studying low temperature fatigue constructed at FTINT AS UkSSR [16 — 18] are based on this principle. They make it possible to study the characteristics of metals under cyclic bending, torsion, and tension-compression at room and low temperatures and in vacuum down to 10^{-9} mm Hg. /16

In the torsion and tension-compression setups, cooling is accomplished to liquid nitrogen temperature, while in the bending setup, cooling is provided to approximately liquid hydrogen temperature. To accomplish this, a flexible cooling line connected with vessels which are filled with the cryogenic liquid is attached to the inactive portion of the specimen. The condition of maintaining the same medium at different test temperatures has been satisfied in the design of several other Soviet testing machines [19, 20].

In order to study the processes taking place during low temperature fatigue, it is necessary to resolve procedurally still another important problem which is not usually given adequate attention. This problem is associated with the fact that,

upon temperature reduction, for the same total deformation magnitude, the plastic component fraction decreases because of elastic deformation fraction increase. Therefore, we must bear in mind that comparison of data obtained at different temperatures must be made with account for the magnitude of the plastic deformation per cycle. Otherwise, changes of the fatigue life, structure, dislocation structure, and other factors can always take place because of the different plastic deformation amplitude. For example, in the study by Hull [25], experiments at temperatures from room to liquid helium were conducted under different stresses and the plastic deformation magnitude was not known. This makes it difficult to interpret the reasons for the phenomenon discovered by Hull — change slip band appearance with reduction of the temperature.

Laird and Krause [22], studying the temperature dependence of the fatigue life of copper and copper-aluminum alloy in vacuum, came to the conclusion that low temperature increases the fatigue life of these metals by factors of five and eight, respectively. They associate this fatigue life increase at low temperatures with slip homogenization. However, the magnitude of the plastic deformation is not known in this case. The slip homogenization may also be associated with the lower magnitude of the plastic deformation [14] and with the effect of vacuum [13].

In connection with what we have been saying, the experimental setups intended for low temperature fatigue study must of necessity be equipped with a device which permits measurement of the magnitude of the plastic deformation amplitude in each experiment. This condition was satisfied in the design of the setup for studying low temperature fatigue during cyclic bending [16]. This setup permits measurement of the total and plastic deformation magnitude at the test temperatures.

Measurement of the total deformation reduces to determining its dependence on the magnitude of the eccentric radius (i.e., on the magnitude of the deflection). The plastic deformation amplitude is determined from the width of the hysteresis loop plotted in the coordinates: load magnitude versus deformation magnitude. The magnitude of the total deformation corresponds to the maximal value of the loading. The magnitude of the plastic deformation is measured upon removal of the loading. The importance of measuring the magnitude of the plastic deformation becomes obvious when studying the reasons for polycrystalline copper and iron fatigue life increase.

The fatigue tests in symmetric bending were performed on flat specimens of cantilever type with equal resistance upon cooling to liquid nitrogen temperature and at room temperature. In this case, the temperature at the active part of the copper specimen was approximately 113° K and that of the iron specimen was 140 — 170° K. The specimens were tested after vacuum annealing and electropolishing.

The dependence of copper fatigue life on total deformation amplitude for temperatures of 293 and 113° K (Figure 1a) is the same at room and low temperatures: each curve has two segments characterized by different slope to the abscissa axis. It is well known [21] that change of the fatigue curve slope under ordinary conditions is associated with the difference in the fatigue fracture mechanism in the high amplitude H and low amplitude F regions. It appears that both of these fracture mechanisms also take place at low temperatures. /17

We see from the data obtained that the fatigue life of copper increases by nearly a factor of two with temperature reduction in the deformation range tested. This may be a

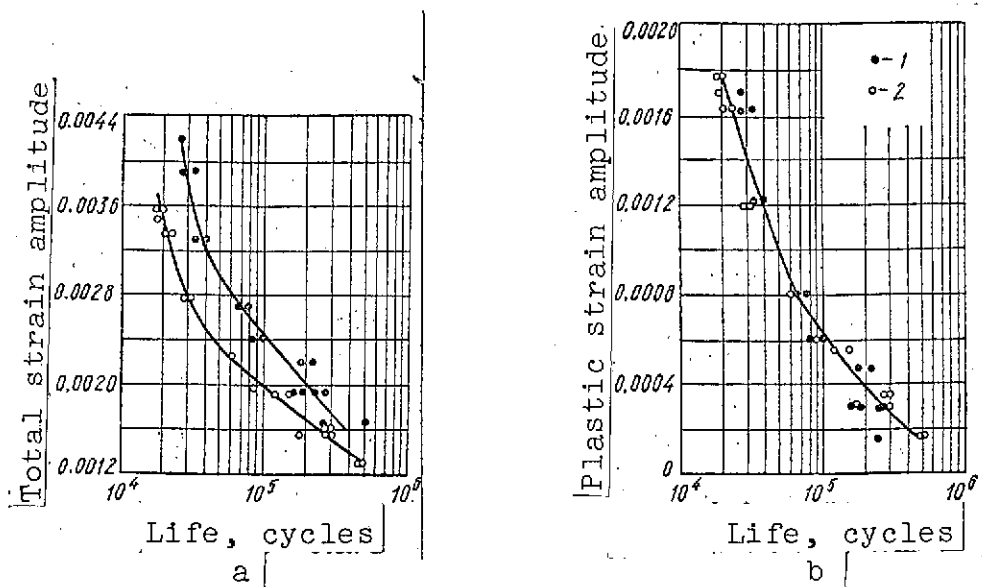


Figure 1. Dependence of copper fatigue life on magnitude of total (a) and plastic (b) deformation amplitude.

1- temperature 113° K; 2- temperature 293° K.

consequence of factors such as change of the magnitude of the plastic deformation, the resistance to which increases with temperature reduction, and change of the nature of the plastic deformation, which shows up in the formation of a different substructure.

We see from Figure 1b that for the same plastic deformation, the fatigue life of copper is the same at different temperatures.

Microscopic studies showed some peculiarities of the substructure in the low temperature deformation case. In the high amplitude region, the copper specimen surface is covered by slip bands which are not detected after light polishing and subsequent etching. It appears that the absence of stable slip bands in the high amplitude region is characteristic of low temperature fatigue fracture just as for fracture at room temperature. However, the nature of the cracks detected on the surface at low and room temperatures is somewhat different: at room

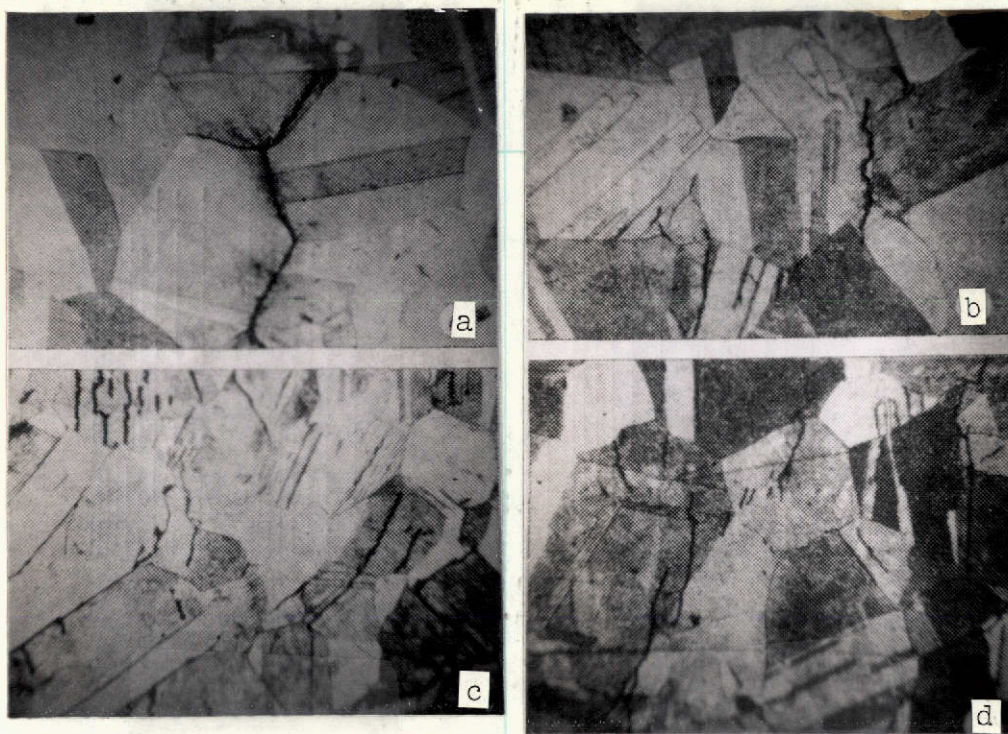


Figure 2. Cracks in cyclically deformed copper in the high amplitude region for 293° K (a), 113° K (b) and in the low amplitude region for 293° K (c), 113° K (d).

temperature, we observe intergranular cracks, while at low temperatures we find many intragranular cracks (Figure 2a, b).

In the low amplitude region at deformation temperature 113° K, we observe stable slip bands whose density is the same as at room temperature, if we compare specimens at the same plastic deformation magnitude. It appears that the slip homogenization which was observed by the authors of [22] at low temperature and was ascribed to the effect of this temperature is a consequence of high vacuum rather than the temperature influence.

At low deformation amplitudes, the fatigue cracks pass through the grain along stable slip bands for both temperatures investigated (Figures 2c, d). Consequently, the plastic deformation distribution and crack nature do not change under the influence of low temperature in the low amplitude region.

Thus, the cyclic fatigue life increase of copper at 113° K in comparison with the fatigue life at 293° K for the same total deformation amplitude is due to the lower plastic deformation magnitude in each cycle in this case.

Figure 3a shows the dependence of structural iron fatigue life on total deformation amplitude at room and low temperatures. The low temperature curve is shifted in relation to the curve obtained at room temperature. However, the nature of the curve remains the same. We see from these data that, for the same total deformation amplitude, the low temperature fatigue life increases by about a factor of three to four in the high amplitude region and by a factor of four to six in the low amplitude region. The fatigue limit also has a high value at the low temperature.

The dependence of the fatigue life of iron on plastic deformation amplitude, plotted using a calibration curve (Figure 3b), indicates that the relative positioning of the curves changes significantly in the case when the argument is the plastic deformation magnitude. For low plastic deformation amplitudes (less than 0.0003), the fatigue life of specimens tested at room and low temperatures is practically the same. For plastic deformation amplitudes above 0.0003, the fatigue life of the specimens tested at low temperature is lower than for those tested at room temperature.

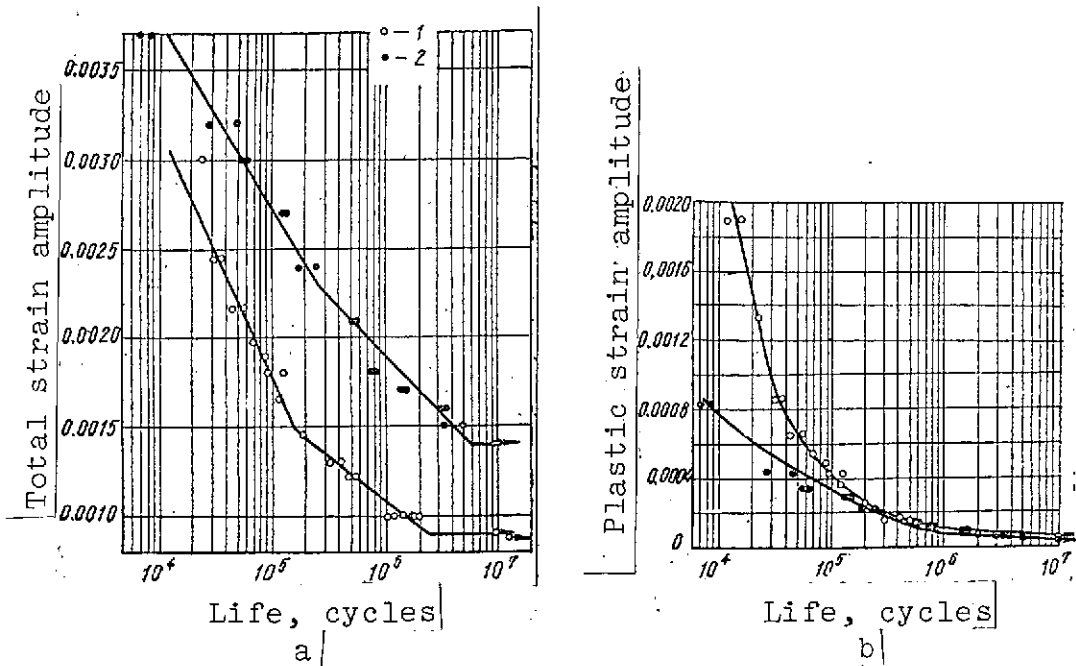


Figure 3. Dependence of fatigue life of iron on magnitude of total (a) and plastic (b) deformation amplitude.

1- temperature 293° K; 2- temperature 143° K.

Consequently, for low plastic deformation amplitudes, the fatigue life value for the same total deformation is determined only by the magnitude of the plastic deformation. For higher plastic deformation amplitudes, there are still other factors which shift the low temperature curve in the direction of lower fatigue life values. Electron microscopic study of the surface slip showed that, in the low amplitude region for equal plastic deformation amplitude and different test temperature, the slip lines are similar in magnitude and nature. In this case, the fracture is intragranular at both temperatures studied. /19

In the high amplitude region, the slip bands cover the surface of the grains more densely at room temperature than at low temperature. We also note that fracture in the low temperature case differs in nature from fracture at room temperature — in the former case, the fracture is intergranular, in the latter case it is mixed.

Comparison of the deformation and fracture characteristics of iron with the magnitude of the fatigue life leads to the conclusion that, for low deformation amplitudes, when fatigue life is determined only by the magnitude of the plastic deformation, the nature of the fracture is independent of temperature. In the high amplitude region, transition to intergranular fracture corresponds to lower values of the fatigue life at low temperatures. This fatigue life reduction at low temperatures may be associated with several factors. First, intergranular fracture may facilitate transition to the stage of rapid brittle crack propagation. Second, it is possible that, at high amplitudes, where fracture has features similar to static fracture, the stresses at the tip of the propagating crack play a significant role. At low temperature, the elastic deformation component has considerably larger magnitude than at room temperature, which may lead to greater stress concentration and acceleration of crack advancement. This may lead to the development of local brittle fracture at the crack tip regardless of its nature (intragranular or intergranular). This hypothesis is in good agreement with the known tendency of iron to brittle fracture.

We see from the data presented that, in many low temperature fatigue cases, the magnitude of the plastic deformation determines the fatigue life value. Moreover, these data indicate the necessity for studying still another aspect of this problem /20 — transition from fatigue fracture to brittle fracture.

As is well known, the metal fatigue fracture process can be divided into hardening, crack initiation, and crack propagation stages. Each of these stages is characterized by its own governing laws. Hardening and crack initiation are determined by development of the plastic deformation process, deformation magnitude, deformation distribution, formation mode, and other

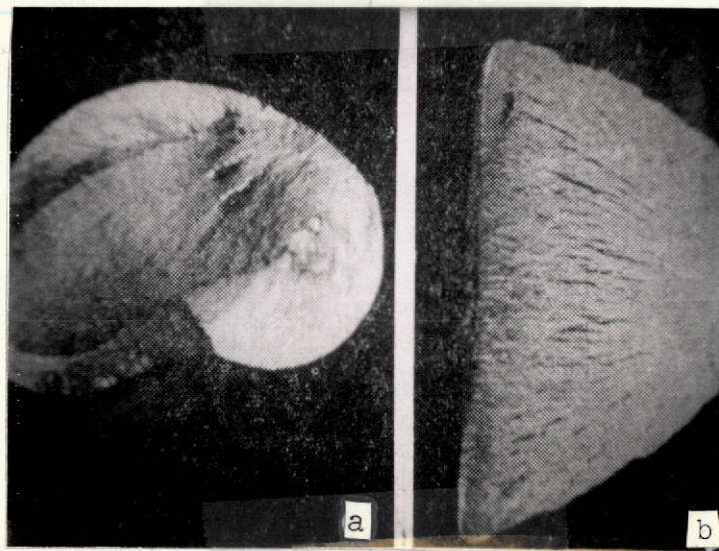


Figure 4. Appearance of titanium alloy specimen fractures at 293° K (a) and at 133° K (b).

characteristics. The crack propagation stage is the beginning of the fracture process, which is determined by other parameters.

If transition from fatigue fracture to brittle fracture takes place at low temperatures, the crack propagation stage may shorten significantly and this may lead to decrease of the fatigue life. It is probable that this was the situation in the low temperature iron fatigue case described above. Increase of the brittle fracture fraction in the crack propagation stage was observed in studying fatigue fractures of the VT-22 two-phase titanium alloy during cyclic torsion in the temperature range from -140 to +150° C [23]. Each fracture has three clearly discernible zones corresponding to the crack propagation stages (Figure 4). The initial zone (Figure 5a) has the form of an oval below the surface, located in the plane of action of the maximal normal stresses. Fracture in this zone takes place by cleavage along slip planes which have first been weakened by plastic deformation. This failure nature is typical for fatigue.

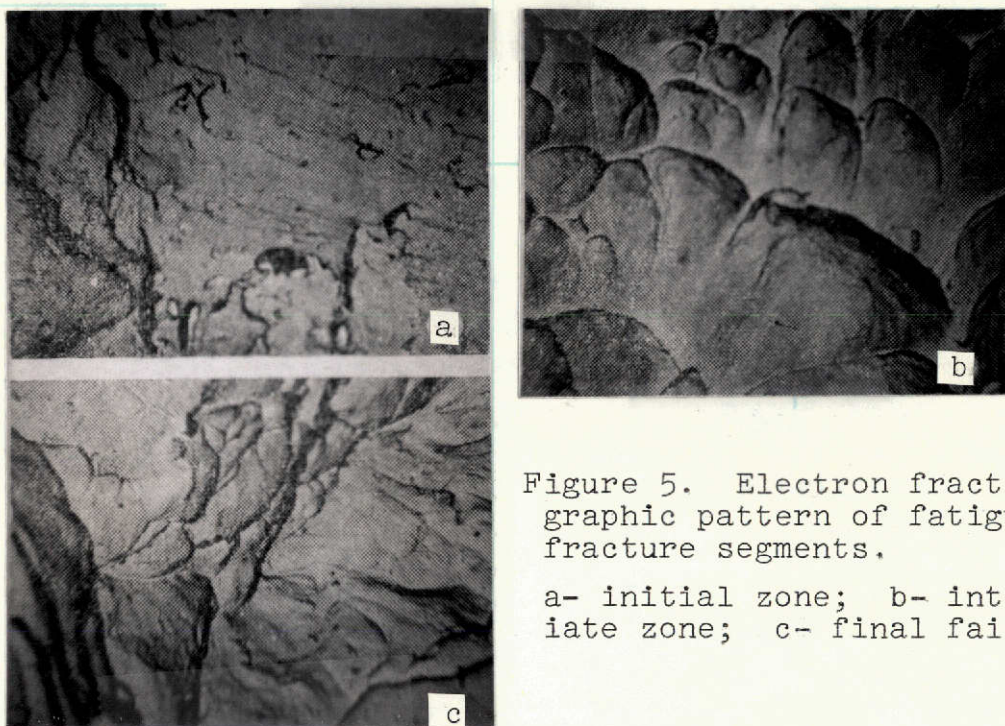


Figure 5. Electron fractographic pattern of fatigue fracture segments.

a- initial zone; b- intermediate zone; c- final failure.

The zone corresponding to the intermediate macrocrack propagation stage is located in the maximal tangential stress planes (Figure 5b). It also consists of plane cleavage segments, however in contrast with the initial stage here, the cleavage is accompanied by considerable plastic deformation. Sometimes cleavages take place along nearby planes and the splitting of each of these planes also culminates in plastic deformation.

The final failure zone, located in the plane of the normal stresses, has a mixed fracture microstructure (Figure 5c), consisting of steps, "riverine patterns," and segments whose structure is nearly "cup-like."

Thus, the fracture microstructure discloses features similar /21 in the first and second stages to ductile fracture and similar in the final stage to quasibrittle fracture.

The three zones described are observed at all temperatures from -140 to $+150^{\circ}$ C and their microstructure is independent of temperature. However, the ratio of the areas of these zones changes markedly (see Figure 4): upon temperature reduction, the area of the intermediate zone decreases at the expense of the final fracture zone. At temperatures below -50° C, the second zone becomes very small, i.e., the brittle fracture zone occupies most of the area. On this basis, we can assume that the crack propagation process accelerates with temperature reduction. This statement requires careful experimental verification under the condition of the same plastic deformation for cases of different crystal lattice type, structure, stress concentration, and so on.

In examining the fatigue characteristics at low temperatures, we should note certain peculiarities of plastic deformation under these conditions.

Thus, Hempel [24] discovered, on armco iron segments which had been subjected to cyclic deformation, the presence of twinning at liquid hydrogen temperature, while only slip occurs at room temperature.

Hull [25] showed that, upon temperature reduction the slip bands in copper become finer, are located closer together, and their number increases. At the same time, the extrusions and intrusions which form at low temperatures are similar to those which arise as a result of tests under room temperature conditions.

According to the data of Pratt [26], the dislocation formations in copper at temperatures of 78 and 295° K are similar, however, at 78° K, the dislocation wall thickness and tangling and the cell segment irregularity are greater.

Thus, comparatively extensive data which can be used to explain the mechanism of fatigue crack initiation and propagation have been accumulated. The usual cyclic deformation conditions and certain characteristics of plastic deformation behavior and substructure formation have been studied. This information is quite limited for low temperature fatigue. Clarification of the influence of low temperatures on such fatigue failure characteristics as fatigue life and fatigue limit requires further study of the laws governing the process of plastic deformation and failure under these conditions. /22

REFERENCES

1. Zambrow, J. L. and M. G. Fontana. Trans. ASM, Vol. 41, 1949, pp. 480-518.
2. Kenneford, A. S., and R. W. Nichols. J. Iron and Steel Institute, Vol. 194, 1960, pp. 1, 13-18.
3. Spretnak, J. W., M. G. Fontana, and H. E. Brooks. Trans. ASM, Vol. 43, 1951, p. 547.
4. Bishop, S. M., J. W. Spretnak, and M. G. Fontana. Trans. ASM, Vol. 45, 1953, p. 993.
5. Hempel, M. Draht, Vol. 16, No. 4, 1965, pp. 209-218.
6. Grinberg, N. M., et al. Problemy prochnosti, Vol. 4, 1971.
7. McCammon, R. D., and H. M. Rosenberg. Proc. of Royal Society, 1957, 242, 1229, pp. 203-211.
8. Pustovalov, V. V., V. I. Dotsenko, and V. F. Statinova. Problemy prochnosti, Vol. 4, 1971.
9. Pustovalov, V. V., et al. FMM, Vol. 23, No. 2, 1967.
10. Oku, T., and J. M. Galligan. Phys. Res. Lett., Vol. 22, 1969, p. 12.
11. Gindin, I. A., and Ya. D. Starodubov. FMM, Vol. 15, No. 5, 1963, p. 736.

12. Holt, D. L., and W. A. Backofen. Trans. Met. Soc., AIME, Vol. 2, 1967, pp. 264-269.
13. Grinberg, N. M., et al. FKhMM, Vol. 3, 1972.
14. Grinberg, N. M., et al. Izv. AN SSSR, Metally, Vol. 3, 1971.
15. Grinberg, N. M., A. I. Alekseyev, and I. M. Lyubarskiy, FMM, Vol. 34, No. 6, 1973.
16. Yakovenko, L. F. Zavodskaya laboratoriya, Vol. 2, 1971.
17. Boychuk, V. M., et al. Problemy prochnosti, Vol. 4, 1971.
18. Boychuk, V. M., et al. FKhMM, Vol. 4, No. 6, 1968.
19. Gindin, I. A., M. I. Starolat, and Ya. D. Starodybov. Zavodskaya laboratoriya, Vol. 6, 1970.
20. Andreyev, L. P. In the book: Termoprochnost' materialov i konstruktivnykh elementov (Thermal Resistance of Materials and Structural Elements). Naukova Dumka Press, Kiev, 1967.
21. Wood, W. A. In the book: Atomic Mechanism of Fracture. Moscow, 1963.
22. Laird, C., and A. R. Krause. Trans. Met. Soc., AIME, Vol. 242, 1968, p. 11.
23. Grinberg, N. M., I. L. Ostapenko, and I. M. Lyubarskiy. MiTOM, Vol. 8, 1972.
24. Hempel, M. In the book: Atomnyi mekhanizm pazpusheniya (Atomic Mechanism of Fracture). Moscow, 1963.
25. Hull, D. J. Inst. of Metals., Vol. 9, 1958, pp. 425-430.
26. Pratt, J. E. Acta met., Vol. 15, No. 2, 1967, pp. 319-327.

N74-28027

MAGNESIUM-LITHIUM CASTING ALLOYS

V. P. Latenko, T. V. Sil'chenko, V. A. Tikhonov,
V. P. Mal'tsev and V. P. Korablin

The strength properties of magnesium-lithium alloys at room, low, and high temperatures are investigated. It is found that the alloys may have practical application at ambient temperatures up to 100° C, that negative temperatures have a favorable influence on the alloy strength, and that cyclic temperature variations have practically no effect on the strength characteristics. The influence of chemical coatings on corrosion resistance of the MgLi alloys is examined. Several facilities based on pressure casting machines, low-pressure casting machines, and magnetodynamic pumps were designed for producing MgLi alloy castings. Results are obtained for MgLi alloys reinforced with fibers having volumetric content 15%.

With the growth of space and aircraft technology, the need /22 arises for new super strong and super light materials. Therefore, the interest in alloys of magnesium with lithium — a super light material having quite high specific strength — becomes understandable.

Judging by foreign and Soviet studies primarily the deformable alloys are used in aerospace technology. Among the magnesium-lithium alloys developed in the USA, the LA141SZ and LA141A [1] deformable alloys are most widely used. In the USSR, the IMV3 and VMD5 alloys are recommended for industrial use. These alloys have a good combination of specific strength and plasticity.

Casting class alloy compositions have been developed to a /23 far smaller degree. Several casting alloys based on the magnesium-lithium system have been developed at the IPL (Institute of Precision Casting) of the Academy of Sciences of the UkSSR (the alloy compositions were developed by A. A. Gorshkov, Corr. Mem. AS UkSSR, and P. S. Kozenko, Cand. Tech. Sci.). The basis of the MgLi casting alloys with content 15 — 16% Li is the β phase

(cubic modification of the crystal lattice). The alloying additives either enter into the solid solution, hardening it, or form independent phase components (Figure 1). At the present time, a broad range of studies of the MgLi alloys is being carried out at the Institute. The following mechanical properties have been determined: fatigue strength σ_{-1} at normal temperatures, ultimate tensile strength σ_u , relative elongation δ , Young's modulus E , thermal expansion coefficient α at temperatures -70°C , $+50^\circ \text{C}$, $+100^\circ \text{C}$, $+200^\circ \text{C}$, $+300^\circ \text{C}$, and $+400^\circ \text{C}$, and also these same characteristics and the yield strength $\sigma_{0.2}$ and fatigue strength σ_{-1} after five temperature variation cycles (-60°C and $+65^\circ \text{C}$ for two hours).

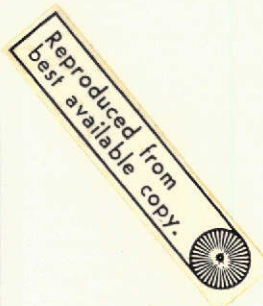
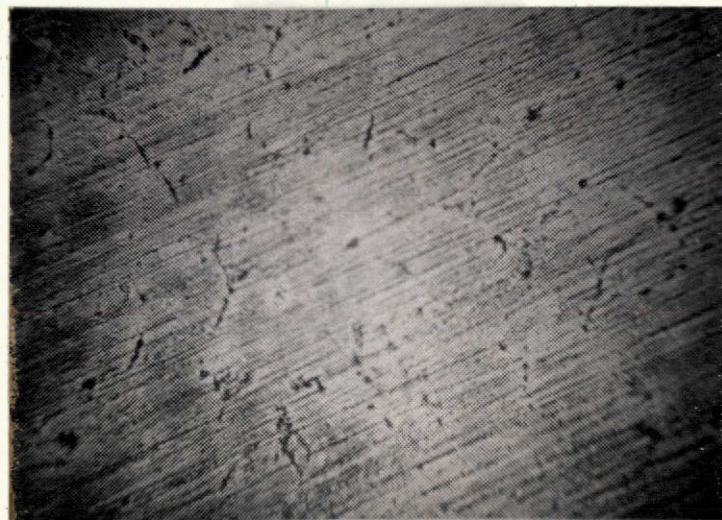


Figure 1. Microstructure of cast specimens of an alloy of the Mg — 15% Li system alloyed with aluminum, zirconium, and RZM (rare earth metals) x 300.

The test specimens were cut from blanks cast into a graphite form. Prior to introduction of the RZM, the alloy was heated to 800°C , pouring of the alloy into the form was performed at $720 - 740^\circ \text{C}$. Prior to casting, the form was preheated to $250 - 300^\circ \text{C}$. The study of the mechanical characteristics σ_u , δ , $\sigma_{0.2}$, and E was conducted together with the IPP of the AS UkSSR (see table), the study of σ_{-1} was conducted together with the IM (Institute of Metals) of the AS UkSSR.

RESULTS OF MECHANICAL TESTS OF MgLi ALLOYS

Characteristic	Units	Test Temperature, °C						
		20	50	100	150	200	-70	Cyclic (-60, +65)
σ_u	kG/mm ²	11.6	11.7	11.1	6.9	3.5	13.8	12.0
$\sigma_{0.2}$	"	9.8	10.3	10.2	6.8	3.0	11.5	10.7
δ	%	6.6	4.05	4.35	4.0	-	17.6	2.3

We can conclude from the test results that the MgLi alloys may have practical application at ambient temperatures up to 100° C; negative temperatures have a favorable influence on the strength of the alloy; cyclic temperature variations have no noticeable influence on the strength characteristics of the alloy.

/24

Young's modulus E was determined on UP-1 and UP-6 testing machines by the dynamic resonance method from the first bending and longitudinal vibration mode of a cylindrical specimen. The test results are shown in Figure 2. The influence of temperature on the thermal expansion coefficient is shown in Figure 3. We see that Young's modulus and the thermal expansion coefficient decrease monotonically with temperature increase.

The fatigue stress values for specimens which have been subjected to cycling (-60, +65° C) are 2 — 3 kG/mm² higher than for specimens under normal conditions (Figure 4).

Corrosion resistance of a material is important in evaluating its suitability. Most aerospace technology products are tested for corrosion resistance under tropical climate conditions (temperature 40° C, relative humidity 98%). The MgLi alloy specimens were tested under these same conditions. The

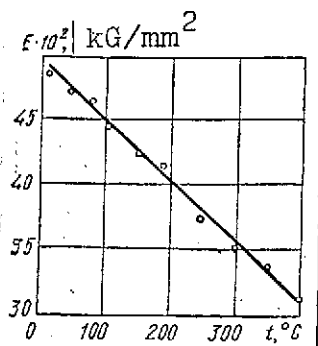


Figure 2. Young's modulus of MgLi alloy versus temperature.

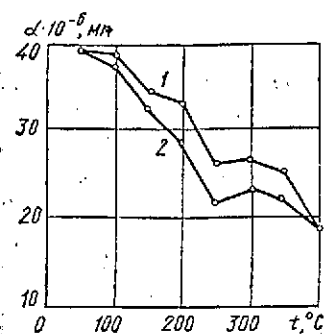


Figure 3. Temperature dependence of coefficient α of MgLi alloy.

1- conventional specimens; 2- specimens after cycling.

specimens of dimensions 30 x

15 x 3 mm were placed in a special sealed chamber where constant temperature and humidity were maintained. Specimens with and without anticorrosion coatings were placed in the chamber.

Specimens of the AL4, AL9, and ML5 alloys were used as comparison specimens. The corrosion resistance characteristics are shown in the following table.

Specimen condition	Corrosion index $n \cdot 10^{-3}, \text{mg/cm}^2/\text{day}$ (10 day ave.)
Uncoated	3.54
Coating NaF, $\text{K}_2\text{Cr}_2\text{O}_7$	3.37
Coating $\text{K}_2\text{Cr}_2\text{O}_7$, alum, acetic acid	3.45
Coating $\text{K}_2\text{Cr}_2\text{O}_7$, nitric acid NH_4Cl	3.22
Oxidation $\text{K}_2\text{Cr}_2\text{O}_7$, MgSO_4 , $(\text{NH}_4)_2\text{SO}_4$	1.20
Oxidation + primer (VL-062) + enameling (EP-755)	1.81
Oxidation + epoxy resin	2.10
Uncoated with addition of Be to alloy	3.6
Uncoated from AL4 and AL9 alloys	0

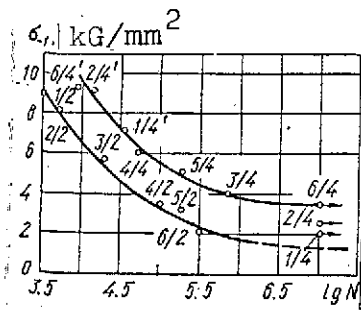


Figure 4. Fatigue curves of MgLi alloy (specimen number in numerator, test number in denominator).

- 1- conventional specimens;
- 2- specimens after cycling (-60, +65° C).

An estimate of the corrosion ^{/25} rate was made on the basis of specimen weight loss in milligrams per square centimeter on surface per day.

We see from the data presented that the chemical coatings used, except for oxidation, did not yield any marked corrosion resistance increase in a humid medium. The specimens coated with enamel and epoxy resin have better corrosion resistance than uncoated

specimens, but in the course of the tests, we observed blistering and peeling of the enamel and epoxy resin from the specimen surface. Therefore, these coatings cannot be recommended for protecting parts against corrosion during long term exposure to a humid medium.

Improvement of the corrosion resistance of the magnesium alloys is provided by alloying them with metals having high relative oxide film density. We used as the alloying element beryllium, which was introduced into the melt in the amount of 0.002 — 0.003%. Testing of the specimens showed that the corrosion resistance of the alloy is not improved with this amount of beryllium. The best results were obtained with oxidation of the specimens. According to the foreign data, oxidation of the magnesium alloys is used prior to application of paint and lacquer coatings to the part. Therefore, it is possible to continue studies to select paint and lacquer coatings which can be applied to oxidized parts.

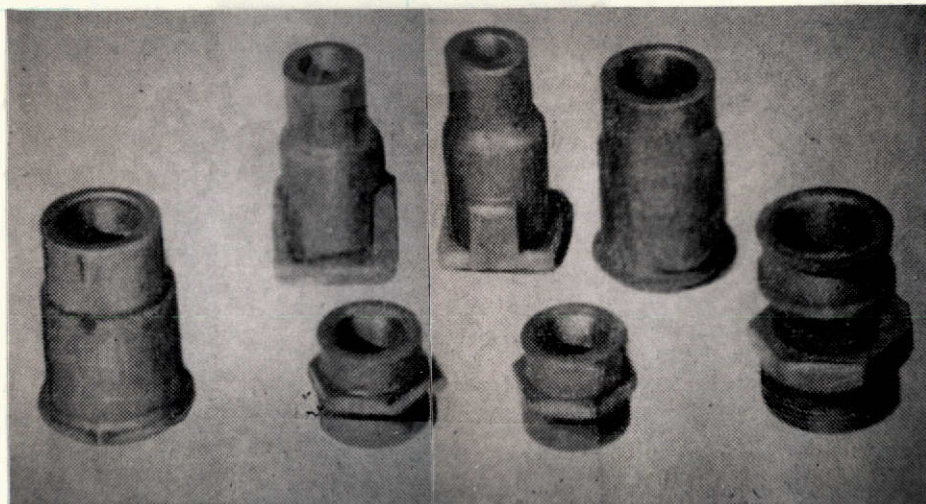


Figure 5. Cast detail parts.

One of the negative characteristics of the alloys is their higher chemical activity and predisposition to combustion upon heating and in the liquid state.

Protective fluxes perform their role in the melting process, but are completely unreliable during pouring. Moreover, during melting under flux, complete assimilation of the RZM, Si, and Mn does not take place because of the fact that these elements are easily wetted by the flux and settle to the bottom of the crucible along with the flux. Therefore, melting under flux cannot be considered acceptable in industrial use of the alloys.

Several facilities for melting and pouring MgLi alloys have been designed at the Institute of Precision Casting of the AS UkSSR: melting and pouring unit using a pressure casting machine, melting and pouring unit for low pressure casting, melting and pouring unit using a magnetodynamic pump.* Common to all the units is the fact that melting is carried out in a sealed crucible

*In the design of these pumps, we used the recommendations of G. P. Borisoa and V. P. Polishchuk, Candidates of Technical Sciences.

or chamber, which prior to connection into the system is evacuated to a residual pressure of 0.1 — 0.05 mm Hg and filled with purified argon (pressure 1.2 to 1.4 ata). In all cases, the casting forms are also evacuated and, if necessary, a protective atmosphere can be provided in the forms. The melting vessel and casting form are interconnected by a molten metal transfer line. /26

The use of differential pressure in crystallization of castings, on which the described facilities are based, is extremely important in obtaining castings from light weight alloys such as MgLi, which have very low metallostatic pressure. /27

Stainless steel and graphite are used as the form material. The most effective protective coating for the form was found to be a 0.05 — 0.1 mm thick coating of carbon black from combustion of polystyrene foam applied to the cleaned working surface of the form prior to each pouring. Castings made from the MgLi alloys are shown in Figure 5.

The strength and heat resistance of the MgLi alloys can be increased by reinforcing the castings using high strength and high modulus filaments. Some work in this direction has been carried out at the Baikov Institute of Metallurgy of the AS USSR with the deformable alloys [2]. Reinforcing was provided by continuous AT-3 alloy and 28A steel filaments by impregnation under pressure and explosive welding. The maximum strength obtained using the MgLi — AT-3 composition was 40 kg/mm^2 , the strength obtained using the MgLi-22A steel composition was 60 kg/mm^2 , the corresponding moduli of elasticity were 6600 and 7000 kg/mm^2 .



Reproduced from
best available copy.

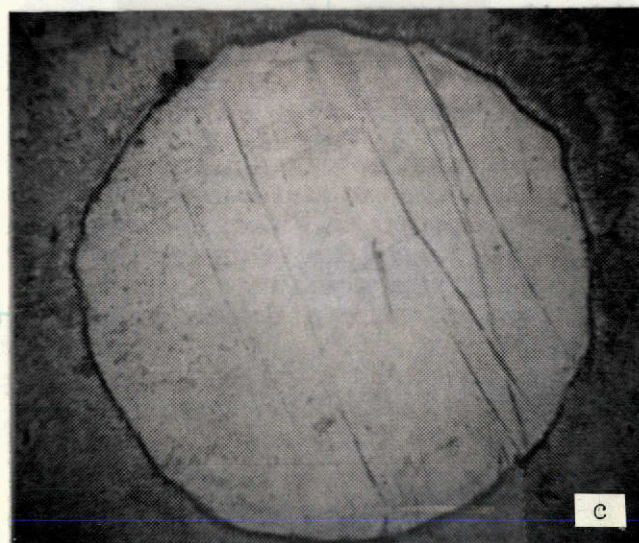


Figure 6. Microstructure of composite material specimens.

a, b- alloys reinforced with 1Cr18Ni10Ti wire, \varnothing 0.3 mm, x 300 and x 10,000, respectively; c- alloy reinforced with EP322 wire, \varnothing 0.2 mm x 300.

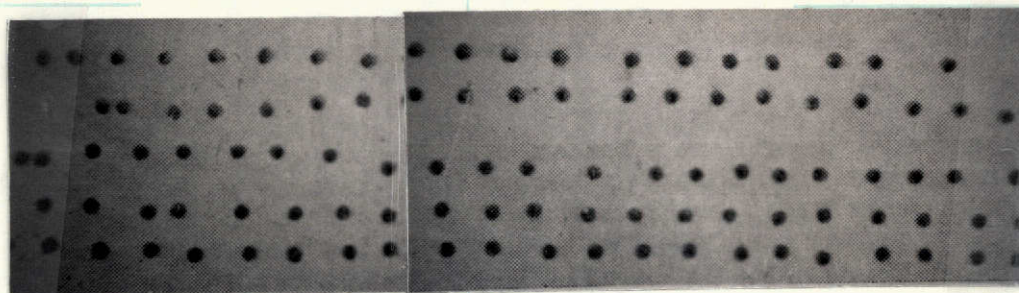


Figure 7. Macrostructure of specimen reinforced with EP322 wire \varnothing 0.2 mm x 16.

Work has been carried out at the Institute of Precision Casting of the AS UkSSR to obtain lightweight composite casting materials with MgLi alloy matrix. Individual castings using filaments of various materials were made in order to determine the interaction between the filaments and matrix. Microscopic study of sectioned specimens (Figure 6) showed that, in all cases, there is a zone of interaction of the filament material and the matrix material. The width of the interaction zone is different for the various materials, but in the worst case does not exceed 10 microns in radius. Moreover, this zone is quite stable and broadening of the zone was not observed at room temperature in the course of six months.

In order to obtain reinforced specimens, special frames were prepared on which 0.3 mm diameter EP322 steel wire was wound. The spacing between filaments was determined so that the reinforcement volumetric fraction amounted to 15% of the total volume. The frame with the wire wound on it was placed in a graphite form, which in turn was placed in the shaft of an electric furnace and heated to 450 — 500° C. Pouring of the form was carried out at this same temperature. The metal was melted under flux in an open crucible and the pouring temperature was 700 — 720° C. In the resulting specimens, all the filaments were coated with metal with any discontinuities (Figure 7).

A more advanced technology for obtaining reinforced specimens has now been developed, which provides for electric preheating of a chill mold and obtaining reinforced billets in the vacuum chamber of a low pressure casting facility.

Thus, the work which has been done has shown the possibility of obtaining cast composite materials based on the MgLi alloys. At the same time, there are definite difficulties in obtaining specific detail parts. Thus, during preheating of the form prior to pouring the reinforcing filaments, sag and tensioning of the filaments presents considerable technological difficulty. /28 Moreover, the problem of reinforcing contoured parts has not yet been resolved.

In conclusion, we can express confidence that, with resolution of the question of improving corrosion resistance and obtaining stable tensile strength characteristics, exceeding 20 kg/mm^2 , the MgLi casting alloys will find extensive application in space and aircraft technology, electronics, and other branches of engineering.

REFERENCES

1. Nazvanova, V. A., and B. I. Kogan. In the book: Redkiye elementy (Rare Elements). Moscow, 1970.
2. Kop'yev, I. M. In the book: Fizicheskiye i khimicheskiye osnovy zharoprochnosti metallicheskih materialov (Physical and Chemical Bases of High Temperature Strength of Metallic Materials). Moscow, 1971.

FATIGUE LIFE OF METALS UNDER CYCLIC LOADING IN VACUUM

B. I. Verkin, I. M. Lyubarskiy, V. M. Boychuk,
N. M. Grinberg and A. I. Alekseyev

The effect of vacuum on the cyclic strength of metals is examined. Experimental data are presented of studies by the authors to clarify the mechanism of vacuum influence on fatigue failure. The dependence of copper and armco-iron fatigue life on vacuum level is studied. It is found that the presence of saturation on the curve of fatigue life versus vacuum level is common for the materials studied. The effect of vacuum on fatigue fracture of copper is studied over a wide range of deformations. It is shown that fatigue life increase under vacuum conditions and the observed characteristics of the fatigue fracture itself in vacuum are associated with homogenization of the plastic deformation under these conditions.

During the last decade, many studies devoted to investigating /28 the process of fatigue failure under vacuum conditions have appeared. The increased interest in this problem is explained by several factors. In connection with the development of space technology, particularly with the duration of vehicle stay in space, the necessity arises for obtaining practical information on structural material characteristics under conditions simulating space. For successful resolution of the problem of selecting the material and its processing technology and predicting its capability to operate in outer space, it is necessary to study the mechanism of vacuum influence on the fatigue fracture process. Finally, the fact that study of fatigue fracture under vacuum conditions yields important information on the physical mechanism of this process is very significant. Unfortunately, the data available in the literature have not been systematized and are difficult to compare with one another. This is associated, particularly, with the fact that the studies have been made using different materials and under different conditions. Moreover, when treating the reasons for the influence of vacuum on the fatigue properties, many investigators have used previously proposed and often purely hypothetical concepts, and therefore, their ideas are, to a considerable degree, biased.

At FTINT AS UkSSR, along with study of the fatigue properties of the structural metals and alloys which are used in space technology and testing of specific vehicle components under high vacuum conditions, studies are being made to clarify the mechanism of the vacuum influence on the fatigue fracture process. Three machines have been developed for fatigue testing in high vacuum down to $5 \cdot 10^{-9}$ mm Hg using cyclic tension, torsion, and bending [1 — 4]. A distinctive feature of these machines is that each has been designed on the basis of the same standard vacuum system. The configuration of the vacuum system permits the use of various loading mechanisms for the required testing mode without any system changes. At the same time, provision is made for identical test conditions in regard to vacuum level and residual gas composition. All the machines have load excitation systems with a crank mechanism which permits testing with constant deformation amplitude.

The fatigue process development is studied by metallographic analysis using the MIM-7 electron-optical microscope, both to /29 study the slip bands on the surface of the specimen and to identify the stable slip bands and cracks (after polishing and etching).

Electron microscopic study of the surface is conducted by the method of single-stage lacquer replicas, tinted with chromium, on an UEMV-100V electron microscope with magnification 20,000.

Influence of different vacuum level on fatigue properties of metals. The study of vacuum influence on fatigue life has been made for many metals and alloys. The largest volume of data relates to aluminum [5 — 9], its alloys [10, 11], and various steels [12 — 15]. Lead [16], gold [17, 18], silver [12], molybdenum [19], indium [20], titanium alloys [21], and other metals have also been studied. The investigations show that the

fatigue life of nearly all materials increases in vacuum to a greater or lesser degree in comparison with the fatigue life in air. An exception is gold [18], whose fatigue life is independent of the vacuum. The influence of differing vacuum level on fatigue life has been studied primarily for metals with FCC lattice.

Specifically, for copper [5], the number of cycles to failure increases linearly with increase of vacuum to $2 \cdot 10^{-6}$ mm Hg (limiting value of the vacuum in the experiments). A limiting ambient pressure below which the fatigue life remained constant was obtained for the other materials studied [6 — 8]. It is of interest to clarify the influence of vacuum on the fatigue life of copper in the higher vacuum region, Figure 1a shows the results of such a study, where testing of copper specimens under sign-symmetric bending was conducted in the pressure range from atmospheric to 10^{-9} mm Hg. In contrast with the data of Wadsworth [5], the linear dependence of fatigue life on vacuum level is maintained only down to 10^{-4} mm Hg, thereafter, the $\lg N = f(\lg P)$ curve "saturates."

Similar curves were obtained for armco iron — a typical representative of the metals with BCC lattice (Figure 1b). The dependence of fatigue life on vacuum intensity for armco iron is analogous to that for copper. The trend of the curve with saturation seems valid and apparently reflects the fact that, beginning at some value of the vacuum, the material fatigue life is determined by the basic fatigue fracture mechanism. These data are also of interest in connection with the fact that cyclic strength tests under conditions simulating space can be conducted in the laboratory.

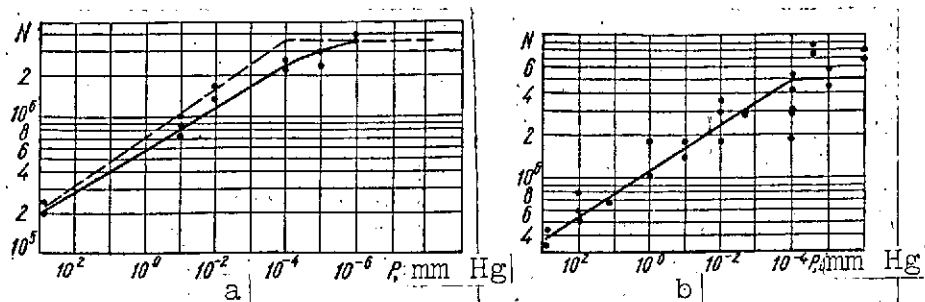
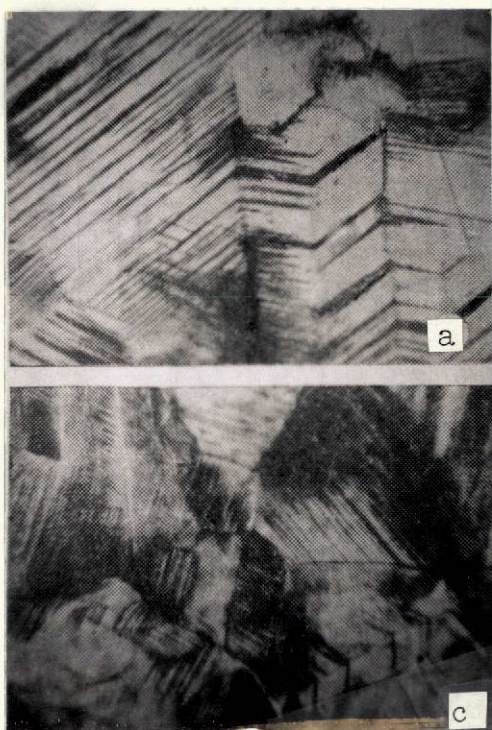


Figure 1. Dependence of fatigue life of copper (a) on oxygen pressure (solid line) and vacuum level (dashed line) and of armco iron (b) on vacuum level.

There are several viewpoints concerning the mechanism of vacuum influence on fatigue life of the metals. In [6, 8], the fatigue life increase in vacuum is explained by reduction of the wedging action of the oxide films in the crack propagation process. Martin [22] and Morecraft [14] suggested that fatigue life increase in vacuum is associated with "healing" of the freshly formed cracks during the compression cycle, while in air the adsorbed gases oppose this process. It follows from the hypotheses explaining the observed effect that, as soon as the adsorption rate becomes equal to or less than the crack propagation velocity, there should be marked fatigue life increase with subsequent saturation. However, we see from the results presented above that this abrupt fatigue life increase does not necessarily occur. /30

An entirely different approach to this problem is that of Kramer [7], who explains the fatigue life increase of aluminum in vacuum by the formation of a near-surface "debris" layer with lower dislocation density than in air. He has in mind a sub-surface layer with increased dislocation density relative to the volume of dislocations which form during deformation. According to Kramer, this situation facilitates plastic relaxation of the stresses at the crack tip under vacuum conditions and leads



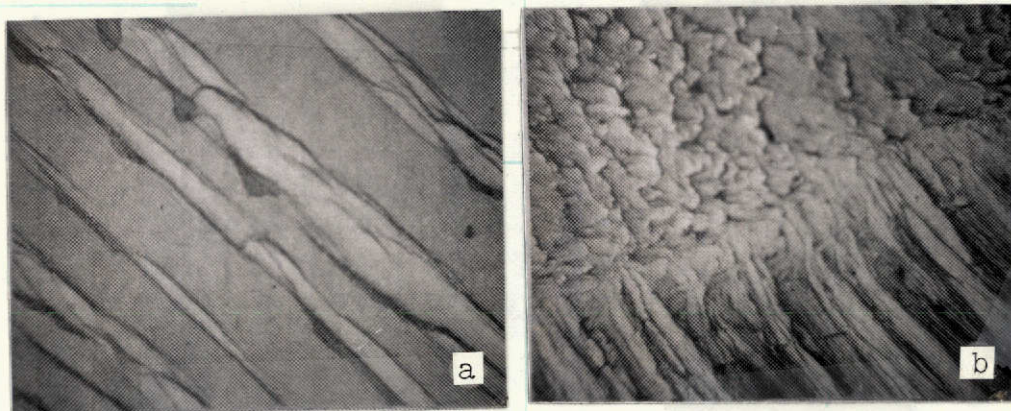
Reproduced from
best available copy.

Figure 2. Slip bands.

a, b- in air and vacuum
(respectively $N = 2.6 \cdot 10^5$
and $N = 3.2 \cdot 10^6$ cycles to
failure); c- in vacuum
($N = 2.6 \cdot 10^5$ cycles).

to slower crack propagation. In all the studies cited, plastic deformation in the early stages of the process is practically ignored. It is assumed that the entire influence of vacuum on fatigue life is associated with change of the crack propagation velocity because of oxygen adsorption at the crack tip.

Since the fatigue failure process and, specifically, the crack propagation process are associated with plastic deformation accumulation, it is of interest to clarify the nature of plastic deformation in vacuum and in air. Metallographic study of the surface of copper specimens after deformation has shown that grains with highly developed and widely spaced slip bands and also grains free of slip bands are characteristic for cyclic loading in air (Figure 2a). As the vacuum is increased to 10^{-4} mm Hg, the number of such grains decreases, grains with fine and densely spaced slip bands are observed, and the nonuniformity in



Reproduced from
best available copy.

Figure 3. Electron microscopic pictures of the surface of specimens tested in air (a) and in vacuum (b). x 20,000.

the distribution of the stable slip bands decreases. The results of studies of specimens after fracture in air and in vacuum are /31 ambiguous, since specimens are compared which have experienced different numbers of cycles and which, consequently, have different total plastic deformation. Therefore, we studied specimens after the same number of loading cycles in vacuum and in air ($2.6 \cdot 10^5$ cycles). We see from Figures 2b and c that the fact that slip is more uniform under vacuum conditions than in air was confirmed.

A more detailed picture of the slip bands and nature of their distribution was obtained by electronic microscopic study of the surface. Characteristic for specimens deformed in air (Figure 3a) are highly oriented slip lines in which extrusions and intrusions are observed. The plastic deformation is not uniform and the slip lines alternate with segments which are either free of deformation or slightly deformed by fine slip.

Characteristic for specimens deformed in air is the presence of slip bands with smaller extrusions and intrusions which completely cover the specimen region in the field of view (Figure 3b).

Thus, we see from the metallographic study data presented above that plastic deformation of copper is more uniform under vacuum conditions than in air. A consequence of the plastic deformation uniformity will be reduction of the probability of failure at a given local site. This then is apparently the reason for fatigue life increase in vacuum. We can attempt to explain the influence of vacuum on slip distribution nature using Kramer's "debris" layer idea. In the slip band formation process, when hardening has taken place in some plane, further deformation can take place in two ways: a) in neighboring slip planes, i.e., roughly speaking, at the same local site, for example, as a result of double lateral slip; b) at an arbitrary site where a new dislocation source develops.

Under vacuum conditions, where the dislocation entanglement density in the near surface layer is less than in air [27], a larger number of dislocation sources is activated and, as a result, the slip is more uniform.

The nature of fatigue life dependence on vacuum level can be explained as follows. As the pressure of the ambient medium is reduced, the rate of oxygen adsorption on the freshly formed slip steps decreases. This leads to less intense dislocation accumulation in the near surface layer, as a result of which slip becomes relatively more homogeneous and fatigue life increases.

Beginning at some pressure, the adsorption rate becomes lower than the rate of slip step appearance, as a result of which the near surface layer effectiveness and fatigue life no longer depend on the vacuum level as this level is decreased further. In this case, the fatigue life is determined by the basic crack distribution propagation mechanism. /32

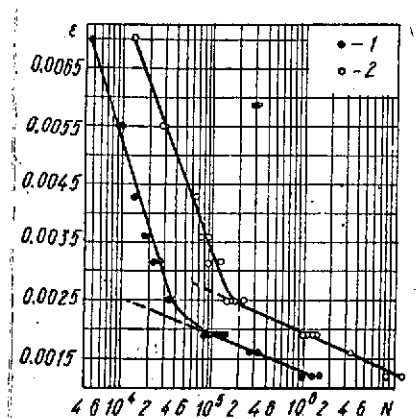


Figure 4. ϵ -N curves in vacuum (1) and in air (2).

Influence of vacuum on fatigue fracture of copper in the high and low amplitude deformation regions. As is known [23], the fatigue failure mechanism, particularly of copper, at high and low deformations is different. Characteristic for the high amplitude H region is the slow static failure mechanism, while in the low amplitude F region, failure is associated with damage and distortion accumulation in active slip planes.

In explaining the influence of vacuum on fatigue life and other fatigue failure characteristics, we did not specify for which deformation region the particular hypothesis was applicable. In this connection, it is of interest to study the influence of vacuum on fatigue life over a wide deformation range for both the F and H regions.

The results of experiments to determine fatigue life as a function of deformation magnitude in air and in vacuum are shown in the form of ϵ — N curves (Figure 4) and indicate that the fatigue life of copper increases markedly under vacuum conditions throughout the entire deformation interval studied ($\epsilon = 0.0012$ to 0.0070). A metallographic study was made of the surface of specimens which had been subjected to polishing and etching after deformation in vacuum and in air to detect the stable slip bands. Characteristic for specimens tested in air in the low amplitude deformation region are stable slip bands, whose number decreases as the deformation increases. Stable slip bands were not detected above the value $\epsilon = 0.0019$ corresponding to transition from the

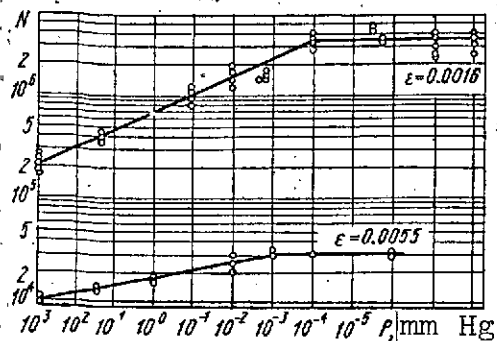


Figure 5. Fatigue life as function of vacuum level for $\epsilon = 0.0016$ and 0.0055 .

F region to the H region. These data agree with those obtained by Kemsley, who found that the stable slip bands disappear with transition from the low amplitude region to the high amplitude region [24].

Under vacuum conditions, the slip band density and stable band density are considerably higher than in air; for the same deformation amplitudes, the slip is more disperse and uniform, i.e., the experimental data obtained for $\epsilon = 0.0016$ are valid throughout the entire F region.

Under vacuum conditions, the number of stable bands also decreases with increase of the deformation amplitude; however, they disappear at higher deformation than in air ($\epsilon = 0.0032$). This phenomenon can be explained if we introduce the critical local plastic deformation ϵ^* , above which stable bands are not formed. Since plastic deformation takes place more uniformly in vacuum than in air, higher macroscopically averaged deformation will correspond to the value ϵ^* . This then is apparently the reason for the fact that the stable bands are retained up to higher deformation amplitude in vacuum than in air. /33

Thus, transition from the F region to the H region under vacuum conditions takes place at higher deformations. This conclusion is very important in connection with explanation of the influence of vacuum on the fatigue failure process. As was mentioned above, increase of the fatigue life in vacuum is explained by various authors [5 — 9, 14, 22] by slowing of crack propagation as a result of the local effects associated

with oxygen adsorption at the crack tip. If everything were actually determined by this factor alone, the $\epsilon - N$ curve, together with the characteristic points, would be shifted along the fatigue life axis. However, we see from the results obtained that the shift of the $\epsilon - N$ curve, at least the F branch of this curve, in vacuum takes place along the deformation axis. This means that it is the plastic deformation and its distribution which determine copper fatigue failure characteristics in vacuum in the low amplitude loading region.

Let us examine the dependence of fatigue life on vacuum level in the F and H regions. The nature of fatigue life dependence on surrounding medium pressure is the same for low and high deformations (Figure 5): as the vacuum is increased, the fatigue life increases linearly; beginning at some value P_{cr} , the life no longer depends on pressure and saturates. The differences are that, for $\epsilon = 0.0055$, the curve lies lower and saturates at a pressure of 10^{-3} mm Hg, while for $\epsilon = 0.0016$, the critical pressure is equal to 10^{-4} mm Hg.

The magnitude of the critical pressure for which the $\lg N = f(\lg P)$ curve saturates is determined, on the one hand, by the rate of oxygen adsorption on the slip steps and, on the other hand, by the rate of dislocation emergence to the surface.

Let us try to estimate how the critical pressure changes with deformation amplitude change. From what we have said,

$$P_{cr} = v_s = \alpha v_d, \quad (1)$$

where P_{cr} is the critical pressure, v_s is the oxygen adsorption rate at the pressure P_{cr} , v_d is the average rate of dislocation emergence to the surface per quarter cycle, α is a constant.

The rate of dislocation emergence is obviously proportional to the average plastic deformation rate per quarter cycle $\dot{\epsilon}_{pl}$;

$$v_d \sim \dot{\epsilon}_{pl} \sim \omega \epsilon_{pl}, \quad (2)$$

where ω is the loading frequency, ϵ_{pl} is the plastic deformation amplitude.

From (1) and (2) follows $P_{cr} \sim \omega \epsilon_{pl}$. Since we have considered here the fatigue life dependences on vacuum level for two deformation amplitudes, $P'_{cr}/P''_{cr} = \epsilon'_{pl}/\epsilon''_{pl}$. In our experiments for $\epsilon_1 = 0.0055$, the plastic deformation amplitude was $\epsilon'_{pl} = 0.00310$, for $\epsilon_2 = 0.0016$, $\epsilon''_{pl} = 0.00034$. Thus, $P'_{cr}/P''_{cr} \approx 10$.

It follows from this discussion that, with deformation amplitude increase from 0.0016 to 0.0055, the critical pressure shifts by an order of magnitude into the region of higher pressures, which is in complete agreement with the experimental data.

Figure 6 shows the dependence of the relative increase of the fatigue life n in vacuum in comparison with air on the deformation magnitude $n = N_v/N_a^0$, where N_v is the fatigue life in vacuum, N_a^0 is the fatigue life in air.

On the curve, we can identify three characteristic segments: the segment FF for which $n \approx 10$ and does not change with deformation change from 0.0012 to 0.0019; the segment HH on which n varies smoothly from 4 to 3, saturating with deformation increase from 0.0032 to 0.0070; the segment FH with deformation 0.0019 — 0.0032, and marked dependence of n on deformation amplitude. /34

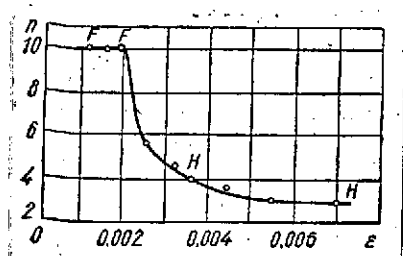


Figure 6. Dependence of relative fatigue life increase in vacuum on deformation amplitude.

In the deformation region corresponding to the segment FF, failure is characterized by the low amplitude mechanism both in air and in vacuum. In the HH region, the high amplitude failure mechanism holds, both in vacuum and in air. The FH region is transitional — since failure in air takes place following the 'H' mechanism while in vacuum it follows the F mechanism,

The influence of vacuum on fatigue life in both the H and F regions is associated with changes in the near-surface layer. These changes take place as a consequence of interaction of the oxygen of the surrounding medium with the freshly formed slip steps; the nature of fatigue life dependence on vacuum level is the same over a wide deformation range and is determined by near surface layer formation kinetics as a function of ambient pressure and deformation amplitude.

Reduction of vacuum influence on fatigue life with deformation amplitude increase can be expected on the basis of the following arguments. The near surface layer effectiveness will increase with deformation amplitude increase so that the additional changes in its formation under the influence of vacuum becomes less important. However, while the relative fatigue life increase within the limits of a deformation region with the same failure mechanism depends weakly on deformation magnitude, upon transition from low amplitude to high amplitude failure, we observe a large dependence of n on the deformation amplitude. This is probably associated with the fact that, during cyclic loading in vacuum, the changes in formation of the near surface

layer may lead to fatigue life increase in a different fashion, depending on the specific fracture mechanism. In the H region (possibly following the Kramer mechanism) under vacuum conditions plastic relaxation of the stresses at the crack tip is facilitated, which leads to the observed fatigue life increase by a factor of three or four, in comparison with fatigue life in air. In the F region, reduction of the near surface layer effectiveness in vacuum leads to more uniform distortions and discontinuity accumulation in the stable slip bands. This reduces the probability of fatigue fracture, as a result of which fatigue life increases by an order of magnitude in comparison with fatigue life in air.

Influence of vacuum on the copper fatigue fracture process in various stages. In studying the influence of vacuum on fatigue properties, we use as the criterion the ratio of specimen fatigue life in vacuum to that in air $n = N_v/N_a$. However, the quantity n characterizes only the average influence of vacuum on the fatigue fracture process during the entire cyclic loading period. It is of interest to examine the influence of vacuum in the various stages of the process.

In order to determine the role of vacuum in the various stages of the fatigue process, we made tests in air for a given number of cycles, after which we determined the fatigue life of these specimens in vacuum. As the parameter defining the influence of vacuum on fatigue fracture, we took the quantity $\bar{n} = N_v/(N_a^0 - N_a)$, where N_v is the fatigue life in vacuum of specimens which have first been deformed in air; N_a^0 is the specimen fatigue life in air; N_a is the number of preliminary loading cycles in air.

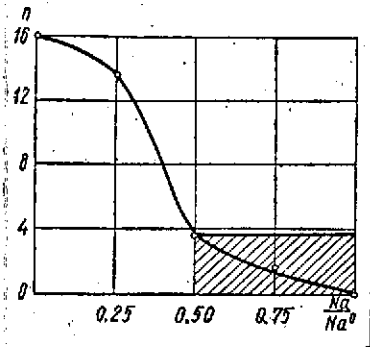


Figure 7. Dependence of \bar{n} on number of preliminary loading cycles in air for $\epsilon = 0.0012$.

In other words, \bar{n} is the ratio of fatigue life in vacuum of specimens which have first been deformed in air to the assumed residual fatigue life in air and characterizes the effect of vacuum in the stage from N_a to failure.

Figure 7 shows the dependence of the quantity \bar{n} for copper on the number of preloading cycles in air. We see from the figure that specimen fatigue life in vacuum increases by 16 times in comparison with the fatigue life in air without preliminary loading.

As the number of preliminary loading cycles is increased, the quantity \bar{n} decreases. For example, after 50% of the specimen life in air, i.e., at the stage $(0.5 - 1)(N_a/N_a^0)$, the quantity \bar{n}_2 amounts to only 3.5.

The influence of vacuum in the stage $(0 - 0.5)(N_a/N_a^0)$ can be estimated as follows:

$$\bar{n}_1 = \frac{N_v^0 - N_v^1}{N_a^1},$$

where N_v^0 is the fatigue life in vacuum of a specimen without preliminary loading; N_v^1 is the fatigue life in vacuum of a specimen which has been tested in air for 50% of its life; N_a^1 is the number of preliminary loading cycles.

On the basis of the fact that $N_v^0 = 16 N_a^0$, $N_v^1 = 3.5 \cdot 0.5 N_a^0$ (shaded region), $N_a^1 = 0.5 N_a^0$, $\bar{n}_1 = 29$.

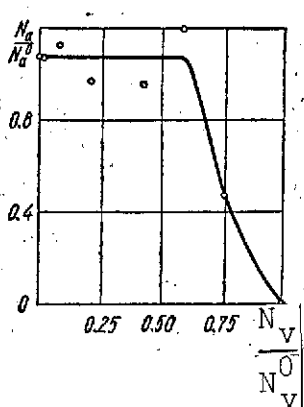


Figure 8. Dependence of fatigue life in air on number of preliminary deformation cycles in vacuum for $\epsilon = 0.0012$.

We see from the \bar{n} values presented (29 and 3.5), that the influence of vacuum in the first half of specimen life is nearly an order of magnitude greater than in the last 50% of the fatigue life.

Thus, the influence of vacuum is not the same in the various stages of the fatigue process in copper and is most significant in the initial stage. Figure 8 shows

the dependence of fatigue life in air of copper specimens which have been first deformed in vacuum on the number of preliminary loading cycles. We see from these data that deformation in vacuum up to 60% of the fatigue life does not alter noticeably the subsequent fatigue life in air. Thus, the specimen loaded for $1.35 \cdot 10^7$ cycles has the same fatigue life in air as the specimen without preliminary loading. This apparently indicates that significant damage does not develop with cyclic deformation of copper in vacuum during a very long stage of the process. As we see when comparing the curves in Figures 7 and 8, the fatigue damage accumulation process takes place differently in air and in vacuum, which is confirmed by the data shown in Figure 9, where the degree of damage during preliminary loading in air and in vacuum is characterized by the magnitude of the fatigue life during subsequent testing in air in the high amplitude region ($\epsilon = 0.003$) with quasistatic nature of the failure.

/36

It follows from these data that loading in air in the low amplitude region ($\epsilon = 0.0012$) reduces the cyclic strength in high amplitude deformation from the very initial deformation

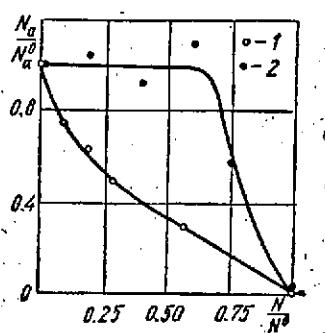


Figure 9. Dependence of fatigue life in air for $\epsilon = 0.0030$ on number of preliminary loading cycles in air and in vacuum for $\epsilon = 0.0012$.

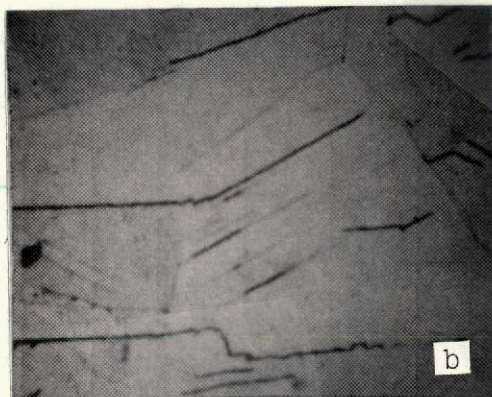
1- pressure 760 mm Hg; 2- pressure 10^{-7} mm Hg.

stages... At the same time, loading in vacuum for up to 60% of the specimen fatigue life does not lead to any change of the cyclic strength in high amplitude deformation. It is interesting that the strength reduction of specimens which have been deformed in vacuum for 75% of their life under these conditions is the same as for specimens which have been deformed in air for only 25% of their life, or in absolute units, the specimen withstands $4.5 \cdot 10^5$ cycles in air while it withstands $1.58 \cdot 10^5$ cycles

in vacuum for the same degree of damage.

It was of interest to clarify exactly what the differences are between the damage accumulation processes during cyclic loading in air and in vacuum. Metallographic study showed that, after testing in air for $5.4 \cdot 10^4$ cycles (3% of the fatigue life), cracks appear at the boundaries of the crystal twins, although stable slip bands have not yet appeared. After $1.44 \cdot 10^5$ cycles (8% of the fatigue life), when stable slip bands have formed, we can detect cracks which extend beyond the limits of a single grain (Figure 10a). With further deformation, in air, we observe longer cracks encompassing several grains.

In a vacuum, the stable slip bands appear only after $7.2 \cdot 10^5$ cycles. Cracks were not detected after testing the specimen for $1.8 \cdot 10^6$ cycles (8% of the fatigue life), although in air after this same period, the fatigue fracture process had



Reproduced from
best available copy.

Figure 10. Cracks and stable slip bands in different cyclic deformation stages.

a- in air after $1.44 \cdot 10^5$ cycles (8% of fatigue life);

b- in air after $1.8 \cdot 10^6$ cycles (100% of fatigue life);

c- in vacuum after $9 \cdot 10^6$ cycles (40% of fatigue life).

culminated (Figure 10b). In a vacuum, the first cracks appear only after $9 \cdot 10^6$ cycles (Figure 10c); with further cycling, the cracks elongate, transitioning from one grain into another. /37

These data confirm the concept that development of the fatigue process takes place differently, depending on the surrounding atmosphere. In air, microcracks appear in the specimens in the very early stages of the fatigue process, constituting less than 10% of the total specimen lifetime. In this case, the fatigue failure actually is basically the crack propagation process, which is noted in studies by Thompson [25], Wood [23], and other investigators. However, in vacuum, the microcracks form far later than in air, both with respect to absolute number of loading cycles and relative to specimen total fatigue life under corresponding conditions.

It is usually considered that the formation of stable slip bands is evidence of fatigue cracks nucleation and the appearance of microcracks corresponds to transition to the crack propagation stage. On this basis, we can assume that vacuum has a dual influence on the initial stage of the fatigue process: it retards crack nucleation and delays the beginning of the crack propagation stage. Hence it follows that the known data [25] indicating that crack nucleation is replaced very rapidly by crack propagation relates only to the case of cyclic loading under atmospheric conditions. These concepts do not correspond to the case of fatigue failure in pure form (without influence of the atmosphere), in which the crack propagation stage duration is approximately equal to that of the preceding stage.

It was shown above that, in the case of cyclic loading of copper, the plastic deformation model is different, depending on the surrounding medium: in air, slip is nonuniform and plastic deformation is localized in a comparatively small number of slip planes; in vacuum, slip takes place more uniformly and is distributed in numerous slip bands. It appears that this is the reason for the reduction of critical crack nucleus formation probability under vacuum conditions.

On the basis of this analysis, we can come to the following conclusions.

The most significant effect of vacuum on the fatigue failure of copper is reduction of the plastic deformation concentration in individual slip bands and activation of a large number of these bands. Increase of fatigue life of the metals, change of the relationship between the fracture process development stages in copper, and increase of the deformation for transition from the F region to the H region are consequences of this basic influence.

The influence of vacuum on the fatigue fracture process of copper begins in the early cyclic loading stages and does not amount simply to localization of oxygen interaction with the freshly formed surfaces at the crack tip as the crack advances.

Fatigue fracture in the pure form is not basically a crack propagation process, as is usually thought on the basis of experiments conducted in air. In vacuum, the fracture stages prior to initiation of crack propagation constitute a considerable portion of specimen fatigue life (for example, about 50% of the fatigue life of copper).

REFERENCES

1. Boychuk, V. M., et al. Fiziko-khimicheskaya mekhanika materialov, Vol. 4, No. 6, 1968.
2. Amelin, E. A., et al. Author's certificate No. 256,324, cl. 42K, 34/05. Byul. otkrytiya, izobreteniya, promyshlennye obraztsy, tovarnyye znaki, No. 34, 1969.
3. Verkin, B. I., et al. Trudy FTINT (Physico-Technical Institute of Low Temperatures) of the Academy of Sciences UkSSR), Vol. 4, 1968.
4. Boychuk, V. M. Problemy prochnosti, Vol. 4, 1971.
5. Wadsworth, N. T. In the book: Ustaloste i vyнослиvoste metallov (Fatigue and Endurance of Metals). Moscow, 1963.
6. Hordon, M. I. Acta Metallurgica, Vol. 14, No. 10, 1966, pp. 1173-1178.
7. Shen, H., S. E. Podlaseck, and I. R. Kramer. Acta Metallurgica, Vol. 14, No. 3, 1966, pp. 341-346.
8. Snowden, K. U. Acta Metallurgica, Vol. 12, No. 3, 1964, pp. 295-303.

9. Ham, I. L., and G. S. Reichenbach. Symposium Materials for Aircraft. Amer. Soc. Test. and Mater., Philadelphia, Pa., 1963.
10. Jacisin, I. M. Trans. Met. Soc., AIME, Vol. 239, No. 6, 1967, pp. 821-823.
11. Engelmaier, W. Trans. Met. Soc., AIME, Vol. 242, No. 8, 1968, pp. 1713-1718.
12. Steverding, B. Review of Scientific Instruments, Vol. 35, No. 5, 1964, pp. 565-568.
13. Smith, H. H., A. Shaninian, and M. R. Achter. U. S. Nav. Rev. Lab. Rep., N. R. L. Progr., 1966, Aug, 23-24.
14. Morecraft, D. W. Vacuum, Vol. 18, No. 3, 1968, pp. 164-165.
15. Wadsworth, N. T. Phil. Mag., Vol. 63, No. 6, 1961, pp. 397-401.
16. Snowden, K. U. Nature, Vol. 189, No. 53, 1961, p. 4758.
17. Grosskreutz, I. C., and C. Q. Bowles. Environment-Sensitive Mech. Behavior of Mat., eds. Westwood and Stolloff, 1967.
18. Wadsworth, N. T., and T. Hutchings. Phil. Mag., Vol. 3, No. 34, 1958, pp. 1154-1166.
19. Robertson, I. A. Trans. Met. Soc. AIME, Vol. 235, 1965, pp. 1799-1801.
20. Snowden, K. U. J. Less Common Metals, Vol. 7, 1964, p. 84.
21. Meyn, D. A. Naval U.S. Res. Lab. Rept. N. R. L. Progr., 1966, May 20-21.
22. Martin, D. E. Trans ASME, Vol. D87, No. 4, 1965, p. 850.
23. Wood, W. A. Inst. Metals., Vol. 91, 1962-1963, pp. 225-229.
24. Kemsley, D. S. J. Inst. Metals, Vol. 85, No. 4, 1956-1957, p. 153.
25. Thompson, N., N. Wadsworth, and N. Louat. Phil. Mag., Vol. 1, No. 2, 1956, pp. 113-126.

INFLUENCE OF LOW TEMPERATURES ON FRICTION AND WEAR

V. F. Udovenko and G. N. Presnyakova

A brief review of studies on low-temperature friction is presented. A facility and technique for studying friction both in air and in vacuum at temperatures of $+20^{\circ}$ and -190° C is described. Results of a wear study of 110 G13L structural steels operating together with 40Cr steel are presented. It is shown that reduction of the test temperature in vacuum leads in certain cases to marked increase of the wear magnitude and friction coefficient, which is associated not only with the general change of the mechanical properties of the materials but also with the influence of temperature reduction on the hardening and structure formation which take place in the surface layers during friction.

The development of cryogenic technology and exploration of /38 outer space and the far north are expanding the field of application of machines and mechanisms operating at low temperatures. As is well known, temperature reduction leads to marked change of the physical and mechanical properties of materials. In the metals, there is restructuring of the crystal lattice and some materials experience phase transition into the solid state, which may be accompanied by abrupt change of the mechanical properties, and the nature of the plastic deformation, magnetic, thermoelectric, and other physical properties change [1, 2].

Since the wear resistance of friction pairs is determined by the mechanical properties and the ability of the material to form efficient secondary structures, which is directly associated with the physical properties of the material, temperature reduction may have significant influence on friction behavior and wear dynamics. Of particular interest is study of the friction process at low temperature in vacuum, under conditions of degraded heat rejection and absence of an oxidizing medium, since transition to vacuum leads in itself to change of the friction properties of materials.

In spite of the urgency of the problem, very little study has been made of low temperature friction. In connection with the specific nature of the operation of friction pairs and components, the studies on friction at cryogenic temperatures are subdivided into studies in liquified gases, in inert gas atmospheres, and in vacuum. Most studies have been devoted to investigations of friction of the pure metals. The results of many of these studies are contradictory [3, 4, 5]. The structural steels have received far less study. Among the significant studies we can mention that of Golego [6] on friction of steel 45 in air and in an argon atmosphere with liquid nitrogen cooling of the specimens, and the study of Dychko [7] on friction of steels under Siberian winter conditions (air, temperature -25 to -30° C).

We designed a facility and developed a testing technique to study the wear mechanism at low temperatures in various gaseous media and in deep vacuum, and also to determine the efficiency of a broad class of materials (metals, alloys, plastics, etc.). /39

The facility is a high vacuum chamber within which there is located a miniature low temperature friction testing machine (Figure 1a). The vacuum (down to 10^{-9} tor) in the chamber is created by cryogenic condensation pumps. Annular condensation pumps which surround the object under test to the maximal extent

The miniature low temperature friction testing machine (Figure 1b) is made in the form of two coaxial units: the shaft input unit and the vacuum manipulator, mounted, respectively, on the lower and upper chamber covers. In designing this machine, we considered the peculiarities of specimen cooling in vacuum. The absence of convectional heat transfer and heat transport in vacuum leads to a situation in which change of the specimen temperature can take place only as a result of contact with cooled structural elements and radiant heat transfer. Contact of the body with the coolant occurs only at individual points; therefore, specimen cooling in vacuum with significant reduction of the heat transfer will be a very long process. In the case of friction of /40 cooled specimens, when high local temperatures develop, there is danger of specimen heating. Therefore, when studying the friction process at low temperatures in vacuum, it is necessary to cool both elements of the friction pair in order to ensure adequate removal of the heat evolved during operation.

The moving specimen (ring) is mounted on the end of a rotating shaft which is inserted through the lower cover of the chamber. The shaft is driven through a V belt transmission from a multistage reducer located outside the chamber, which permits stepwise change of the specimen speed from 0 to 1000 rpm. The ring is cooled by liquid or gaseous coolant (nitrogen) which is fed into the copper vessel 1, coupled with the hollow shaft through the heat bridge 2, which is a teflon washer. The filler tube 3 is bonded through the heat bridge 8 to the lower end of the shaft. In the upper portion of the shaft, there are ports for evacuating the space between the filler tube and the shaft. The seals 4 and 6 are cooled by means of the copper sleeves 5 and 7, seated on the filler tube.

The stationary specimen (indenter) is attached to the vacuum manipulator which is mounted on the upper cover and is intended for transmission of normal load to the friction pair and measurement of the friction torque by the "entrainment" method. The indenter is cooled by the same technique as the ring. Mounting of the specimens directly on the nitrogen vessel provides good thermal contact, which is achieved not only by forcing the specimens together, but also by using Wood's alloy to fill the recess in which the specimens are seated. The friction force is measured by a dynamometer or by a force friction measuring instrument [10], located outside the chamber. Transmission of the friction torque from the vacuum to the measurement system is accomplished by the vacuum manipulator, whose own friction torque can be small enough so that the error resulting from this torque will be slight.

The specimen temperature is measured by chromel-kopel thermocouples and recorded by a potentiometer. The indenter temperature can be measured throughout the entire experiment; that of the ring

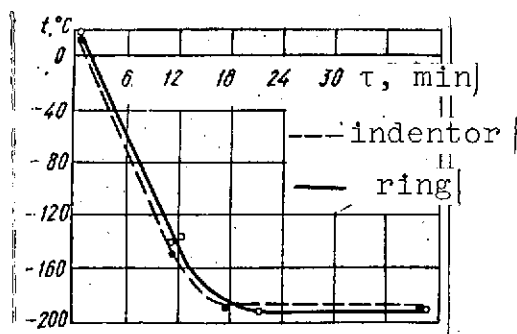


Figure 2. Specimen temperature versus cooling time.

can be measured only prior to initiation of rotation. It was found (Figure 2) that the specimen temperature reaches -190°C 25 to 30 minutes after initiating nitrogen flow into the holders of both specimens in the case when the specimens are not bonded using Wood's alloy. However, if only one specimen is cooled (either ring or indenter), the temperature of

the other specimen which is brought into contact with the first will be considerably higher than -190°C . As will be shown later, the wear magnitude and friction coefficient will be different than in the case when both specimens are cooled. By regulating the

nitrogen flow into the specimen holders, we can obtain any intermediate temperature from 0 to -190° C.

This design makes it possible to conduct tests of materials over a wide range of conditions. On the one hand, the design provides the possibility of varying specimen temperature at $+20$ and $+100$ to -190° C and the ambient temperature; on the other hand, it is possible to vary the gaseous medium composition by pumping the selected gaseous medium through the inflow valve into the chamber under varying pressure — from atmospheric to 10^{-7} tor.

This technique was used to study wear resistance of materials under conditions simulating the far north (dry air, temperature -60 to -80° C), and in high vacuum at $+20$ and -190° C. For the study, we selected the 110G1ZL high manganese austenitic steel, /41 which is widely used in machines and mechanisms operating in the north. We studied the wear resistance of the 110G1ZL steel in friction with bonded abrasive and dry friction of 110G1ZL steel on 40Cr steel.

The experimental setup was the same in both cases. We tested an open friction pair consisting of ring and indenter with overlap coefficient close to zero with 5.2 kG normal load on the friction pair.

When studying abrasive wear, the indentors were fabricated from 110G1ZL steel and the rings were pressed abrasive (sand). These tests were conducted at a single sliding velocity $v_{sl} = 0.44$ m/sec along a friction path of 500 m. The tests results are shown in Table 1.

The greatest ring and indenter wear occurred for specimen friction in a dry cold air atmosphere, and the friction coefficient in this case varied considerably in the indicated limits. Wear in

TABLE 1
RESULTS OF 110G1ZL STEEL TESTING WITH ABRASIVE
IN AIR AND VACUUM

Test Conditions		Friction coefficient	Wear, g/km		Indenter friction surface micro-hardness, H_d , kg/mm ²
Medium	t, °C		Ring	Indenter	
Vacuum $5 \cdot 10^{-7}$ tor	-190	0.27	0.3984	0.1238	890
Vacuum $5 \cdot 10^{-7}$ tor	+20	0.88—0.98	Very little	0.1022	860
Dry air	-60— -80	0.39—0.67	1.1496	0.2560	600
Air	+20	0.69—0.74	0.6630	0.1770	590

vacuum and in vacuum with cooling was less than in air, while wear in vacuum at -190° C was somewhat greater than at room temperature. Measurements of friction surface microhardness showed a greater degree of hardening for testing in vacuum than in air. Comparing the magnitudes of the wear and working surface hardening, we can assume that the reduction of steel wear for testing in vacuum is explained by the more intense hardening of the surface during friction. It is interesting to note that the abrasive itself wore differently in the conditions investigated. It is probable that the properties of the abrasive itself change with transition to vacuum, probably as a result of dehydration.

In the investigation of 110G1ZL steel dry friction on 40Cr steel, we studied the influence of sliding velocity (in the velocity interval from 0.11 to 0.75 m/sec). The indentors were made from 110G1ZL steel (basic structure austenite) and the rings from 40Cr steel (basic structure martensite). The wear was determined along a one-kilometer friction path for the same normal load as in the first case, namely 5.2 kG. The experimental data obtained are shown in Table 2.

TABLE 2
RESULTS OF 110G1ZL STEEL TESTING WITH 40Cr STEEL
AT ROOM AND LOW TEMPERATURES IN AIR AND IN VACUUM

v_{sl} m/sec	Test conditions		Wear, g/km		Friction coefficient
	Medium	$t, ^\circ C$	Indentor	Ring	
0.11	Vacuum $5 \cdot 10^{-7}$ tor	+20	0.0027	0.1632	0.6—0.7
		-190	0.0050	3.3626	0.95
		$\frac{-190^*}{+20}$	0.0122	0.7572	0.75—0.85
		$\frac{+20}{-190}$	0.0087	2.2268	0.95
	Air	+20	0.0060	0.0021	0.56
		-190	0.0073	0.0018	0.56
0.21	Vacuum $5 \cdot 10^{-7}$ tor	+20	0.0028	0.0600	0.58
		-190	0.0077	2.2726	0.8—0.9
	Air	+20	0.0102	0.0063	0.47—0.57
		-190	0.0087	0.0017	0.45
0.44	Vacuum $5 \cdot 10^{-7}$ tor	+20	0.0014	0.0497	0.52
		-190	0.0027	0.0430	0.52
	Air	+20	0.0114	0.0028	0.59—0.75
		-190	0.0083	0.0004	0.43
0.75	Vacuum $5 \cdot 10^{-7}$ tor	+20	0.0097	0.0172	0.78
		-190	0.0047	0.0185	0.58
	Air	+20	0.0082	0.0020	0.5
		-190	0.0133	+0.0008	0.4

*Numerator is indentor temperature, denominator is ring temperature.

On the basis of the Bowden-Kragel'skiy adhesion-deformation theory of friction, we can assume that, with reduction of the test temperature, the adhesion component of the friction force and consequently the friction coefficient will decrease because of metal surface hardness increase. In fact, this occurs in friction

of the pure metals [11]. However, we obtained contradictory results in the case of steel friction. It is likely that, in the heterogeneous systems, where structure formation and surface phase hardening during friction become important, there are peculiarities which influence the dynamics of the process. The data of Table 2 indicate significant increase of 40Cr steel wear when transitioning to operation in vacuum at low temperature, while 110G1ZL steel wear increases, but to a far smaller degree. We explained these results from the viewpoint of the theory of active layer hardening and softening during friction. In order to determine the degree /42 of working surface hardening, we measured the microhardness on a PMT-3 instrument, and the active layer phase composition change was determined by x-ray structural analysis and metallography [12]. Since the characteristic feature of 110G1ZL steel is formation of deformation martensite (α'' phase) as a result of deformation and the amount of this phase depends on the degree of deformation and temperature, this quantity can serve as an indicator for determining deformation intensity. It was found that the largest amount of α'' phase is formed on the friction surface during testing in vacuum with cooling, which indicates the more intense hardening of the surface of this steel during friction under /43 these conditions (Figure 3).

In comparing the wear data with the data on working surface hardening (Figure 4), the increase of 40Cr steel wear at low sliding velocities at -190°C was explained not only by general embrittlement of the material with transition to negative temperature, but primarily by the absence of conditions for formation of a hardened protective layer on the friction track because of low plasticity of the basic structure. In this case, the thermal asymmetry of the friction pair became important. The external appearance of the friction surface (Figure 5) made it possible to suggest the following wear mechanism. The particles which harden to some degree and flake off from the ring surface embed

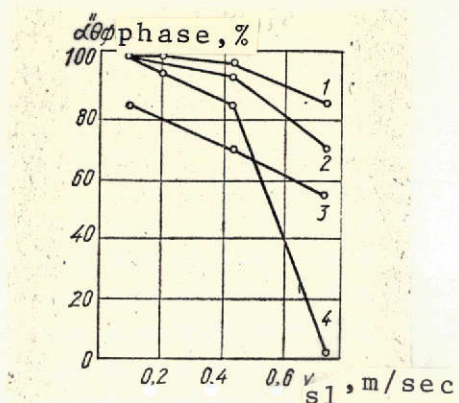


Figure 3. Influence of friction conditions on formation of deformation martensite in indenter working layer.

1- vacuum $5 \cdot 10^{-7}$ tor, $t = -190^\circ \text{C}$; 2- air, $t = -190^\circ \text{C}$; 3- air, $t = +20^\circ \text{C}$; 4- vacuum $5 \cdot 10^{-7}$ tor, $t = +20^\circ \text{C}$.

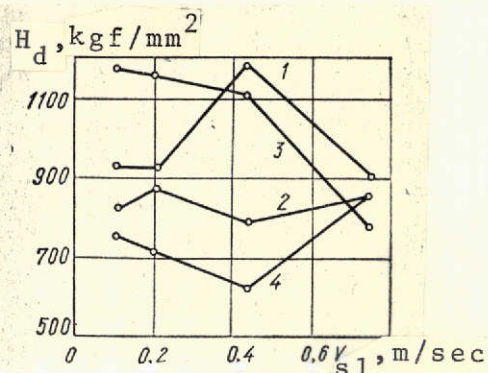
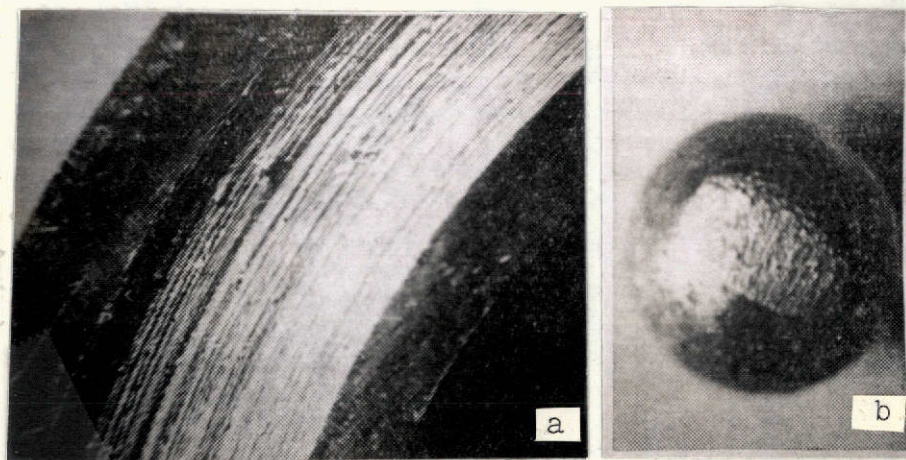


Figure 4. Hardening of ring surface after friction under different conditions.

1- vacuum $5 \cdot 10^{-7}$ tor, $t = -190^\circ \text{C}$; 2- air, $t = -190^\circ \text{C}$; 3- vacuum $5 \cdot 10^{-7}$ tor, $t = +20^\circ \text{C}$; 4- air, $t = +20^\circ \text{C}$.



Reproduced from
best available copy.

Figure 5. External view of friction surface after operating in vacuum at $t = -190^\circ \text{C}$ ($v_{sl} = 0.11 \text{ m/sec}$) $\times 4$.

a- ring; b- indenter.

themselves into the softer indenter surface and, acting like an abrasive coating, cut the ring.

It was found that test temperature reduction in vacuum leads to increased wear only up to a quite definite sliding velocity (0.44 m/sec). It is possible that, even at this velocity, the conditions at the friction surface (primarily temperature) become the same when testing both with cooling and without cooling. This assumption is indirectly confirmed by the same magnitude of the wear and friction coefficient and the same external appearance of the working surface.

REFERENCES

1. Gudkov, S. I. Mekhanicheskiye Svoystva stali pri nizkikh temperaturakh (Mechanical Properties of Steel at Low Temperatures), Metallurgiya Press, Moscow, 1967.
2. Uzhik, G. V. Prochnost' i plastichnost metallov pri nizkikh temperaturakh (Strength and Plasticity of Metals at Low Temperatures). Izdatel'stvo AN SSSR, Moscow, 1957.
3. Barton, R. A., J. A. Russel, and P. M. Ku. Wear, 1962, p. 5.
4. Simon, I., I. O. McManon, and R. J. Bowen. J. of Appl. Phys., Vol. 22, 1951, p. 2.
5. Karapetyan, S. S., et al. DAN SSSR, Vol. 192, 1970, p. 5.
6. Golego, N. L. Skhvatyvaniye v mashinakh i metody ego ustraneniya (Seizure in Machines and Methods for Eliminating Same). Tekhnika Press, Kiev, 1965.
7. Dychko, A. A. In the book: Trudy OMIIT (Transactions of the Omsk Institute of Railroad Transportation Engineers). Vol. 43, 1963, p. 2.
8. Bagrov, N. N., et al. ZhTF, Vol. 37, 1967, p. 1105.
9. Baryshova, N. M. PTE, Vol. 6, 1965, p. 139.
10. Kurilov, G. V., et al. Zav. Lab., Vol. 9, 1968, p. 1127.
11. Bowden, F. and T. H. C. Childs. Proc. Roy. Soc., Vol. 312, 1969.
12. Presnyakova, G. N., et al. MITOM, Vol. 3, 1971.

INFLUENCE OF DEGREE OF AMBIENT MEDIUM RAREFACTION ON
DEFORMATION OF COPPER AND ALUMINUM

I. M. Lyubarskiy, A. A. Guslyakov, A. V. Ashukin,
and V. I. Kuleba

The influence of high vacuum $1 \cdot 10^{-9}$ torr on the plastic deformation of copper and aluminum is studied. When stretching polycrystalline aluminum and copper specimens in vacuum the deformation at failure increases and the ultimate strength decreases. Deformation in vacuum is accompanied by the evolution of hydrogen. For copper, gas evolution is observed only at failure, while for aluminum hydrogen evolution takes place in the initial stage and the gas evolution peaks correspond to small steps on the deformation curve.

It is well known that reduction of the surrounding gaseous /44 medium pressure may lead to change of the strength characteristics of metallic materials. For example, for monocrystalline aluminum, whose specimens were oriented so that during tension in air the first hardening stage was absent, deformation in 10^{-8} — 10^{-9} torr vacuum led to the appearance of the first hardening stage and reduction of the slope of the second hardening stage. For polycrystalline aluminum specimens, the yield point decreased and the total elongation to failure increased [1, 2]. For polycrystalline molybdenum, pressure reduction to 10^{-10} torr did not influence the yield point, although it did lead to increase of the deformation to failure by 30% [3, 4].

During deformation of molybdenum, aluminum, and magnesium in vacuum [3, 4], release of hydrogen and methane was observed and the gas evolution peak corresponded to the elastic limit.

This effect of high vacuum can be explained by the somewhat different behavior of the dislocations in the near surface layer [5 — 7] in comparison with their behavior under atmospheric conditions. Actually, the surface influence shows up in the development of an effective stress field which hinders dislocation movement in this layer. The presence of oxide and other contaminating films on the surface causes additional increase of the height of the potential barrier which the dislocations must overcome to emerge through the surface [17]. This leads to inhibition of metal plastic flow. Moreover, the stress concentration in the near surface layer resulting from the presence of the contaminating films facilitates crack formation, which causes failure at considerably smaller deformation than in the clean metal surface case [5]. Therefore, during deformation under high vacuum conditions, when the formation of oxide and other contaminating films is inhibited, we should observe increase of the plastic flow and increase of the deformation prior to failure. The gas evolution during deformation can be explained both by gas desorption from the surface as a result of surface stresses [3, 4], and by gas evolution from the interior during microcrack formation, entrainment of gaseous atmospheres by dislocations, and so on. In this connection, study of metal plastic deformation in high vacuum with simultaneous determination of gas evolution from the specimens is of definite interest.

The experimental setup for studying the influence of vacuum on the plastic properties (Figure 1) consists of a chamber and evacuation unit with cryogenic helium pump surrounded by a nitrogen shield, both of which can be heated to 400° C. The roughing evacuation system consists of a forevacuum pump and two diffusion

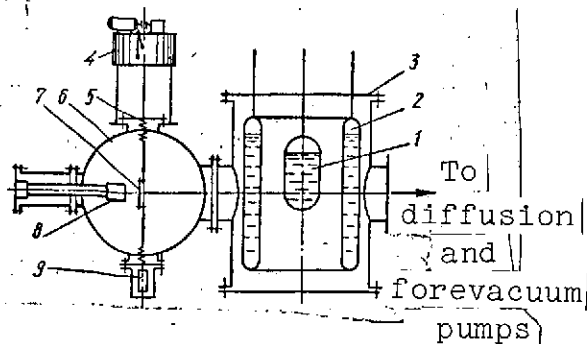


Figure 1. Schematic of setup.

1- helium condensation pump;
2- shield; 3- evacuation
unit; 4- tensile testing
machine; 5- bellows; 6-
chamber; 7- specimen; 8-
ROMS-1 mass spectrometer
sensor; 9- dynamometer.

pumps connected in series [8]; this system is connected with the evacuation unit only during its preheating period in order to reduce contamination by oil decomposition products. The evacuating unit makes it possible to obtain a pressure of $5 \cdot 10^{-10}$ tor with inflow $2 \cdot 10^{-8}$ liter/tor/sec.

A miniature tensile testing machine of the rigid type [9], mounted on the upper flange of the chamber, was used to stretch the /45

specimen. The machine provides loads up to 200 kG at four constant strain rates, which can be switched during the deformation process. The load is transmitted into the chamber by a rod connected by a biaxial universal joint with the drive screw of the tensile testing machine reducer. The metering dynamometer is an elastic element of tubular form. In order to avoid outgassing of the resins which protect the strain gages against the influence of the ambient medium, the dynamometer is located outside the chamber and is rigidly connected with the lower rod and cylinder. The rod is sealed by a bellows. Since the dynamometer deformation is small, the bellows stiffness does not change during measurement and has no influence on measurement accuracy. The effect of atmospheric pressure on the load magnitude is determined by calibrating the instrumentation system prior to the experiment. Since the experiment is brief, atmospheric pressure changes can be neglected.

In order to monitor residual gas composition and determine gas evolution magnitude during deformation, an ROMS-1 [10] mass spectrometer sensor was located in the working chamber in the

immediate vicinity of the specimen, which increases gas evolution determination accuracy. For quantitative analysis of the partial components of the gases evolved during deformation, particularly H_2 , the setup was calibrated by the constant pressure method using diaphragms with orifices of different sizes mounted in the line connecting the working chamber with the evacuation unit.

The commercially pure polycrystalline copper and aluminum specimens tested had section $5 \times 1 \text{ mm}^2$ and working length 18 mm. In order to relieve the stresses which arise during machining, the specimens were first annealed in vacuum $5 \cdot 10^{-6}$ tor (aluminum at 400°C , copper at 700°C). Deformation of the specimens was accomplished at room temperature with constant deformation rate $\epsilon = 8 \cdot 10^{-4} \text{ sec}^{-1}$.

Figure 2 (upper part) shows the hardening curves obtained as a result of statistical analysis of the tension diagrams. We see from the figure that the deformation prior to failure in $1 \cdot 10^{-9}$ tor vacuum for aluminum is 10% higher than in air, while for copper the deformation in vacuum is 8% higher than in air. Figure 2 (lower part) shows the statistically analyzed hydrogen evolution curves. Outgassing was observed for the copper specimens only at the instant of failure. In the other tension stages, /46 the hydrogen evolution, if any, did not exceed the instrument error and merged with the background.

For the aluminum specimens, hydrogen evolution was observed in the initial stage. The gas evolution peak corresponds to approximately 3 — 4% deformation. Gas evolution peaks are observed at failure for the aluminum specimens, just as for the copper specimens.

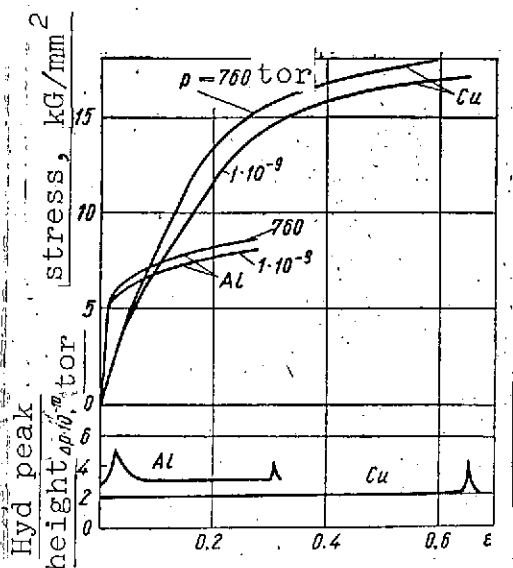


Figure 2. Curves of aluminum and copper hardening in air and in vacuum $1 \cdot 10^{-9}$ tor vacuum and hydrogen evolution curves.

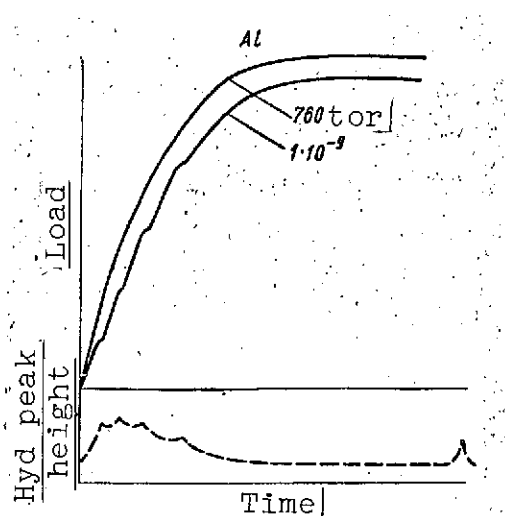


Figure 3. Tension diagrams of aluminum in vacuum and in air and hydrogen evolution curve.

Figure 3 shows the tensile curves of aluminum in vacuum and in air and the hydrogen evolution curve (dashed line). On the tension curve in vacuum, we see small steps which are not present during deformation in air. Each small step corresponds to a hydrogen evolution peak.

Metallographic studies of the specimens showed that during deformation in vacuum, the number of slip bands increases and the bands become finer and more uniformly distributed.

The strengthening action of surface films is determined by many factors which determine the nature of the interaction of these films with dislocations. In fact, the data of mass spectrometric measurements of residual gas composition indicate that in the bakeable vacuum chamber with cryogenic evacuation system, even at a pressure of $1 \cdot 10^{-7}$ tor, when the influence of vacuum on deformation is not yet marked, the oxygen content is insufficient for formation of an oxide monolayer on the freshly formed surface

in the course of the experiment time. Therefore, we can assume that the strengthening action of oxygen shows up, even for coatings amounting to a fraction of a monolayer. This can be explained by the fact that the clean metal surface is nonuniform in its properties [11] and oxide formation begins at low oxygen concentrations in individual regions having high chemical activity [12], possibly at dislocation emergence locations. In addition, the adsorbed gas films are probably also responsible for the strengthening effect. Since desorption of these gases depends significantly on the degree of rarefaction [13, 14], their influence may show up at lower pressures than the effect of oxygen.

The presence of the small steps on the deformation curves can be explained by simultaneous emergence of dislocation groups which were retarded by the surface and were located in the near surface layer. The emergence of such dislocation groups in aluminum is accompanied by entrainment of their gaseous atmospheres. This shows up in the appearance of the gas evolution peaks. With further deformation, the gas evolution decreases because of the fact that the dislocations begin to separate from their gaseous atmospheres. The gas evolution peak at failure is associated with gas evolution from the interior.

The absence of gas evolution in the initial stages of copper deformation makes it possible to assume that, for copper, the gaseous atmospheres are relatively weakly coupled with the dislocations. Therefore, even small stresses lead to separation of the dislocations from the gaseous atmospheres and their entrainment by the moving dislocations practically does not take place.

REFERENCES

1. Kramer, I. R., and S. Podlaseck. Acta Met., Vol. 11, 1963, p. 70.
2. Shen, H., S. Podlaseck, and I. R. Kramer. Trans. Met. Soc. AIME, Vol. 233, No. 11, 1965, p. 1933.
3. Feuerstein, S., L. Rice, and H. Conrad, Appl. Phys. Letts., Vol. 4, 1964, p. 154.
4. Feuerstein, S., and J. W. John. Appl. Phys., Vol. 40, No. 8, 1969, p. 3334.
5. Kramer, I. R., and L. Demer. Vliyanie sredy na mekhanicheskiye svoystva metallov (Effect of Environment on Mechanical Properties of Metal). Metallurgiya Press, Moscow, 1964.
6. Chvstvitel'nost' mekhanicheskikh svoystv k deystviyu sredy (Sensitivity of Mechanical Properties to the Environment). (Collection). Mir Press, Moscow, 1969.
7. Kochanova, L. A., P. P. Fedoseyeva, and E. L. Shchukin. FKhMM, Vol. 6, No. 3, 1970, p. 43.
8. Hengevoss, I., and W. K. Huber. Vacuum, Vol. 13, No. 1, 1963, p. 1.
9. Pustovalov, V. V., et al. PTE, Vol. 2, 1967, p. 176.
10. Bagrov, N. N., A. G. Furmanskiy, and A. A. Guslyakov. PTE, Vol. 4, 1969, p. 136.
11. Gane, N., and F. R. Bowden. Appl. Phys., Vol. 39, No. 3, 1968, p. 1432.
12. Okisleniye metallov (Oxidation of Metals) (collection). Vol. 1, Metallurgiya Press, Moscow, 1968.
13. Dushman, S. Nauchnye osnovy vakuumnoy tekhniki (Scientific Foundations of Vacuum Technique). Mir Press, Moscow, 1964.
14. Levin, G. Osnovy vakuumnoy tekhniki (Fundamentals of Vacuum Engineering). Energiya Press, Moscow, 1969.

FRICTION AND WEAR CHARACTERISTICS OF CARBON STEELS IN VACUUM

B. I. Verkin, I. M. Lyubarskiy, V. F. Udovenko,
and A. A. Guslyakov

The nature of carbon steel friction and wear under vacuum conditions is described within the framework of general friction and wear theory. Friction is considered a dynamic process and wear is considered to be the result of a continuous sequence of transitions of the friction surface material from one state into another.

The friction process in vacuum is characterized by several 47 peculiarities associated with change of the physical and chemical processes of ambient gaseous medium interaction with the material of the friction pair. The absence of or at the very least, partial removal of the protective films, presence of direct metallic contact of the friction surfaces, and change of the heat transfer nature and other factors during friction in vacuum lead to increase of the adhesional component of the friction force and change of the wear mechanism. The thermodynamic and kinetic parameters change significantly and these changes, in turn, influence the structural and phase changes during friction in vacuum.

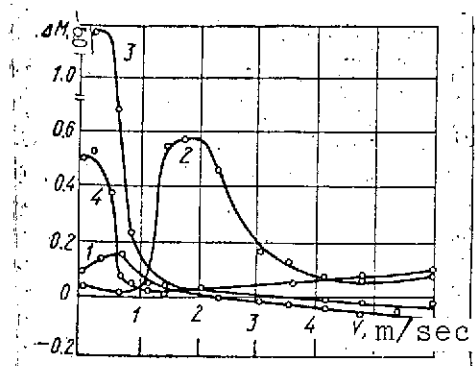


Figure 1. Wear of steel 45 indenter and ring for various sliding velocities.

1- ring wear, vacuum 10^{-7} tor; 2- indenter wear, vacuum 10^{-7} tor; 3- ring wear, atmosphere; 4- indenter wear, atmosphere.

In order to clarify the general laws governing the influence of vacuum on friction and wear characteristics, we conducted — under the guidance of B. I. Verkin and I. M. Lyubarskiy — studies of the friction and wear process of carbon steels (steel 45 and U8) over a wide range of velocities (0.1 — 6.3 m/sec) and pressures (760 — 10^{-7} tor) for an asymmetric ring indenter friction pair with overlap coefficient close to zero.

Figure 1 shows the results of the studies made on steel 45. From comparison of the curves, we see significant influence of the medium on wear magnitude.

Under atmospheric conditions, asymmetry of the friction pair elements has no significant effect on the wear process: maximal wear of both the ring and indenter is observed at low sliding velocities. With increase of the sliding velocity, the ring wear magnitude decreases sharply and becomes minimal. For velocities above 4 m/sec, we observe transfer of the indenter material to the ring. This wear process in air can be explained by the temperature conditions at the friction surface, which change both the oxidation process kinetics and the physical and mechanical properties of the metal.

During friction in vacuum, the ring wear is considerably less than in air throughout the entire velocity range studied. The wear reaches a maximum at low velocities, approximately 0.65 m/sec. Then it decreases smoothly, passes through zero, and

becomes negative because of indenter material transfer to the ring. On the whole, the ring wear process in vacuum is similar to ring wear in air.

Indenter wear in vacuum differs markedly from its wear in air: the wear becomes minimal rather than maximal at low velocities. In the velocity region 1.4 — 2.2 m/sec, we observe a definite wear maximum, then it decreases smoothly, remaining higher than in air.

Our results agree well with the data of Mies, who studied flat surface friction of similar steels in 10^{-4} — 10^{-5} torr vacuum for low sliding velocities (0.07 — 1.19 m/sec). The specimen wear in flat surface friction is similar to the ring wear in our case.

The observed behavior of the wear curves of asymmetric friction pair elements can be explained by the kinetics of the structural and phase transformations at the friction surface.

For low sliding velocities (up to 1.3 m/sec), the hardened /48 layer (specifically, the white zone) forms earlier on the indenter than on the ring. At a sliding velocity of 0.65 m/sec, conditions are realized on the ring friction surface which favor hardened layer formation and wear reduction. This leads, in turn, to rapid destruction of the hardened layer on the indenter and marked increase of its wear. With further increase of the sliding velocity, the friction surface is heated to a high temperature, at which the hardened layer does not form, and the plastic and adhesional properties of the metal increase. As a consequence of this, the mutual transport from one friction pair element to the other increases. The indenter mass wear decreases while the ring wear becomes negative. Further development of this

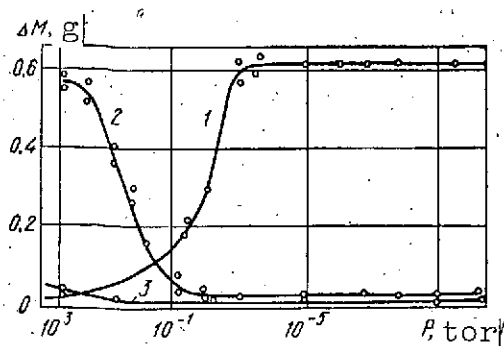


Figure 2. Mass wear of steel 45 indenter for various sliding velocities.

1- 2.4 m/sec (720 rpm); 2- 0.24 m/sec (72 rpm); 3- 1.4 m/sec (420 rpm).

The influence of the medium on wear magnitude is different for different sliding velocities. We can see this by examining the dependence of indenter wear magnitude on vacuum level for different sliding velocities (Figure 2). The selected velocities correspond to minimal indenter wear in vacuum, equal wear of the indenter and ring, and the maximal indenter wear. We see from the figure that regions of gaseous medium pressures ($1 - 10^{-3}$ torr) exist which are critical in regard to wear magnitude. Characteristic for low sliding velocities is reduction of the wear magnitude with vacuum depth, while for high velocities increase in comparison with the wear in air is typical. It is interesting to note the characteristic wear for the velocity 1.26 m/sec (velocity of equal wear of indenter and ring in vacuum): the wear remains low in both air and vacuum, although its nature changes markedly. Metallographic investigations showed that hardened structure formation depends significantly on the ambient pressure. For those sliding velocities for which the hardened structure forms, the higher the vacuum, beginning with 10^{-1} torr, the more clearly this structure forms.

Hardened structure formation has considerable influence on the friction coefficient as well, since the hardened structure which is formed reduces the adhesional properties of the steel and reduces the friction coefficient correspondingly.

process leads to a situation in which the magnitude of the indenter wear becomes equal to the ring weight increase, i.e., the overall mass wear of the friction pair becomes equal to zero.

The influence of the medium

on wear magnitude is different for different sliding velocities.

We can see this by examining the dependence of indenter wear magnitude on vacuum level for

For steel U8, we observe the same wear patterns, with the difference that the characteristic points (peak ring and indenter wear, point of equal ring and indenter wear) are shifted somewhat on the velocity scale. The results obtained indicate the following:

1. In spite of the fact that wear in vacuum differs from /49 wear under atmospheric conditions, the wear mechanism in vacuum can be explained on the basis of the adhesional-deformational theory of friction.

2. The adhesional component of the friction force begins to play the dominating role upon reaching a definite total pressure of the gaseous medium, when the rate of protective oxide film breakdown becomes commensurate with its rate of formation.

3. The structural changes which lead to hardened layer formation alter the magnitude of the adhesion and thereby alter the nature of the friction and wear process.

4. Thermodynamic asymmetry of the friction pair may lead to different structural transformations on the indenter and ring, which leads to difference in the nature of friction and wear in vacuum.

5. Change of the medium in which the friction and wear process takes place leads, in accordance with the general laws of physico-chemical mechanics, to changes of the mass wear relationships.

THERMAL REGIME AND TEMPERATURE STRESSES IN BODIES
DURING THERMORADIATIONAL HEATING

N. V. Chistop'yanova and V. L. Chumakov

An approach is developed to the application of the perturbation method for the solution of problems with essential external nonlinearities, based on identification in the boundary condition of a small nonlinear complex which is considered a perturbing function. The solutions obtained in the first approximation with error of 1-2% in calculating the unsteady temperature fields are then used to determine the temperature stresses and deformations in solid bodies of classical form.

The development of modern technology and particularly space /49 engineering has led to the necessity for solving several new problems of heat conduction, particularly problems with nonlinear boundary conditions. Closely associated with these problems are studies of the stress state and the strains caused by nonuniform heating of structural details and assemblies under conditions of large temperature gradients.

Heat transfer by radiation is exceptionally important in space vehicle calculations, since in airless space, there is no convective heat transfer during vehicle heating from the Sun and other external sources. A literature survey of the questions associated with radiational heating of bodies in space is presented in [1].

In order to study the thermoelastic stresses and strains, which is necessary for ensuring safe thermal loads with the lowest possible strength margin, we need to know the unsteady temperature distribution. When solving nonlinear heat conduction problems, we use approximate (numerical or analytic) techniques whose effectiveness depends on many factors. Recently, considerable attention has been devoted to the development of analytic methods which can compete successfully with the numerical methods for engineering calculations.

The characteristic feature of the present paper is study of the approximate solutions of the thermoradiational heating problem obtained on the basis of the disturbance method and the reduction of these solutions to a form convenient for use in the thermoelasticity problem.

Let us examine the dynamics of solid body heating by radiation with the boundary condition written in the dimensionless form:

$$(\nabla \theta)_{\text{S}} = \text{Sk} (1 - \theta_{\text{S}}^4) \quad (1)$$

where $\theta = T/T_c$ is the dimensionless temperature; $\text{Sk} = (\sigma_a T_c R)/\lambda$ is the Stark number; σ_a is the apparent radioactivity; T_c is the temperature of the medium; R is the defining dimension of the body; λ is the thermal conductivity; the subscript "s" refers to the surface of the body.

We write (1) in the form

$$(\nabla \theta)_{\text{S}} = \text{Bi}_\Sigma(q) [1 + \Phi(\theta_{\text{S}}, q) - \theta_{\text{S}}^4] \quad (2)$$

where

$$\text{Bi}_\Sigma = \text{Sk} (1 + q) \quad (3)$$

and the function

$$\Phi(\theta_{s_i}, q) = [\theta_{s_i} - \theta_{s_i}^4 - q(1 - \theta_{s_i})]/(1 + q) \quad (4)$$

is the nonlinear part of the condition (1). The linearization parameter q introduced here should be selected so that the influence of the parametric function Φ on the problem solution will be minimal. For this, it is necessary to set

$$q \approx \theta_{s_i} + \theta_{s_i}^2 + \theta_{s_i}^3 \quad (5)$$

For convenience of practical calculations, we can take as the quantity q the integral mean value of the polynomial (5)

$$q = \frac{1}{1 - \theta_{i1}} \int_{\theta_{i1}}^1 (\theta + \theta^2 + \theta^3) d\theta = \frac{1}{12} [13(1 + \theta_{i1}) + \theta_{i1}^2(7 + 3\theta_{i1})] \quad (6)$$

where θ_{i1} is the initial temperature.

We shall consider the nonlinear parametric function $\Phi(\theta_s, q)$ as the "disturbing" function. We introduce into the condition (2) the perturbation parameter ε ($0 \leq \varepsilon \leq 1$):

$$(\nabla \theta)_{s_i} = \text{Bi}_z(q) [1 + \varepsilon \Phi(\theta_{s_i}, q) - \theta_{s_i}] \quad (7)$$

For $\varepsilon = 1$, the condition (7) is identical to the original nonlinear condition (1), while for $\varepsilon = 0$, we have an "unperturbed" linear condition in the form of a boundary condition of the third kind, for which the basic solutions θ_0 of the thermal conduction problem for bodies of classical form are known.

Following the perturbation (small parameter) method, we seek the solution of the nonlinear problem with the boundary condition (7) in the form of the asymptotic expansion

$$\theta(\varepsilon) = \theta_0 + \sum_{m=1}^{\infty} \varepsilon^m \theta_m, \quad (8)$$

where the corrections θ_m ($m = 1, 2, \dots$) to the basic solution θ_0 are subject to determination.

Grouping terms of the same order in ε^m ($m = 0, 1, \dots$) and requiring that the coefficients of ε^m all vanish individually for each m , we obtain a sequence of homotypic linear boundary value problems. Integration of these problems on the basis of the lower solutions $\theta_0, \theta_1, \dots, \theta_{m-1}$ yields the values of the corrections θ_m of ε^m in the expansion (8). Here, it is assumed that the perturbation $\varepsilon\Phi(\theta_s, q)$ is small in comparison with unity in the condition (7), which ensures satisfaction of the inequalities $\theta_0 \gg \theta_1 > \theta_2 > \dots$, i.e., the corrections to the basic solution (zero approximation) will amount to a small percentage of the sought temperature θ .

The functions

$$\Phi_m[\theta_n(\varepsilon), q] = \frac{1}{(m-1)!} \left(\frac{\partial^{m-1} \Phi}{\partial \varepsilon^{m-1}} \right) \Big|_{\varepsilon=0}^{\theta_n=\theta_{n0}} \quad (m = 1, 2, \dots) \quad (9)$$

appear as variable temperatures of the medium in the boundary value problems θ_m ($m = 1, 2, \dots$). The solutions of these problems can be obtained on the basis of the Duhamel theorem [2], which is valid for a body of any geometric form

$$\theta_m(P, Fo) = \frac{\partial}{\partial Fo} \int_0^{Fo} \Phi_m(Fo - \theta) \left(\frac{\theta_0(P, \theta) - \theta_1}{1 - \theta_1} \right) d\theta, \quad (10)$$

where $P = P(x, y, z)$ is a point of coordinate space; $Fo = a\tau/R^2$ is the Fourier number (a is the thermal diffusivity, τ is time).

The relative excess temperature, for example, for bodies of 51 classical form (plate, cylinder, sphere) with form factor Γ (equal to 1, 2, 3, respectively) may be written in the form [2]

$$\frac{\theta_0(X, Fo) - \theta_{\infty}}{1 - \theta_{\infty}} = 1 - \sum_{n=1}^{\infty} M_n(X) \exp(-\mu_n^2 Fo), \quad (11)$$

where

$$M_n(X) = \begin{cases} A_n \cos \mu_n X, & \mu_n \operatorname{tg} \mu_n = \operatorname{Bi}_x, & \Gamma = 1; \\ A_n I_0(\mu_n X), & \mu_n = \operatorname{Bi}_x \frac{I_0(\mu_n)}{I_1(\mu_n)}, & \Gamma = 2; \\ A_n \frac{\sin \mu_n X}{\mu_n X}, & \operatorname{tg} \mu_n = -\frac{\mu_n}{\operatorname{Bi}_x - 1}, & \Gamma = 3; \end{cases} \quad (12)$$

$X = x/R$ is the dimensionless coordinate.

In (12), the corresponding thermal amplitudes $A_n(\mu_n)$ also depend on Γ

$$A_n(\mu_n) = \begin{cases} \frac{2 \sin \mu_n}{\mu_n + \sin \mu_n \cos \mu_n}, & \Gamma = 1; \\ \frac{2 I_1(\mu_n)}{\mu_n [I_0^2(\mu_n) + I_1^2(\mu_n)]}, & \Gamma = 2; \\ \frac{2 (\sin \mu_n - \mu_n \cos \mu_n)}{\mu_n - \sin \mu_n \cos \mu_n}, & \Gamma = 3; \end{cases} \quad (13)$$

$I_0(z)$ and $I_1(z)$ are Bessel functions of the first kind of zero and first order, respectively.

For engineering applications, we are interested not so much in the theoretical convergence of the series (8) as in the error which is made when we retain a segment of the series (usually two or three terms) for $\epsilon = 1$. In order to evaluate the error of the proposed technique, we selected the usual technique of comparing the approximate solutions with those obtained on computers.

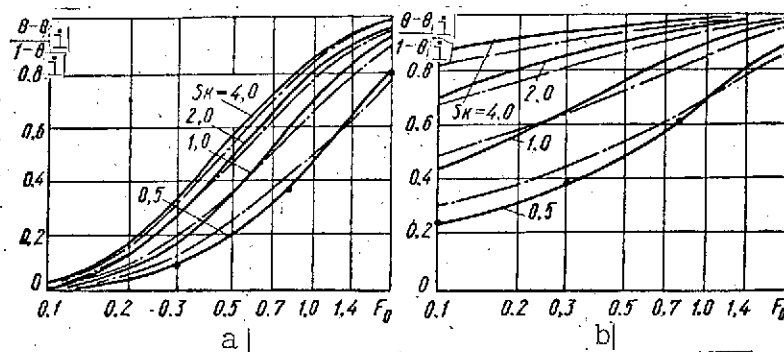


Figure 1. Dependence of relative excess temperature at the center (a) and surface (b) of plate on values of the criterion Fo ([the solid curves are the solution obtained on a digital computer [3]; the dash-dot curves are the solution of the "unperturbed" problem, "zero" approximation; the filled circles are the first approximation calculated using (18)].

We shall consider examples of heating of bodies of different form.

Example 1. Heating of an infinite flat plate by radiation in the variation range of the criterion Sk (0.5 — 4.0) with initial temperature $\theta_1 = 0.2$.

Figure 1 shows the results of calculation of the relative excess temperature for the center ($X = 0$) (a) and surface ($X = 1$) (b) of the plate using the proposed technique in comparison with the numerical solutions [3].

The solutions of the "unperturbed" problem ($\epsilon = 0$) differ from the tabulated values presented in [3] for the variation range $0.2 \leq Fo \leq 2.0$ by no more than 4 — 7%. For the center of the plate, this error decreases with increase of Sk . For $Sk > 4.0$ ($Bi_\Sigma > 10$), the temperature distribution becomes close to that in the problem with boundary condition of the first kind. The error of the first approximation

$$\theta(X, Fo) = \theta_0(X, Fo) + \theta_1(X, Fo) \quad (14)$$

is 1.0 — 1.5% for $Sk = 0.5$ and less than 1.0% for $Sk > 0.5$.

For convenience in calculating the first correction, the function $\Phi_1(Fo, q)$ is approximated by the relation

$$\Phi_1(Fo, q) = \Phi_M - (\Phi_M - \Phi_{\frac{1}{2}}) \exp(-bFo),$$

for which (10) takes the form

$$\theta_1(X, Fo) = \frac{1}{1+q} \left\{ \Phi_{\frac{1}{2}} \left[\frac{\theta_0(X, Fo) - \theta_{\frac{1}{2}}}{1 - \theta_{\frac{1}{2}}} \right] + (\Phi_M - \Phi_{\frac{1}{2}}) \left[1 - \exp(-bFo) - \sum_{n=1}^{\infty} \frac{\exp(-\mu_n^2 Fo) - \exp(-bFo)}{1 - \mu_n^2/b} M_n(\mu_n X) \right] \right\}, \quad (15)$$

where

$$\Phi_{\frac{1}{2}} = (1+q) \Phi(\theta_{\frac{1}{2}}, q); \quad \Phi_M = (1+q) \left[\frac{3}{4} \sqrt{\frac{1+q}{4}} (1+q) - q \right] = \\ = (1+q) \max_{0 \leq Fo \leq \infty} \Phi(\theta_0, q); \quad b = -\frac{1}{Fo'} \ln \left(\frac{\Phi_M}{\Phi_M - \Phi_{\frac{1}{2}}} \right). \quad (16)$$

Here, Fo' is the quantity for which $\Phi[\theta_0(Fo'), q] = 0$ ($\theta_0 \neq 1$).

For definite values of Sk (and correspondingly, b) and moments of time when

$$\exp[(\mu^2 - b)Fo] \sim \frac{\mu^2}{b} \ll 1,$$

Formula (15) simplifies and becomes more exact for large Fo

$$\theta_1(X, Fo) = \frac{1}{1+q} \left\{ \Phi_{\frac{1}{2}} \left[\frac{\theta_0(X, Fo) - 1}{1 - \theta_{\frac{1}{2}}} \right] + \Phi[\theta_0(Fo), q] \right\}. \quad (17)$$

Thus, in the considered example, $Sk \geq 1.0$ and $Fo \geq 0.3$, we can, with first approximation error on the order of 1%, use (17).

The analogous calculation made for an infinite cylinder with $Sk = 1.0$, $\theta_1 = 0.2$ showed that the difference between the temperatures $\theta_0(X, Fo)$ ($X \in [0, 1]$) and the values presented in [3] for $0.1 \leq Fo \leq 1.0$, amounts to no more than 4%, which indicates adequate engineering accuracy even in the zero approximation (solution of the linearized problem). The maximal error in calculation of the first approximation $\theta^{(1)}(X, Fo)$ does not exceed 1.5%. The error in the solution of the linear problem ($q = \varepsilon = 0$) for $X = 0$ and $X = 1$ reaches 18.7% and 21%, respectively.

The simple form of the solutions (11), (15), and (17) makes it possible to calculate the temperature distribution without a digital computer and determine the thermal stresses and displacements in solid bodies.

Let us examine the thermoelasticity problem for a sphere, taking as the basis the solution of the nonlinear thermal problem, which in the first approximation finally takes the form

$$\begin{aligned} \theta^{(1)}(X, Fo) = 1 - (1 - \theta_1) \sum_{n=1}^{\infty} M_n(X) \exp(-\mu_n^2 Fo) + \frac{1}{1+q} \left\{ \Phi_1 \left[1 - \sum_{n=1}^{\infty} M_n(X) \exp(\mu_n^2 Fo) \right] + (\Phi_m - \Phi_1) \left[1 - \exp(-b Fo) - \sum_{n=1}^{\infty} \frac{\exp(-\mu_n^2 Fo) - \exp(-b Fo)}{1 - \mu_n^2/b} M_n(X) \right] \right\}. \end{aligned} \quad (18)$$

Then the unsteady thermal stresses which arise in the sphere as a consequence of nonuniform heating and also the radial displacement [4] are defined by the formulas

$$\sigma_X = 4\mu\alpha T_c \frac{3\lambda + 2\mu}{\lambda + 2\mu} \left[I(1) - \frac{1}{X^3} I(X) \right], \quad 0 < X \leq 1; \quad (19)$$

$$\sigma_\theta = \sigma_\varphi = 2\mu\alpha T_c \frac{3\lambda + 2\mu}{\lambda + 2\mu} \left[\frac{1}{X^3} I(X) - 2I(1) - \theta^{(1)}(X, Fo) \right], \quad 0 < X; \quad (20)$$

$$u = \alpha T_c \frac{3\lambda + 2\mu}{\lambda + 2\mu} \left[\frac{1}{X^2} I(X) + \frac{2(1-2\nu)}{1+\nu} I(1) \right], \quad 0 < X \leq 1. \quad (21)$$

For $X = 0$, $u = 0$.

$$\sigma_\theta(0) = \sigma_X(0) = \sigma_\varphi(0) = 4\mu\alpha T_c \frac{3\lambda + 2\mu}{\lambda + 2\mu} \left[I(1) - \frac{2}{3} \theta^{(1)}(0, Fo) \right], \quad (22)$$

where

$$\begin{aligned} I(X) = & \frac{X^3}{3} - (1 - \theta_1) \sum_{n=1}^{\infty} \frac{A_n \exp(-\mu_n^2 Fo)}{\mu_n} H(X) + \\ & + \frac{1}{1+q} \Phi_1 \left[\frac{X^3}{3} - \sum_{n=1}^{\infty} \frac{A_n \exp(-\mu_n^2 Fo)}{\mu_n} H(X) + (\Phi_m - \Phi_1) \left[\frac{X^3}{3} (1 - \right. \right. \\ & \left. \left. - \exp(-b Fo)) - \sum_{n=1}^{\infty} \frac{\exp(-\mu_n^2 Fo) - \exp(-b Fo)}{1 - \mu_n^2/b} \frac{A_n}{\mu_n} H(X) \right] \right], \\ H(X) = & \frac{\sin \mu_n X - X \mu_n \cos \mu_n X}{\mu_n^2}, \quad I(1) = I(X) \Big|_{X=1}. \end{aligned} \quad (23)$$

Here α is the coefficient of linear thermal expansion, λ and μ are Lamé constants, the subscripts θ and φ refer to spherical coordinates, ν is the Poisson coefficient.

Example 2. Radiational heating of a sphere with $Sk = 2.0$, $\theta_1 = 0.2$, $\nu = 0.33$. The temperature distribution along the sphere radius X for the linear problem ($q = \varepsilon = 0$) and the first approximation is shown in Figure 2. For $Fo = 0.05$, the thermal disturbance reaches the center of the sphere, while for $Fo = 0.8$, the steady state regime is reached. The difference between the solutions of the linear thermal problem for $q = \varepsilon = 0$ and the nonlinear problem in the first approximation is more than 30%, this is due to the difference in the solutions of the thermal stress and deformation components (Figures 3 and 4).

The thermal stresses σ_X and σ_θ are presented with accuracy to the constant factor $2\mu\alpha T_c (3\lambda + 2\mu)/(\lambda + 2\mu)$ and the thermal displacements with accuracy to the factor $\alpha T_c (3\lambda + 2\mu)/(\lambda + 2\mu)$. The

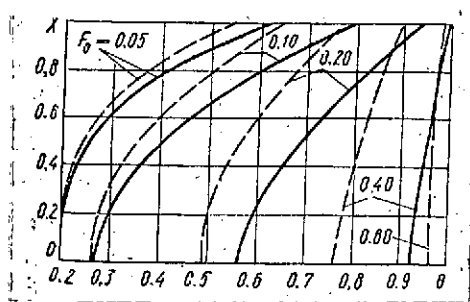


Figure 2. Distribution of relative temperature $\theta(X, Fo)$ along sphere radius X for different moments of time Fo for $Sk = 2$, $\theta_1 = 0.2$, $\nu = 0.33$ [solid curves are the solution using (18) with $q = 1.325$; dashed curves are the solution of the linear problem with $q = 0$, $\epsilon = 0$].

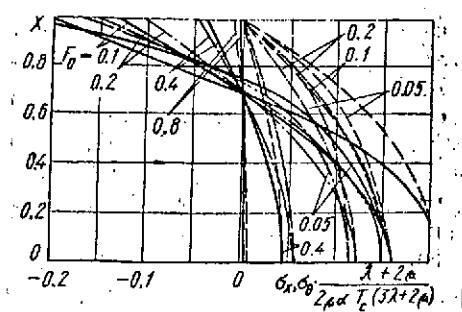


Figure 3. Distribution of thermal stresses σ_θ , σ_X along sphere radius at moments of time Fo (solid and dashed curves correspond to the values of σ_θ and σ_X in the nonlinear thermal problem; the dash-dot and dashed curves correspond to the linear problem with $q = \epsilon = 0$).

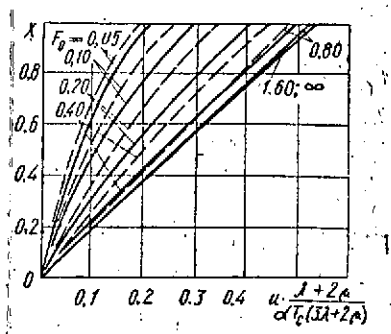


Figure 4. Radial displacements u for sphere at moments of time Fo (solid curves correspond to the solution of the nonlinear thermal problem; dashed curves correspond to the solution of the linear problem with $q = \epsilon = 0$).

values of the components σ_X differ most at the sphere center (25%); in the displacements u , this difference reaches the maximal magnitude at the sphere surface (20%).

Similarly, taking as the basis the corresponding solution of the thermal problem, we can solve the thermoelasticity problem for a spherical shell.

REFERENCES

1. Zamula, G. N., and V. M. Marchenko. In the book: Teplovye /54
napryazheniya v elementakh konstruktsiy (Thermal Stresses
in Structural Elements). Vol. 5, Kiev, Naukova Dumka
Press, 1965.
2. Lykov, A. V. Teoriya teploprovodnosti (Theory of Heat
Conduction). Moscow, Vysshaya Shkola Press, 1967.
3. Vidin, Yu. V., and V. V. Ivanov. Raschet temperaturnykh
poley v tverdykh telakh, nagrevayemykh konvektsiyei
i radiatsiyei odnovremenno (Calculation of Thermal Fields
in Solids Heated by Convection and Radiation Simultane-
ously). Press of Krasnoyarsk Polytechnic Institute, 1965.
4. Boley, B. A., and J. H. Weiner. Theory of Thermal Stresses.
Moscow, Mir Press, 1964.

EFFECTIVENESS OF SOLID LUBRICANT COATINGS FOR FRICTION
IN HARD VACUUM (10^{-9} tor)

B. I. Verkin, I. M. Lyubraskiy, V. F. Udovenko,
and L. N. Sentyurikhina

A study is made of the efficiency of solid lubricating coatings based on MoS_2 with various binders during friction under high-vacuum conditions with the use of mass spectrometric analysis of the composition of the gas evolved from the coatings in the friction process. It is shown that the vacuum level, loading, and sliding velocity influence coating effectiveness. In the friction process the solid lubricant coatings yield characteristic decay products associated with the chemical nature of the binders. The mechanism of coating breakdown during friction is associated with the binder breakdown mechanism.

The problem of improving the reliability and service life /54
of machines is intimately associated with questions of lubricating material application for friction components and also with questions concerning the theory of friction, lubrication, and wear, all of which are important. At the present time, this problem has been broadened in machine design and includes such questions as friction, lubrication, and wear in vacuum. This is a result of the fact that, in many mechanisms used in various branches of industry and for scientific purposes, friction takes place under vacuum conditions.

Since special conditions are created in vacuum, the question of friction and particularly the question of lubricating material application is examined from a new viewpoint. Study of lubricating material behavior under vacuum conditions may yield new results.

The primary influence of vacuum on friction pair behavior shows up in the fact that the surfaces of solid bodies in a vacuum are free of the adsorbed and chemisorbed films which normally cover these surfaces and the surfaces come into direct contact with one another and form intolerably strong bonds [1]. The forces of adhesion during contact of juvenile surfaces are tremendous; as a result, the friction coefficient increases sharply and in the end, the surfaces may even weld together in the cold state [2].

One of the effective means to protect friction surfaces against seizing and subsequent deep grooving is creation between the surfaces of special lubricant layers (ensuring satisfaction of the positive gradient rule [3]) which are easily deformed, can withstand repeated mechanical action, have a strong bond with the basic material, and retain their properties over the specified temperature range. At the present time, a new form of lubricant is finding increased application for these purposes — solid lubricants, which include lamellar solid substances having as a consequence of their crystalline structure low friction coefficient: graphite, MoS_2 , WS_2 , MoSe_2 , BN, mica, talc, etc. Graphite and MoS_2 are most frequently used as solid lubricants. They are used in the form of finely dispersed powders, pastes, briquettes, suspensions, and solid lubricating coatings [4, 5].

The widest use for solving problems associated with reducing friction and wear under hard vacuum conditions has been made of the solid lubricant coatings (hereafter called s.l. coatings), which are a combination of antifriction component (MoS_2 or graphite) and binder and are applied to the metallic surface in suspension form with subsequent solidification at elevated temperatures [5].

The effectiveness of s.l. coating application depends primarily on correct selection of the composition of the suspension, the technique for its application and subsequent solidification, the chemical nature of the suspension, and also on the metal and preliminary treatment of its surface. /55

The need for the study whose results are presented in the following arose primarily to solve the practical problems associated with the operation of various components and mechanisms under vacuum conditions.

At the Physico-Technical Institute of Low Temperatures of the AS UkSSR, together with VNII NP (All-Union Scientific Research Institute of Petroleum and Gas Processing and the Production of Synthetic Liquid Fuel), the technique was developed and a series of studies were carried out to investigate the effectiveness of s.l. coatings based on MoS_2 in the case of sliding friction under atmospheric conditions (with and without drying of the air) and in hard vacuum (10^{-9} tor) at room (25°C) and low (-196°C) temperatures with observation and monitoring of the composition of the gases which are evolved during the friction process.

The behavior of the s.l. coatings in hard vacuum and their effectiveness must be examined under conditions which are as close as possible to the actual operating conditions. The

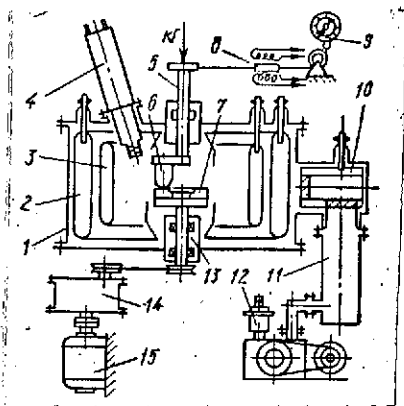


Figure 1. Schematic of UTI-1 facility of FTINT AS UkSSR.

1- vacuum chamber; 2- nitrogen shield; 3- cryogenic hydrogen pump; 4- MSKh-3A sensor (mass analyzer); 5- upper unit; 6- slider; 7- ring; 8- friction force recording sensor; 9- dynamometer; 10- nitrogen trap; 11- diffusion pump; 12- forevacuum pump; 13- lower unit; 14- speed reducer; 15- electric motor.

effectiveness of the same s.l. coatings will be different for friction in vacuum and in air. Therefore, it is very important to develop methods for studying s.l. coating effectiveness in hard vacuum and evaluating the results of the study; this was done for a series of s.l. coatings based on MoS_2 which were developed at VNII

NP and have been widely used in practice, in particular lubricants such as VNII NP-209, VNII NP-212, VNII NP-213, VNII NP-229, and VNII NP-230, which differ in chemical nature of the binder. The selected s.l. coatings are most promising, since they have excellent cohesive and adhesional

properties and very high resistance to erosion under atmospheric conditions.

Coatings of thickness 20 ± 5 micrometers were applied by spraying at a pressure of 2 atm on previously sand blasted surfaces of the hemispherical slider and the flat ring of the friction unit of the UTI-1 facility of FTINT AS UkSSR [6, 7] (Figure 1).

The basic vacuum condition characteristic is considered to be the magnitude of the total pressure measured in the test space. However, this characteristic is inadequate because of absence of information on gas composition in the test space. Moreover, a local vacuum is created near the working surfaces of the enclosed friction pair or when using a heater.

Mass spectrometric analysis of the gases prior to and during the experiment yields more complete characterization of the gaseous medium surrounding the friction pair. In order to obtain information on residual gas qualitative composition and study the gaseous products which are released during friction of the s.l. coatings, we used the mass spectrometric method [8, 9]. Inside the high vacuum chamber where the friction unit is located, we installed the sensor (mass analyzer) (Figure 1) of the MSKh-3A fast response time-of-flight mass spectrometer, a characteristic of which is that it records continuously the entire mass spectrum and thus makes it possible to follow the dynamic variation of the qualitative composition of the gaseous products which are released from the materials in the friction process. The selection of the MSKh-3A fast response time-of-flight dynamic type mass spectrometer was based on the fast transient processes which /56 take place during friction of s.l. coatings.

The test conditions were as follows: vacuum 10^{-9} tor, sliding velocity 0.87 m/sec, normal load 4.75 kG, radius of slider sphere 4.5 mm, initial Hertz contact pressure 176 kG/mm^2 . In those cases when we studied the influence of load or sliding velocity on s.l. coating effectiveness and antifriction properties, the load was varied in the interval 100 — 200 kG/mm^2 and the sliding velocity in the interval 0.1 — 3.5 m/sec.

As the criterion of s.l. coating effectiveness, we took the coating operating time (service life) until marked irreversible increase of the friction coefficient, which led to s.l. coating erosion and the appearance of metallic contact between the friction surfaces.

The studies conducted showed that, other conditions being the same, the service life and antifriction properties of the s.l. coatings are influenced by the external medium: atmospheric conditions (dry or moist air) [8], vacuum [7], vacuum level [8, 9], and also the conditions which always accompany friction: load, sliding velocity, and temperature [5, 10].

In the process of s.l. coating erosion, its physical and chemical properties change. These changes may occur both in the antifriction component MoS_2 and in the binder. The primary factor which influences the antifriction properties of s.l. coatings, along with temperature on which the rate of thermal decomposition of the components depends [5], is the presence of atmospheric moisture and oxygen.

Under atmospheric conditions with constant oxygen content, the humidity of the air has a significant influence on the antifriction properties of the s.l. coatings as well as on the powder coatings MoS_2 [4]. Depending on the humidity level, the friction coefficient may increase or decrease by two to three times. Removal of the moisture vapors leads to improvement of s.l. coating antifriction properties. High atmospheric humidity influences not only on the s.l. coating antifriction properties but also their service life [8].

In deep vacuum, where the amount of moisture and other residual gases including oxygen is low, s.l. coating service life will be high. However, studies have shown that the s.l. coatings with organic binders are the longest lived, just as in air: the urea-formaldehyde (VNII NP-212) and epoxy (VNII NP-230) resins and the inorganic sodium silicate binder (VNII NP-229). The s.l. coatings with silicone binder (VNII NP-209, VNII NP-213) have shorter service life in deep vacuum.

The entire s.l. coating operating period within the limits of the time studied can be divided into two stages — the continuous friction period (friction coefficient nearly constant), and the discontinuous friction period (magnitude of the friction coefficient changes abruptly). For VNII NP-212, VNII NP-229, VNII NP-230, the continuous friction period lasted for six to eight hours. The pressure in the chamber remained nearly constant (varied in the range 10^{-8} — $2 \cdot 10^{-8}$ tor). For the VNII NP-209 and VNII NP-213 coatings, the continuous friction period lasted 15 to 30 minutes and the pressure in the chamber increased from $5 \cdot 10^{-9}$ to 10^{-7} torr. The average value of the friction coefficient in the first period for VNII NP-212, VNII NP-229, and VNII NP-230 was 0.02 — 0.04; while for VNII NP-209 and VNII NP-213, the average value was 0.04 — 0.06, i.e., the friction coefficient of the coatings with organic and inorganic binders is lower by a factor of two than for the silicone binder, and on the whole, the coatings which we studied are characterized by a low friction coefficient, not exceeding 0.08. Under atmospheric conditions, the friction coefficient of these same s.l. coatings is higher and amounts to 0.12.

In studying the influence of vacuum level (degree of rarefaction) on s.l. coating effectiveness, it was found that the friction characteristics (friction coefficient and service life) /57 begin to change noticeably as soon as the pressure of the gaseous medium surrounding the friction pair becomes lower than atmospheric. Thus, with reduction pressure from 100 tor, the s.l. coating friction coefficient decreases and service life increases. In the pressure interval 100 — 10^{-1} tor, these characteristics change only slightly. However, with pressure reduction in the interval 10^{-1} — 10^{-3} tor, we again see marked reduction of coating friction coefficient and service life. Outside this interval throughout the entire pressure range studied 10^{-4} — 10^{-9} tor, the s.l. coating friction characteristics remain

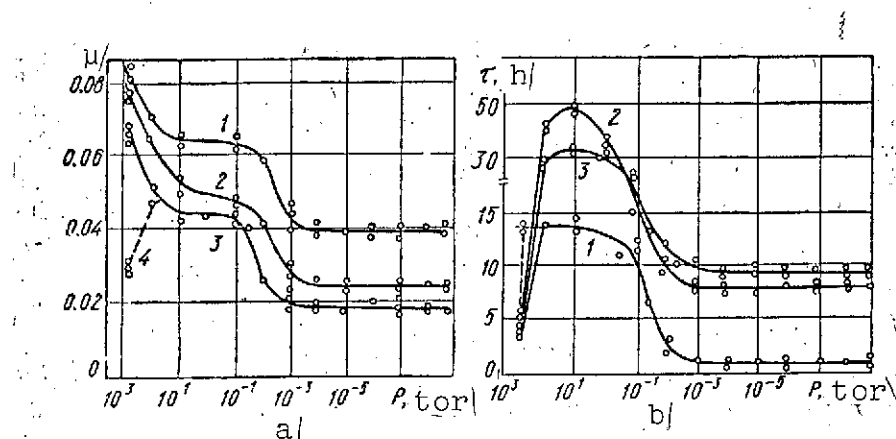


Figure 2. Dependence of friction coefficient (a) and service life (b) of s.l. coatings VNII NP-213 (curve 1), VNII NP-212 (curve 2), VNII NP-229 (curve 3), on vacuum depth and air humidity (curve 4).

practically constant or vary only slightly (Figure 2).

We can assume that this complex nature of the friction coefficient $\mu = \varphi(P)$ and service life $\tau = \varphi(P)$ variation is due to the influence of the medium surrounding the friction pair and also to the resistance of the s.l. coatings to tribocracking (coating destruction during friction) [8, 9, 10].

Thus, the vacuum intensity has a significant influence on s.l. coating antifriction properties and service life. Both the mechanism and final result of this interaction depend to a great degree on the physical and chemical properties of the components which make up the s.l. coatings.

The influence of load and sliding velocity on the friction coefficient variation of the VNII NP-213, VNII NP-212, and VNII NP-229 s.l. coatings shows up similarly for all three binder cases — silicone, organic, and inorganic. With increase of the load, we observe a general pattern of friction coefficient decrease regardless of the test conditions (atmospheric or deep

vacuum) [10]. This same pattern is observed with variation of the sliding velocity.

In studying the effect of load on s.l. coating service life, we find that this effect has a dual nature: on the one hand, load increase leads to increase of the temperature which occurs during friction and this accelerates and facilitates binder transition from one phase state to another and leads to friction coefficient decrease and service life increase; on the other hand, the heat which arises in the friction process is not removed by the s.l. coating but is accumulated, which leads to binder decomposition and failure of the s.l. coating — tribo-cracking. The interaction of these factors may be used to explain the peak on the $\tau = \varphi(N)$ curve. This pattern of service life variation with load increase is observed in both dry and moist air and in deep vacuum. A service life maximum for some definite loading is characteristic for each s.l. coating. The dependence of the friction coefficient $\mu = \varphi(v)$ and service life (friction path distance) $s = \varphi(v)$ on the sliding velocity of the VNII NP-213, VNII NP-212, and VNII NP-229 s.l. coatings, and the relation $\tau = \varphi(N)$ as well, have an extremal nature. This nature of the VNII NP-213, VNII NP-212, and VNII NP-229 s.l. coating friction coefficient and service life variation is observed in dry and moist air and in deep vacuum, and is associated with the frictional heating upon increase of the sliding velocity, leading to change of the binder phase state, which changes similarly to the variation of the relation $\tau = \varphi(N)$. |

The chemical nature of the binder has considerable influence on the behavior of the $\mu = \varphi(v)$ and $s = \varphi(v)$ curves. Each s.l. coating has on the curves its own optimum, corresponding to a definite sliding velocity.

Analysis of the relations $\mu = \varphi(N)$, $\tau = \varphi(N)$, $|\mu = \varphi(v)|$ and $s = \varphi(v)$ showed that, with increase of the load and sliding velocity, the latter has considerable influence on VNII NP-213, VNII NP-212, and VNII NP-229 s.l. coating friction coefficient and service life variation.

We were interested in determining whether or not the s.l. coatings will be retained on the friction components and whether or not they will be effective at low (cryogenic) temperatures. For this purpose, we studied the service life and antifriction properties of the s.l. coatings VNII NP-212 with organic binder and VNII NP-213 with silicone binder at low temperatures (-196°C) in deep vacuum. Comparing the results of experiments made in deep vacuum at room ($+25^{\circ}\text{C}$) and cryogenic (-196°C) temperatures, we can see that the service life of the s.l. coatings with organic binder — urea-formaldehyde resin K-411-02 — remains at the same level, while for the coating with silicone polymer KO-921, at cryogenic temperature, the lifetime decreases, which is associated with brittle failure of the silicone polymer. The friction coefficient of the VNII NP-212 and VNII NP-213 s.l. coatings increases only slightly when tested under cryogenic temperature conditions.

Identification of the factors which lead to pressure change in the vacuum chamber during friction of the s.l. coatings, and also qualitative analysis of the gaseous products released from the coatings in the friction process, make it possible to explain to some degree those changes which are observed in the coatings during friction, clarify the mechanism of their fracture, and evaluate the influence of various factors on s.l. coating service life and antifriction properties.

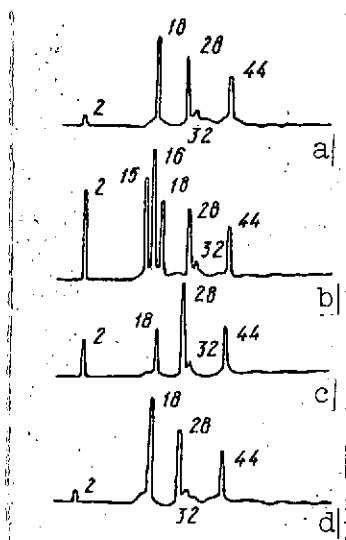


Figure 3. Mass spectrograms obtained in s.l. coating friction.

a- chamber background; b- VNII NP-213 coating; c- VNII NP-212 coating; d- VNII NP-229 coating.

Study of the breakdown kinetics of the s.l. coatings and their components is important for understanding the process taking place in s.l. coating friction. Therefore, it is very desirable to utilize mass spectrometry, which permits obtaining new information on the behavior of the solid lubricant coatings directly in the friction process.

Mass spectrometric study of the products released from the s.l. coatings in the friction process showed that, in comparison with the chamber background (Figure 3a), each coating type yields charac-

teristic decay products which depend on the chemical nature of the binder. Thus, during friction of the VNII NP-213 s.l. coating, we observe on the mass spectrograms increase of the peaks corresponding to masses 2; 15; 16 (Figure 3b). Here the variations of the mass peak growth rate, residual pressure in the vacuum chamber, and friction coefficient are related synchronously with one another. Comparing the growth rate kinetics of the peaks corresponding to masses 2; 15; 16 for s.l. coatings VNII NP-209 and VNII NP-213 of the same binder class (KO-921 silicone resin), which differ from one another in binder quantity (the factor K , indicating the ratio of the amount of binder to the amount of MoS_2 , is unity for the VNII NP-209 coating, for the VNII NP-213 coating $K = 0.5$), we can note that the peak growth rate for the VNII NP-209 coating is considerably higher (for the same coating operating time) than for the VNII NP-213

coating. Here we also note that the VNII NP-209 coating service life in deep vacuum is less than that of the VNII NP-213 coating.

The friction process of the VNII NP-212 coating with organic binder (K-411-02 urea-formaldehyde resin) was accompanied by only slight pressure increase in the vacuum chamber from 10^{-8} to $6 \cdot 10^{-8}$ tor and on the mass spectrograms, we observed only slight increase of the peaks corresponding to masses 2 and 28, while the peak corresponding to mass 18 decreased (Figure 3c).

During friction of the VNII NP-229 s.l. coating with inorganic binder (sodium silicate Na_2SiO_3), we observed only slight increase of the peak corresponding to mass 18 (Figure 3d). Here the pressure in the vacuum chamber changed only slightly for both the VNII NP-212 and VNII NP-229 coatings.

The analysis made of the mass spectrograms showed that the observed pressure changes in the vacuum chamber are the consequence of s.l. coating decay product gas evolution caused by tribochemical changes taking place in the coatings during friction. These changes can take place both in the MoS_2 antifriction filler in the binder.

For complete clarification of the factors leading to evolution of gaseous products during the s.l. coating friction process, we made a mass spectrometric analysis during friction of the MoS_2 antifriction filler and the binders separately. During the friction process of MoS_2 in powder form, we did not observe any changes in the mass spectrogram in comparison with the chamber background (the friction process realization conditions corresponded to the s.l. coating friction conditions).

The data obtained on binder breakdown kinetics indicate that the organic binders are more resistant to tribocracking than the silicone binders, which leads to greater effectiveness under deep vacuum conditions of the VNII NP-212 and VNII NP-230 s.l. coatings, since s.l. coating failure is associated with binder failure kinetics in the friction process. In addition, the possible organic binder decay products may play the role of a lubricant, in contrast with the silicone binder.

As has been noted previously [9, 10], the tribocracking processes in the s.l. coatings which contain silicone polymers show up to a greater degree in deep vacuum than in air, since under deep vacuum conditions because of oxygen deficiency, the siloxane bonds which inhibit further breakdown of the polymer do not form. Therefore, the service life of the VNII NP-209 and VNII NP-213 s.l. coatings is shorter in deep vacuum than in air. This is confirmed by the mass spectrograms obtained during VNII NP-213 s.l. coating friction at low temperature (-196°C), on which we find peaks corresponding to masses 2; 15; 16. The intensity of these peaks is higher and the service life is shorter in comparison with the intensity and service life at room temperature. All this indicates that the polysiloxanes used as binders in the s.l. coatings, just as the silicone fluids [11, 12], are less stable in the friction process than the coatings with organic and inorganic binders.

Thus, in vacuum at normal and low temperatures, the s.l. coatings with organic binders are preferable, just as in air.

/60

REFERENCES

1. Jaffe, L. D., and J. B. Rittenhouse. ARS Journal, Vol. 3, 1962.

2. Verkin, B. I., Ye. L. Kravchenko, and A. N. Lyulichev. In the book: O prirode skhvatyvaniya tverdykh tel (On the Nature of Solid Body Seizing). Moscow, Nauka Press, 1968.
3. Kragel'skiy, I. V. Treniye i iznos (Friction and Wear). Moscow, Mashinostroyeniye Press, 1968.
4. Braithwaite, E. R. Solid Lubricants and Antifriction Surfaces. Moscow, Khimiya Press, 1967.
5. Sentyurikhina, L. N., and Ye. M. Oparina. Tverdye disul'fidmolibdenovye smazki (Solid Molybdenum Disulfide Lubricants). Moscow, Khimiya Press, 1966.
6. Udovenko, V. F. FKhMM, Vol. 4, No. 2, 1968.
7. Lyubarskiy, I. M., et al. Khimiya i tekhnologiya topliv i masel (Chemistry and Technology of Fuels and Oils). Vol. 5, 1969.
8. Sentyurikhina, L. N., et al. FKhMM, Vol. 6, No. 4, 1970.
9. Kurilov, G. V., et al. Mekhanika polimerov, Vol. 6, 1970.
10. Kurilov, G. V., et al. Khimiya i tekhnologiya topliv i masel, Vol. 3, 1970.
11. Vinogradov, G. V., N. S. Nametkin, and M. I. Nosov. In the book: Novoye o smazochnykh materialakh (New Lubricants). Moscow, Khimiya Press, 1967.
12. Klimov, K. I., and V. A. Mikheyev. In the book: Plastiknyye smazki i tverdye smazochnye pokrytiya (Plastic Lubricants and Solid Lubricating Coatings). Khimiya Press, 1969.

TRANSIENT COOLING OF SOLID BODIES OF CLASSICAL FORM BY RADIATION

V. S. Novikov and V. L. Chumakov

An approximate analytic method is presented for analysis of the unsteady process of radiative cooling of solid bodies of classical form. The nonlinear heat transfer problem is solved by the cascade linearization technique with use of the iteration method. Comparison of the results obtained even in the first approximation with the available numerical solutions indicates adequate engineering accuracy of the proposed technique.

The question of heat transfer by radiation has become increasingly important in recent years in connection with intensive space studies. This question is intimately associated with the problem of space vehicle and satellite interaction with the ambient medium and heat removal from their powerplants. /60

The subject of the present paper is analysis of heat transfer during cooling of solid bodies by radiation and obtaining computational equations which are sufficiently exact and convenient for engineering determination of the transient temperature fields.

The subject problem is a nonlinear problem of mathematical physics with significant nonlinearity in the boundary condition. Exact analytic solutions of such problems have not yet been obtained, therefore, the analysis of body cooling by radiation is made using various approximate (basically numerical [1 — 3]) methods.

Among the approximate methods, the linearization techniques [4 — 9] are worthy of particular attention, being simple and quite exact. They are based on linearizing the heat transfer law, which for $T_s \gg T_c$ has the form

$$\lambda(\text{grad } T)_s = -\sigma_a T_s^4, \quad (1)$$

where T_s is the body surface temperature; σ_a is the apparent radioactivity; λ is the thermal conductivity.

The linearization methods can be divided into two groups. In the first group, the condition (1) is linearized without considering the heat conduction equation [7 — 9]. This method involves expanding the right side of the condition (1) into a Taylor series about some fixed temperature T_* and retaining the first two terms, which yields satisfactory results for small temperature differences $T_s - T$. The second group includes the integral linearizing transformation methods. These methods also /61 linearize the condition (1), but in this case, there arises a nonlinear complex in the heat conduction equation which can be discarded for bodies which are not too massive thermally. Specific examples of such transformations can be found in [4, 5]. In [6], the linearizing transformation method was refined by introducing a correcting parameter whose proper selection leads to smaller errors when discarding the nonlinear complex.

The cascade linearization method proposed here can be applied to any problem of radiant cooling of bodies of both small and large "thermal inertia," with minimal errors in determining the temperature fields in comparison with the known linearization methods.

In the problem investigated, we make the following assumptions:

1. The axisymmetric body (plate, cylinder, sphere) is made of uniform isotropic and opaque material whose thermal and physical properties are independent of temperature.

2. Radiation is the only form of heat transfer between the body and the surrounding medium. From the instant of time $Fo = 0$, the body surface begins to radiate into the ambient medium, whose temperature in a particular case may be absolute zero.

3. The thermal fluxes are directed along the normal to the surface (along the radius for the sphere and cylinder). End effects are not considered.

4. The body radiativity is independent of its surface temperature.

5. The initial body temperature T_1 and temperature T_c of the medium are constant ($T_c < T_1$).

The mathematical model of the problem in dimensionless form is constructed on the basis of the Fourier equation

$$\frac{\partial \theta(X, Fo)}{\partial Fo} = X^{-\nu} \frac{\partial}{\partial X} \left[X^{\nu} \frac{\partial \theta(X, Fo)}{\partial X} \right], \quad 0 < X < 1, \quad Fo > 0 \quad (2)$$

with the initial

$$\theta(X, 0) = 1 \quad (3)$$

and boundary conditions

$$\frac{\partial \theta(0, Fo)}{\partial X} = 0; \quad (4)$$

$$\frac{\partial \theta(1, Fo)}{\partial X} = Sk [\theta_c^4 - \theta^4(1, Fo)], \quad (5)$$

where $Fo = a\tau/R^2$, $Sk = \sigma_a T_1^3 R/\lambda$, v is the form factor ($v = 0$ for a plate, $v = 1$ for a cylinder, $v = 2$ for a sphere). We approximate $\theta^4(1, Fo)$ by a parabola $(A + B\theta^2)$ in the temperature range $\theta_* \leq \theta \leq 1$ on the basis of satisfaction of the following conditions:

$$\int_{\theta_*}^1 \theta^4 d\theta = \int_{\theta_*}^1 (A + B\theta^2) d\theta \quad (6)$$

and

$$\theta^4|_{\theta=\theta_*} = (A + B\theta^2)|_{\theta=\theta_*}. \quad (7)$$

We find the constants A and B from solution of the system of Equations (6) and (7)

$$B = \frac{3}{5} \frac{4\theta_*^5 + 1 - 5\theta_*^4}{1 + 2\theta_*^3 - 3\theta_*^2}; \quad A = \theta_*^4 - B\theta_*^2. \quad (8)$$

We rewrite the condition (5) in the form

$$\frac{\partial \theta(1, Fo)}{\partial X} = -Sk [\bar{A} + B\theta^2(1, Fo)] - \Phi[\theta(1, Fo)], \quad (9)$$

where

$$\bar{A} = A - \theta_*^4, \quad (10)$$

$$\Phi = Sk [\theta^4(1, Fo) - (A + B\theta^2(1, Fo))]. \quad (11)$$

In the beginning of the process, the nonlinear complex $\Phi[\theta(1, F_0)]$ /62 appears as a surface heat sink; after some instant of time (when $\Phi < 0$), it has the physical sense of a surface heat source.

We then convert to the new variable v so that the boundary condition (9) with discarded complex Φ will be linear. From solution of the differential equation

$$d\theta/d\theta = -h\theta/(\bar{A} + B\theta^2) \quad (12)$$

we find that the variable v is defined by the expression

$$\theta = \left| \frac{\theta(B + \sqrt{-AB}) + \bar{A} - \sqrt{-AB}}{\theta(B - \sqrt{-AB}) + \bar{A} - \sqrt{+AB}} \right|^{-1/\eta}, \quad \eta = 2\sqrt{-AB}/h. \quad (13)$$

With account for the transformation (13), the equations (2), (3), (4), and (9) (for $\Phi = 0$) take the form

$$\frac{\partial\theta(X, F_0)}{\partial F_0} = X^{-v} \frac{\partial}{\partial X} \left[X^v \frac{\partial\theta(X, F_0)}{\partial X} \right] + \varphi; \quad (14)$$

$$\varphi = \frac{\partial^2\theta}{\partial\theta^2} \left(\frac{\partial\theta}{\partial X} \right)^2 = -h\theta(h + 2B\theta) \left(\frac{\partial\theta/\partial R}{\bar{A} + B\theta^2} \right)^2; \quad (15)$$

$$\frac{\partial\theta(0, F_0)}{\partial X} = 0, \quad \theta(X, 0) = 1, \quad (16)$$

$$\frac{\partial\theta(1, F_0)}{\partial X} = hSk\theta, \quad h < 0, \quad (17)$$

$$h = -2B\theta|_{\theta=\bar{\theta}=0.5(1+\theta_*)} = -B(1+\theta_*). \quad (18)$$

The influence of the complex φ is opposite that of the nonlinear function Φ — in the beginning, φ plays the role of an internal heat source and later a heat sink. Consequently, the

errors from neglect of the complexes Φ and φ will also have opposite signs and will partially compensate one another, which on the whole makes the proposed linearization method more exact in comparison with the known methods [4 — 9].

The solution of the boundary value problem (14), (16) — (18) for $\varphi = 0$ on the basis of [10] is written in the form

$$\theta(X, Fo) = \sum_{n=1}^{\infty} M_n(X) \exp(-\mu_n^2 Fo), \quad (19)$$

where the expressions for $M_n X$ depend on the geometry of the body

$$M_n(X) = \begin{cases} A_n \cos \mu_n X, & v = 0; \\ A_n I_0(\mu_n X), & v = 1; \\ A_n \frac{\sin \mu_n X}{\mu_n X}, & v = 2, \end{cases} \quad (20)$$

where $I_0(z)$ is the Bessel function of the first kind of zero order.

The coefficients $A_n(-hSk)$ and $\mu_n(-hSk)$ are tabulated in [10]. The sought temperature $\theta(X, Fo)$ is described in explicit form by the expression

$$\theta(X, Fo) = \frac{V - \bar{A}B - \bar{A} + (\bar{A} + V - \bar{A}B)\theta^{-\eta}(X, Fo)}{V - \bar{A}B + B - (B - V - \bar{A}B)\theta^{-\eta}(X, Fo)}. \quad (21)$$

The solution (19 — 21) describes approximately the cooling process of bodies both for $T_c = 0$ (in vacuum) and for $T_c \neq 0$.

The numerical temperature field calculations made using (19) — (21) and the method of [6] indicate better accuracy of the proposed technique. While for thermally thin bodies, the difference between the maximal errors of the two methods is comparatively small, with increase of the magnitude of the radiation criterion Sk , the discontinuity in the errors increases

significantly. For example, for $Sk = 2.0$ and $X = 0$ in the range $0 \leq Fo \leq 2.0$ for $\theta_* = 0.55$, the corresponding maximal errors are 1.6 and 8.3%.

If necessary, the approximate temperature value found from (19) — (21) can be refined if we take this solution as the first approximation in an iteration scheme. /63

The general expression for the j^{th} iteration for the sought temperature at an arbitrary fixed instant of time Fo^* takes the form

$$\theta_j(X, Fo^*) = \frac{\sqrt{-\bar{A}_j B_j} - \bar{A}_j + (\bar{A}_j + \sqrt{-\bar{A}_j B_j}) \Phi^{-\eta_j}}{\sqrt{-\bar{A}_j B_j} - B_j - (B_j - \sqrt{-\bar{A}_j B_j}) \Phi^{-\eta_j}}, \quad (22)$$

where $A_{nj} = A_n(-h_j Sk)$, $\mu_{nj} = \mu_n(-h_j Sk)$, $h_j < 0$, and the linearization parameters

$$h_j = -B_j(1 + \theta_{*j-1}); \quad (23)$$

$$B_j = \frac{3}{5} \frac{4\theta_{*j-1}^5 + 1 - 5\theta_{*j-1}^4}{1 + 2\theta_{*j-1}^3 - 3\theta_{*j-1}^2}; \quad (24)$$

$$A_j = -B_j \theta_{*j-1}^2 + \theta_{*j-1}^4. \quad (25)$$

In this case, $\theta_{*0} = \theta_*$, i.e., the reference temperature θ_* will be the lowest of all the temperature values in the considered time interval. On the basis of the approximate analytic solutions (19) — (21), we can approximate easily and quite closely the transient temperature distribution in axisymmetric bodies cooled by radiation, which can be used in calculating thermal stresses in space structures being designed. Moreover, using the proposed technique and knowing the body surface and ambient

temperatures, we can find the transient thermal flux at the body surface, which is important for questions of spacecraft thermal protection.

The technique described in the article can be extended to the case of cooling of composite bodies with asymmetric non-linear boundary conditions describing combined convective and radiative heat exchange.

REFERENCES

1. Zerkle, R. D., and J. E. Sunderland. ASME, J. of Heat Transfer, Vol. 87, Ser. C, No. 1, 1965.
2. Crosbie, A. L., and R. Viskanta. In the book: Proc. Third International Conference, AIChE, Vol. 5, August 1966, pp. 146-153.
3. Ayres, D. L. ASME, J. of Heat Transfer, Vol. 92, Ser. C, No. 1, 1970.
4. Ivanov, V. V., and Yu. V. Vidin. Izv. vuzov, chernaya metallurgiya, Vol. 3, 1965.
5. Vidin, Yu. V. In the book: Issledovaniya po teploprovodnosti (Studies on Thermal Conduction). Minsk, Nauka and Tekhnika Presses, 1967.
6. Ivanov, V. V., and G. G. Medvedev. Inzhenerno-fizicheskiy zhurnal, Vol. 18, No. 3, 1970.
7. Chen, John C. Int. J. Heat and Mass Trans., Vol. 9, No. 5, 1966, pp. 443-450.
8. Benitsio, I., V. Dussen, and T. Irvine. In the book: Advances in Heat Transfer. Moscow, Mir Press, 1970.
9. Lunardini, V. I., and I. P. Chang. Int. J. Heat and Mass Trans., Vol. 13, No. 7, 1970, pp. 1240-1243.
10. Lykov, A. V. Teoriya teploprovodnosti (Theory of Heat Conduction). Moscow, Vysshaya Shkola Press, 1967.

THERMOCAPILLARY CONVECTION IN WEIGHTLESS CONDITIONS

V. G. Babskiy, I. L. Sklovskaya, and Yu. B. Sklovskiy

Results are presented of studies on thermocapillary instability of a liquid in a spherical layer with free surface and convection in a rectangular channel with horizontal temperature gradient. It is shown that in vessels partly filled with a viscous incompressible fluid and under essentially weightless conditions free convection may arise due to the surface tension temperature dependence.

Natural thermal convection under terrestrial conditions is /63 usually caused by Archimedes forces acting in a nonuniformly heated fluid. Under weightless or nearly weightless conditions, the role of the convection "engine" may be played by forces of different origin, associated with temperature gradients in the fluid. These are primarily the thermocapillary forces at the /64 "liquid gas" or "liquid-liquid" interface, which always arise when the interface is nonisothermal. They are proportional to the surface tension gradient at this surface.

The thermocapillary effects, which cause numerous and varied phenomena near the interface, have long attracted the attention of scientists. However, only in recent times has the attempt to make more profound study of the processes of chemical technology, boiling, mass transfer, and liquid behavior in weak force fields led to a rigorous theoretical formulation of the thermocapillary convection problem and obtaining its first quantitative characteristics.

Nearly all the known studies on thermocapillary convection are cited in [1, 2]. We shall examine in greater detail some results obtained in the division of applied mathematics of FTINT AS UkSSR.

In a nonuniformly heated liquid with free surface under weightless conditions, one of the following situations may arise:

1. In the liquid there is established a temperature distribution for which the free surface is isothermal and the liquid is in equilibrium. This equilibrium state may be stable or unstable, depending on the direction and magnitude of the temperature gradient in the liquid.

2. In the liquid there is established stationary free convection. Although the free surface form remains unchanged, in this case, its determination goes beyond the scope of hydrostatics and is a problem of hydrodynamics.

3. Complex unsteady motion of the liquid (and of its free surface) arises, in the best case periodic motion.

The equilibrium state of a nonisothermal liquid with free surface is obviously realized very rarely. Nevertheless, study of the equilibrium state stability boundary yields much valuable information on the form of the flows which develop, on the temperature gradient critical values, etc.

We shall examine a spherical vessel of radius R under weightless conditions, on the inner wall of which a viscous incompressible liquid forms a spherical layer of thickness $H = R - R_c$ (R_c is the radius of the "cavity"). In the liquid, there is the radial temperature gradient ΔT_0 , and $T_0(r)$ satisfies

the heat conduction equation and boundary conditions

$$\Delta T_0 = 0, \quad T_0(R) = C_1, \quad \left. \frac{\partial T_0}{\partial n} + \alpha T_0 \right|_{r=R_0} = C_2 \quad (1)$$

where n is the unit outward normal vector, and α is the constant coefficient of heat transfer at the "liquid-gas" interface.

The liquid velocity \bar{v} , pressure p , and temperature T in the case of stationary free convection in a vessel Ω with solid wall Σ and free surface S satisfy the equations in the region Ω

$$\left. \begin{aligned} v\Delta\bar{v} &= (\bar{v}\nabla)\bar{v} + \frac{1}{\rho}\nabla p; \quad \nabla\bar{v} = 0, \\ X\Delta T &= \bar{v}\nabla T \end{aligned} \right\} \quad (2)$$

and the boundary conditions [3]

$$\left. \begin{aligned} \bar{v}|_{\Sigma} &= 0, \quad T|_{\Sigma} = C_1, \quad \left(\frac{\partial T}{\partial n} + \alpha T \right)|_S = C_2; \\ (p - P_0)n_i &= \mu(v_{i,k} + v_{k,i})n^k - \sigma(k_1 + k_2)n_i - \frac{\partial\sigma}{\partial x_k}; \\ \bar{v}n &= 0 \text{ (on } S). \end{aligned} \right\} \quad (3)$$

Here P_0 is the constant external pressure, $\mu = \rho v$ (ρ is the density, v the viscosity of the liquid), σ is the surface tension coefficient, k_1 and k_2 are the principal curvatures of the surface S . /65

In the considered spherical layer case, the system (2), (3) admits the solution

$$\left. \begin{aligned} \bar{v}_0 &= 0, \quad T_0 = T_0(r), \quad P_0 = \text{const.} \end{aligned} \right\} \quad (4)$$

Let us find the stability boundary, i.e., the values of the physical and geometric parameters for which the equilibrium state (4) changes into movement of the liquid. We assume that

"stability variation principle" [4] is satisfied, which is equivalent to the assumption of stationary convection onset. Then the linearized dimensionless equations and boundary conditions for the disturbances take the form [5].

$$\left. \begin{aligned} \Delta \bar{u} &= \nabla p; \quad \nabla \bar{u} = 0, \quad \Delta \theta = f(r) r u_r; \\ \bar{u}|_{r=h} &= 0; \quad \theta|_{r=h} = 0; \\ \sigma_{r\theta} &= M \frac{1}{r} \frac{\partial}{\partial \theta} (\theta + N); \quad \sigma_{r\varphi} = M \frac{1}{r \sin \theta} \frac{\partial}{\partial \varphi} (\theta + N); \\ \sigma_{rr} &= -We Pr (2N + \Delta_S N); \quad u_r = 0, \quad \frac{\partial \theta}{\partial r} - Bi (\theta + N) = 0 \text{ (for } r = h) \end{aligned} \right\} \quad (5)$$

Here \bar{u} , p , θ are the velocity, pressure, and temperature perturbations; N is the free surface deviation

$$f(r) = -\frac{1}{r} \frac{dT_0}{dr} \gamma^{-1}, \quad \gamma = \left| \frac{dT_0}{dr} \right|_{r=1}; \quad (6)$$

M is the Marangoni number,

$$M = \frac{\gamma \left(-\frac{\partial \sigma}{\partial T} \right) R_c'}{\chi \mu};$$

Pr is the Prandtl number; We is the Weber number, $We = \frac{\sigma R_c}{\rho v^2}$;

Bi is the Bio number $Bi = \alpha R_c$.

The system of equations (5) is an eigenvalue problem in the parameter M and its solution can be obtained in explicit form. For this we seek solutions of the problem (5) in the form of series in generalized spherical functions (for more detail see [5]). Then the general solutions of the ordinary differential equations which appear upon separating variables are substituted into the boundary conditions and the condition of solvability of the resulting algebraic system of equations for the arbitrary constants reduces to the form

$$\mu_l = \frac{J^{-1}(h) [\zeta_1(h) + \text{Bi} \zeta_2(1, h)]}{1 + \frac{1}{(l+2)(l-1)q_l} J^{-1}(h) L\psi_{\zeta_1}(h)} \quad (l = 2, 3, \dots). \quad (7)$$

Here

$$\mu_l = Ml(l+1); \quad q_l = \text{WePr} l(l+1); \quad (8)$$

$$\left. \begin{aligned} \zeta_1(h) &= h^{2l+1}(l+1) + l; \quad \zeta_2(s, h) = s^{-l-1}(h^{2l+1} - s^{2l+1}); \\ J(h) &= \int_1^h \zeta_2(s, h) f(s) \psi(s) s^2 ds; \\ L\psi &= 3l(l+1)\psi'(1) - 3\psi''(1) - \psi'''(1). \end{aligned} \right\} \quad (9)$$

where

/66

$$\psi(r) = \frac{1}{\Delta(h)} (\Delta_1(h) r^{l+2} + \Delta_2(h) r^l + \Delta_3(h) r^{-l+1} + \Delta_4(h) r^{-l-1}); \quad (10)$$

$$\Delta(h) = \begin{vmatrix} 1 & 1 & 1 & 1 \\ (l+2)h^{l+1} & lh^{l-1} & -(l-1)h^{-l} & -(l+1)h^{-l-2} \\ h^{l+2} & h^l & h^{-(l-1)} & h^{-(l+1)} \\ (l+2)(l+1) & l(l-1) & l(l-1) & (l+2)(l+1) \end{vmatrix}; \quad (11)$$

$\Delta_i(h)$ are the algebraic complements of the corresponding elements of the last row of $\Delta(h)$.

It can be shown that the following inequalities are satisfied

$$\psi(r) < 0 \quad (1 < r < h); \quad L\psi < 0. \quad (12)$$

Calculations show that, for $\text{WePr} > 18$ and $J(h) > 0$, the denominator in (7) is positive. We note that realistic values of $\text{WePr} = 10^4 - 10^8$. Thus, for all $f(r)$ for which $J(h) > 0$,

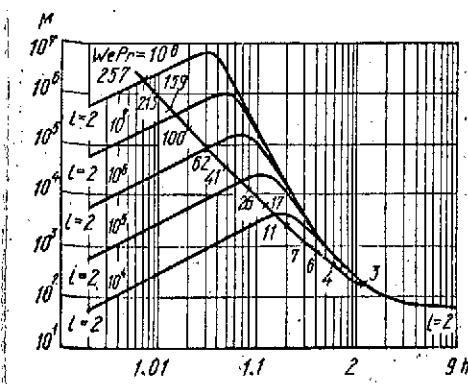


Figure 1. Stability boundary (onset of stationary thermocapillary convection) for spherical liquid layer heated from outside under weightless conditions.

We see from (7) that M increases with increase of Bi , therefore, the stability boundary for $Bi = 0$ is the lower estimate of the boundary for all $Bi \neq 0$.

The calculations results for $Bi = 0$ are shown in Figure 1. On the curve consisting of segments of the $M(h)$ curves for different l and defining the stability boundary there are indicated the values of l for which the minimum of M is reached. We see that these values of l increase monotonically with reduction of h , but for some h which depends on the quantity $WePr$, the stability boundary corresponds to $l = 2$. In other words, with reduction of the spherical layer thickness, the convective motion will consist of an ever increasing number of "cells," but upon reaching some thickness, the perturbations of longest wavelength become the most "hazardous." This agrees well with the known data on thermocapillary convection onset in a flat infinite liquid layer [6] as a result of loss of stability relative to long-wave perturbations for arbitrarily small M . In [7], convection was studied visually in spherical liquid films which arise under the influence of a concentration gradient (exact

the eigenvalues defined by (7)

will be positive (specifically

for $f(r) \leq 0$ or $\frac{dT_0}{dr} \geq 0$, i.e., |

when the temperature decreases

monotonically from the solid wall

to the free surface).

We shall call the quantity

$$\frac{\min}{l} M (l = 1, 2, \dots)$$

the stability boundary for each fixed h .

analog of thermocapillary convection). It is of interest to note that, in the photographs presented in [7], we see both "small-cell" and "large-cell" convection.

Let us examine a rectangular channel of width h and liquid level height l . The free surface is considered plane (contact angle 90°). The temperature distribution $\theta_0 = C_1 + C_2 x$ ($C_2 > 0$), is given on the solid walls Γ_1 , while the condition $\frac{\partial T}{\partial y} = 0$ is given at the free surface.

Here the equilibrium state is obviously impossible and thermocapillary convection will be realized for arbitrarily small C . We shall seek the solution of (2) under the assumption /67 that, for weak liquid motions, the free surface deviations can be neglected. Then, on the flat free surface Γ_0 , there is satisfied the condition $u_y = 0$, which follows from the kinematic condition, and the condition of equality to zero of the tangential stress

$$\mu \frac{\partial u_x}{\partial y} = \frac{\partial \sigma}{\partial T} \frac{\partial T}{\partial x}. \quad (13)$$

For small temperature differences in the considered space, the quantity $\partial \sigma / \partial T$ may be considered constant. In (2) and the boundary conditions, we make the change: $T' = T - \theta_0$. The system of equations for finding \bar{u} , T and the corresponding boundary conditions in dimensionless form is

$$\left. \begin{aligned} \Delta \bar{u} &= \nabla p + (\bar{u} \nabla) \bar{u}, \quad \nabla \bar{u} = 0, \quad \bar{u}|_{\Gamma_1} = 0, \quad u_y|_{\Gamma_0} = 0; \\ \frac{\partial u_x}{\partial y} &= -M \left(\frac{\partial T}{\partial x} + 1 \right) (\Gamma_0); \\ \Delta T &= \text{Pr} \bar{u} \nabla T + \bar{u}_x, \quad T|_{\Gamma_1} = 0, \quad \frac{\partial T}{\partial y}|_{\Gamma_0} = 0. \end{aligned} \right\} \quad (14)$$

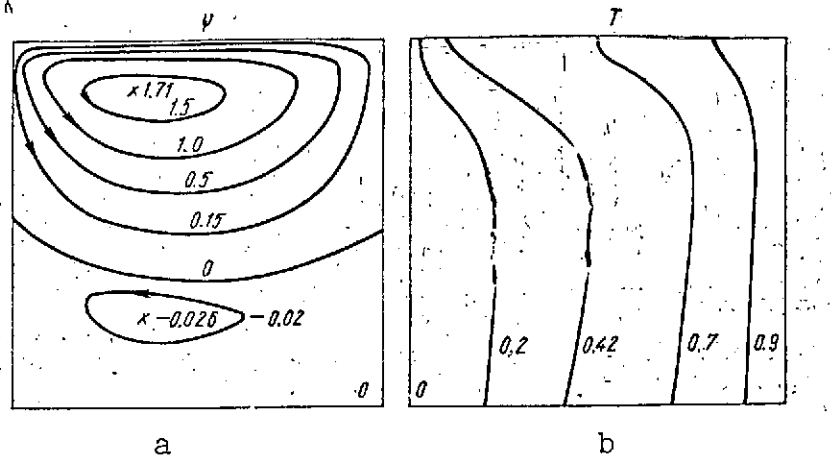


Figure 2. Streamlines and isotherms of steady-state thermocapillary convection in square channel.

It can be shown that, for sufficiently small M , the system (14) has a unique solution which can be obtained in the form of a power law series in M [8]. We continue this unique solution in terms of the parameter M , using for this the Newton-Kantorovich method [9].

In terms of stream function and temperature, the equations of the Newton-Kantorovich method for the considered problem take the form

$$\Delta^2 \psi_{n+1} + \frac{\partial \Delta \psi_n}{\partial y} \frac{\partial \psi_{n+1}}{\partial x} + \frac{\partial \psi_n}{\partial x} \frac{\partial \Delta \psi_{n+1}}{\partial y} - \frac{\partial \Delta \psi_n}{\partial x} \frac{\partial \psi_{n+1}}{\partial y} - \frac{\partial \psi_n}{\partial y} \frac{\partial \Delta \psi_{n+1}}{\partial x} - \frac{\partial \psi_n}{\partial x} \frac{\partial \Delta \psi_n}{\partial y} + \frac{\partial \Delta \psi_n}{\partial x} \frac{\partial \psi_n}{\partial y} = 0; \quad (15)$$

$$\begin{aligned} \frac{\partial \psi_{n+1}}{\partial x} \Big|_{\Gamma_1} = \frac{\partial \psi_{n+1}}{\partial y} \Big|_{\Gamma_1} = 0; \quad \frac{\partial \psi_{n+1}}{\partial x} \Big|_{\Gamma_0} = 0; \quad \frac{\partial^2 \psi_{n+1}}{\partial y^2} \Big|_{\Gamma_0} = -\gamma \left(\frac{\partial T_n}{\partial x} + 1 \right); \\ \Delta T_{n+1} - \frac{\partial \psi_{n+1}}{\partial y} + \text{Pr} \left(\frac{\partial T_n}{\partial y} \frac{\partial \psi_{n+1}}{\partial x} + \frac{\partial \psi_n}{\partial x} \frac{\partial T_{n+1}}{\partial y} - \frac{\partial T_n}{\partial x} \frac{\partial \psi_{n+1}}{\partial y} - \frac{\partial \psi_n}{\partial y} \frac{\partial T_{n+1}}{\partial x} \right) + \text{Pr} \left(\frac{\partial \psi_n}{\partial y} \frac{\partial T_n}{\partial x} - \frac{\partial \psi_n}{\partial x} \frac{\partial T_n}{\partial y} \right) = 0; \\ T_{n+1} \Big|_{\Gamma_1} = 0, \quad \frac{\partial T_{n+1}}{\partial y} \Big|_{\Gamma_0} = 0. \end{aligned} \quad (16)$$

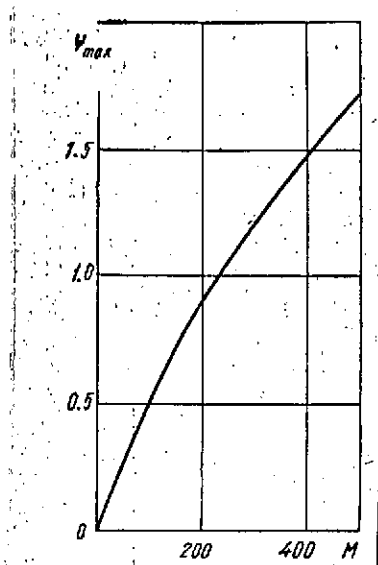


Figure 3. Dependence of ψ_{\max} on M for the flow represented in Figure 2.

We take as the zero approximation (ψ_0, T_0) the solution of the linearized problem [14]. At each step, we solve the problem (15) and then (with known ψ_{n+1}), the problem (16). The solution of the linearized problems at each step was made by the grid method and the grid solutions were found by the Seidel method.

Figure 2 shows the streamlines (a) and isotherms (b) in a channel of square section, obtained for $M = 500$, $Pr = 1$ on a uniform 16×16 grid.

The Newton-Kantorovich method was realized for $M = 5$ with step 5. For $M = 5$, the isotherms are practically vertical and the weak vortex filling the entire channel cross section is symmetric relative to the channel axis. For $M = 500$, the isotherms curve near the free surface, where the convection is most highly developed, and very weak return flow forms in the lower part of the channel.

Figure 3 shows one of the nonlinear characteristics of the resultant convective motion — the dependence of ψ_{\max} on M . We see from the figure that, for $M = 500$, the influence of the nonlinear terms in the stationary convection equations is already quite large.

REFERENCES

1. Scriven, L. E., and C. V. Sternling. Nature, Vol. 187, 1960, pp. 186-187.
2. Kenning, D. B. R. AMR, Vol. 21, No. 11, 1968, pp. 1101-1111.
3. Landau, L. D., and E. M. Lifshits. Mekhanika sploshnykh sred (Mechanics of Continua). Moscow-Leningrad, GITTL (State Technical and Theoretical Press), 1953.
4. Monin, A. S., and A. M. Yaglom. Statisticheskaya gidromekhanika (Statistical Hydromechanics). Vol. 1. Moscow, Nauka Press, 1965.
5. Babskiy, V. G., and I. L. Sklovskaya. Izv. AN SSSR, Mekhanika zhidkosti i gazov, Vol. 3, 1969.
6. Scriven, L. E., and C. V. Sternling. J. Fluid Mech., Vol. 19, No. 3, 1964.
7. Thissen, D. Phys. Chem., Vol. 232, Nos. 1/2, 1966, pp. 27-38.
8. Babskiy, V. G., and Yu. B. Sklovskiy. In the book: Trudy FTINT AN USSR. Voprosy gidrodinamiki i teploobmena v kriogennykh sistemakh (Transactions of the Physico-Technical Institute of Low Temperatures of the Academy of Sciences of the UkSSR. Hydrodynamics and Heat Transfer in Cryogenic Systems). Kharkov, Vol. 1, 1970.
9. Krasnosel'skiy, M. A., et al. Priblizhennoye resheniye operatornykh uravneniy (Approximate Solution of Operator Equations). Moscow, Nauka Press, 1969.

HEAT TRANSFER WITH NUCLEATE BOILING OF LIQUIDS UNDER
WEAK MASS FORCE FIELD CONDITIONS

Yu. A. Kirichenko

We examine the motion of a vapor bubble growing and rising from a flat horizontal heater in the ideal fluid approximation and with account for drag. Estimates are given of bubble life-time, bubble radius at detachment, bubble detachment frequency, and time for the bubble to attain a constant rate of rise. The relations obtained for the microcharacteristics of the boiling process are used to determine the coefficients of heat transfer in developed nucleate boiling. A new form of the equations for describing heat transfer in nucleate boiling in dimensionless parameters is proposed.

Study of the boiling process has considerable practical /68 importance. Without sufficiently good knowledge of the peculiarities of this process, the development of modern power generation (including nuclear), certain branches of industry (chemical and foodstuffs, for example), and cryogenic technology would be unthinkable. Space technology imposes special requirements on the study of boiling, and progress in space technology requires information on liquid boiling under conditions of weak mass force fields and weightlessness. First of all, these data are /69 necessary for such cryogenic fluids as oxygen and hydrogen [1 — 3], which are the most promising rocket fuel components [1 — 3], and helium, which is used to cool the components of electronic and optical devices [3].

Most of the known boiling studies have been devoted to analysis of the integral boiling characteristics which are necessary for engineering calculations (boiling heat transfer coefficients, critical thermal fluxes, etc.). Considerably fewer works have been published on boiling physics, although this field is being developed intensely at the present. However, there is a considerable gap between study of the integral boiling characteristics and study of its "micro-characteristics" (vaporization center density, bubble radius at departure, bubble departure frequency). Only a few studies are known in which an attempt has been made to relate the information on the physics of boiling with the values of the heat transfer coefficients or the critical thermal fluxes.

Obtaining physically valid relationships for the integral boiling characteristics is particularly important for analysis and calculation of thermal processes under weak mass force field conditions. For the calculation of such processes under terrestrial conditions, we can make use of many empirical or semi-empirical formulas. However, the accumulation of analogous experimental data with reduced gravity involves large and frequently insurmountable difficulties.

In the present paper, we attempt to obtain a relation for the heat transfer coefficients only on the basis of the process microcharacteristics.

Vaporization center density. We can assume that the vaporization center density Z is a function of the vapor bubble nucleus radius r_* [4 — 7]:

$$Z = F(r_*) = F\left(\frac{2T_s\sigma}{L\rho^*\Delta T}\right). \quad (1)$$

Here T_s is the saturation temperature, σ is the surface tension coefficient, L is the latent heat of vaporization, ρ'' is the vapor density; ΔT is the difference between the heater and saturation temperatures.

In the first approximation, (1) can be approximated by a power law function of r_*

$$Z = C_z \left(\frac{L\rho''\Delta T}{T_s\sigma} \right)^{n_z}, \quad (2)$$

where C_z is a dimensionless quantity if $n_z = 2$.

The relation (2) with the value $C_z = 625 \cdot 10^{-6}$ m, $n_z = 3$, was obtained in [7] by analyzing all the known data on Z . The scatter of the experimental data relative to this relation amounts to a several hundred percent. The data presented in [7] in the parameter variation range

$$10^7 > \frac{1}{r_*} > 10^8 \text{ m}^{-1},$$

can be represented by the following relation with far greater accuracy

$$Z = 6 \cdot 10^{-7} \left(\frac{L\rho''\Delta T}{T_s\sigma} \right)^3. \quad (3)$$

Bubble departure radii. Evaluation of bubble radii at departure from the heater (departure radii) is usually made using the Fritz formula, obtained from approximate solution of the bubble static stability problem [8].

$$R_d \approx 0.01\gamma \sqrt{\frac{\sigma}{g(\rho - \rho'')}} \quad (4)$$

where γ is the contact angle in degrees; ρ is the density of the liquid. Formula (4) was verified for very slowly growing bubbles

[9]. Their growth rates differed by several orders from the bubble growth rates for developed nucleate boiling. Further studies showed the invalidity of (4) for boiling, primarily because of the very weak dependence of R_d on the pressure p , which this formula yields for $p \ll p_{cr}$. For example, for water, 70 variation of the saturation pressure from 0.12 to 1 bar [10, 11], and from 1 to 10 bar [12] leads to reduction of the departure radius by approximately an order of magnitude in each of the ranges, while (4) yields 6% radius change in the first case and 20% in the second.

For cryogenic liquids, for which the contact angle $\gamma \approx 0$, (4) is not applicable even for $p \approx 1$ bar.

Experiments conducted in recent years under weak mass force field conditions yield still another criterion for validity of (4), namely: dependence of R_d on g [13 — 16]. Figure 1 shows the experimental data on relative bubble radius at departure as a function of load factor η and the relations

$$\frac{R_d}{R_{d1}} = \eta^{-\frac{1}{3}}$$

(solid line), and

$$\frac{R_d}{R_{d1}} = \eta^{-\frac{1}{2}}$$

(dashed line). It is quite obvious that the latter relation, obtained from (4), does not correspond to the experimental data,

The correct value of the departure radius could be obtained from solution of the problem of expanding bubble dynamic stability. However, the known attempt to reduce dynamic stability to quasi-static stability, performed insufficiently rigorously, did not yield positive results [13].

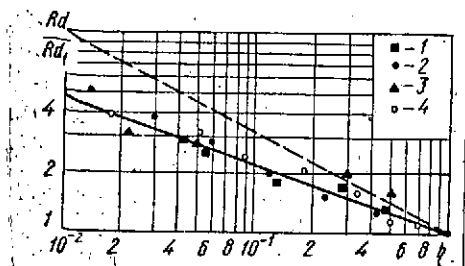


Figure 1. Relative bubble departure radius versus load factor.

1- from data of [12]; 2- from data of [13]; 3- from data of [14, 15]; 4- from data of [15].

The departure radius has been evaluated on the basis of hydrodynamics in several studies [18 — 21]. In [17, 18], the departure conditions were found from equality of the drag and lift forces. This estimate cannot be considered correct: if the bubble contacts the wall, the drag formulas for a nonexpanding sphere in an infinite liquid will not be

valid; however, if the bubble does not contact the wall, the question of its velocity remains unresolved.

In [19], the instant of departure was determined from joint solution of a system of two equations: for the bubble radius and for the motion of the center of gravity of the expanding bubble in an infinite liquid. This method is nearly exact only in application to boiling on fine wire heaters ($r_1 \ll R_d$, where r_1 is the wire radius) in superheated liquid.

In spite of the approximate nature of the R_d estimates in [17 — 21], the formulas obtained therein apparently have the correct structure, since they yield a rational dependence of R_d on p and g .

We shall try to evaluate R_d more rigorously, examining bubble behavior near a heater with account for the influence of the latter on bubble motion. We note that the equation of motion of the bubble does not in itself yield the departure conditions, and in order to evaluate R_d , it is necessary to have still another condition. Such a condition can be the experimentally

determined relationship between bubble radius R and distance S of the bubble center from the heater at the instant of departure [20]: $S \approx 1.5 R$. This condition is satisfied for bubble departure from a "stem," which is characteristic for boiling at low Jakob numbers ($Ja < 10 - 20$) [21]. In the case of liquid boiling under saturation conditions, it is better to make the departure radius estimate not at the instant of formal bubble departure from the wall, but rather at the instant when the bubble no longer receives heat from the heater.

Bubble growth on a heater. We identify the following bubble motion stages: stage I is bubble growth (from nucleation to "stem" formation); stage II is departure (from "stem" formation to its "rupture"); stage III is ascent (after bubble departure from "stem"). We shall assume that the bubble retains a spherical shape in all stages of the motion.

The bubble equation of motion for stage I can be written in the form [22, 23]

/71

$$S = R = \beta \tau^n. \quad (5)$$

According to theoretical studies [24 — 26], $n = 0.5$ with growth modulus β equal to

$$\beta = C_\beta Ja^{n_\beta} a^{\frac{1}{2}} = C_\beta \left(\frac{\lambda \Delta T}{\rho' La} \right)^{n_\beta} a^{\frac{1}{2}}, \quad (6)$$

where λ is the thermal conductivity and a is the thermal diffusivity.

For small Jakob numbers ($Ja < 10 - 20$), characteristic for boiling of cryogenic liquids and freons at $p \geq 1$ bar and water at $p > 10$ bar, we can take $n_\beta = 0.5$ [23, 26] with adequate accuracy. In this case, (6) becomes the Labuntsov formula [26],

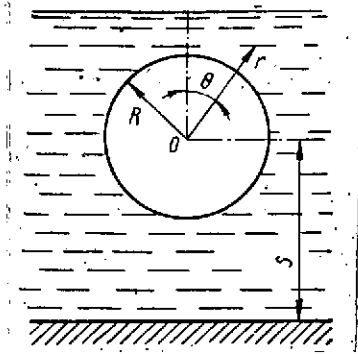


Figure 2. Illustration for calculating bubble motion near a wall.

which can be written approximately in the form

$$\beta \approx 3 \left(\frac{\lambda \Delta T}{\rho'' L} \right)^{\frac{1}{2}} \quad (7)$$

Equation of motion of expanding bubble near horizontal wall. We shall first determine the forces acting on a spherical bubble, assuming that the liquid

flow is potential and neglecting the presence of a temperature field, vapor momentum, and surface tension forces.

We shall seek the velocity field near the bubble by solving the Laplace equation for the velocity potential with the corresponding boundary conditions [27]. We obtain the velocity potential Φ with account for wall influence by the image method [27, 28] in the form

$$\Phi = S \left[\frac{R^3}{2r^2} + \left(\frac{R^3}{2r^3} + r \right) \frac{R^3}{8S^3 - R^3} \right] \cos \theta + R \left[\frac{R^2}{r} + \left(\frac{R^3}{2r^3} + r \right) \frac{2R^2 S}{8S^3 - R^3} \cos \theta \right] \quad (8)$$

The meaning of the quantities in (8) is clear from Figure 2.

It is easy to obtain from (8) the limiting cases for Φ in an infinite liquid ($S \gg R$) [27] and for a bubble in contact with the wall ($S \equiv R$).

Using (8) and the Bernoulli equation [27, 28], we obtain the equation for the pressure, after integrating which over the surface of the bubble we find the expression for the vertical force component

$$F = F_R + F_g. \quad (9)$$

Here F_g is the lift (Archimedes) force

$$F_g = -\frac{4}{3} \pi R^3 g \rho; \quad (10)$$

F_R is the dynamic reaction force acting from the liquid on the expanding and moving bubble (reaction force)

$$\begin{aligned} \frac{F_R}{\frac{4}{3} \pi R^2 \rho} = & \frac{1 + 2\kappa^3}{2(1 - \kappa^3)} \ddot{S}R - \frac{9\kappa^4}{(1 - \kappa^3)^2} \dot{S}^2 + \\ & + \frac{3}{2} \cdot \frac{1 - 2\kappa^3 - 2\kappa^6}{(1 - \kappa^3)^2} \dot{S}\dot{R} + \frac{9}{2} \cdot \frac{\kappa^2}{(1 - \kappa^3)^2} \dot{R}^2 + \frac{3}{2} \cdot \frac{\kappa^2}{1 - \kappa^3} R\ddot{R}, \\ & \kappa = R/2S. \end{aligned} \quad (11)$$

For a bubble in contact with the wall ($S = R$, $\kappa = 0.5$),

$$F_R = \frac{4}{3} \pi \rho R^3 \left(\frac{8}{7} \ddot{R}R + \frac{15}{7} \dot{R}^2 \right). \quad (12)$$

At the beginning of stage I, bubble motion $F_R > -F_g$ and 72 bubble detachment from the wall are not possible, since the resultant force F forcing the bubble to the wall is significantly greater than zero in (9).

The initiation of stage II can be considered to be the condition

$$F_R = -F_g. \quad (13)$$

Substituting (10) and (12) into (13) and considering that the bubble grows following the law (5), we obtain the expressions for the radius R_0 and time τ_0 characterizing the end of stage I:

$$R_0 = \left[\frac{n(23n - 8)}{7} \right]^{\frac{n}{2-n}} \beta^{\frac{2}{2-n}} g^{-\frac{n}{2-n}}; \quad (14)$$

$$\tau_0 = \left[\frac{n(23n-8)}{7} \right]^{\frac{1}{2-n}} \beta^{\frac{1}{2-n}} g^{-\frac{1}{2-n}} \quad (15)$$

In the case $n = 0.5$, we obtain in place of (14) and (15):

$$R_0 = 0.63\beta^{\frac{4}{3}} g^{-\frac{1}{3}}; \quad (14')$$

$$\tau_0 = 0.4\beta^{\frac{2}{3}} g^{-\frac{2}{3}}. \quad (15')$$

For stages II and III, noting that in (9)

$$F = -\frac{d}{dt} (M''u) \approx 0, \quad (16)$$

since the bubble mass M'' is small, after using (10) and (11), we obtain the equation of motion

$$\begin{aligned} & \frac{1+2\kappa^3}{2(1-\kappa^3)} \ddot{S}R - \frac{9\kappa^4}{(1-\kappa^3)^2} \dot{S}^2 + \frac{3}{2} \cdot \frac{1-2\kappa^3-2\kappa^6}{(1-\kappa^3)^2} \dot{S}\dot{R} + \\ & + \frac{9}{2} \cdot \frac{\kappa^3}{(1-\kappa^3)^2} R^2 + \frac{3}{2} \cdot \frac{\kappa^3}{1-\kappa^3} \ddot{R}R - gR = 0, \end{aligned} \quad (17)$$

where $\kappa = R/2S$.

For an expanding bubble in an infinite liquid (far from the wall $S \gg R$, $\kappa \approx 0$), we obtain

$$\ddot{S}R + 3\dot{S}\dot{R} = 2gR. \quad (18)$$

Equation (17) is correct beginning from the instant of time τ_0 and the corresponding radius R_0 , defined by (15) and (14').

Equation (17) was solved on an M-20 digital computer by the Runge-Kutta method with the initial conditions $R_0 = S(\tau_0)$, $\dot{R}(\tau_0) = \dot{S}(\tau_0)$ for $n = 0.5$. Some of the relations obtained are shown in Figure 3. Using this solution and the condition $S \approx 1.5$, we can find the values of the detachment time τ_d and bubble radius R_d at detachment. We note that, for practical purposes, we can use the solution of (18) with the same boundary conditions.

Approximate estimates of bubble detachment radii and detachment time. Using (5), we obtain, on the basis of (18),

$$\dot{S}\tau + 3nS = 2g\tau. \quad (19)$$

The solution of (19) with the initial conditions $S(\tau_{01}) = R(\tau_{01})$, $\dot{S}(\tau_{01}) = \dot{R}(\tau_{01})$ will have the form

$$S = \frac{2g}{3n+1} \left[\frac{\tau^2}{2} + \frac{1}{3n-1} \frac{\tau_{01}^{3n+1}}{\tau^{3n-1}} \right] - \frac{n}{3n-1} \beta \tau_{01}^n \frac{\tau_{01}^{3n-1}}{\tau^{3n+1}} + \frac{1}{3n-1} [(4n-1)\beta \tau_{01}^n - g\tau_{01}^2]. \quad (20)$$

Setting $n = 0.5$ in (20) and considering that $\tau_{01} = \tau_0$, we obtain from (15') the approximate value of the departure time τ_d : $\tau_d \approx 4.5 \tau_0$.

Thus, for $n = 0.5$

$$R_d = C_R \beta^{\frac{4}{3}} g^{\frac{1}{3}}; \quad (21)$$

$$\tau_d = C_\tau \beta^{\frac{2}{3}} g^{-\frac{2}{3}}, \quad (22)$$

where $C_R \approx 1.35$, $C_\tau = C_R^2$.

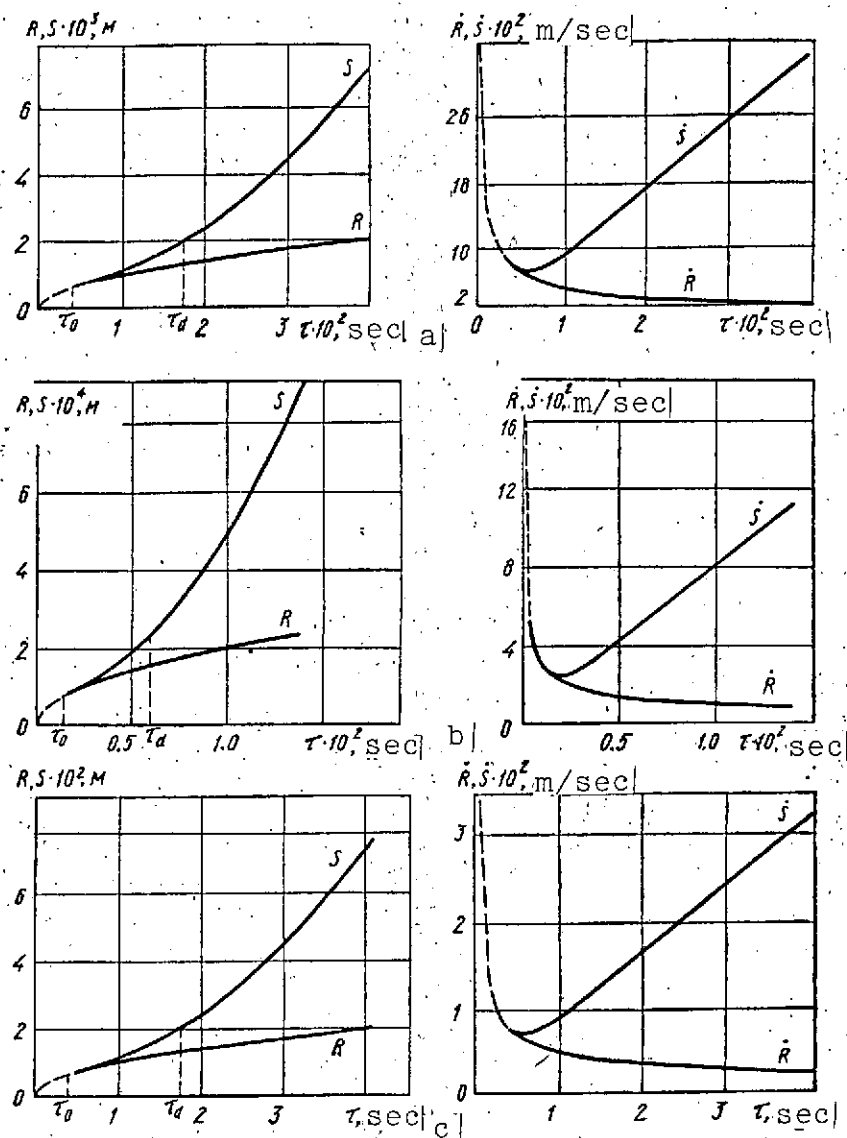


Figure 3. Bubble motion near a wall in an ideal liquid for $g = g_1$, $\beta = 1 \text{ cm/sec}^{1/2}$ (a); for $g = 10^{-3} g_1$, $\beta = 1 \text{ cm/sec}^{1/2}$ (b); and for $g = g_1$, $\beta = 0.2 \text{ cm/sec}^{1/2}$ (c).

If $n \neq 0.5$, the formulas for R_d and τ_d will have the structure of Formulas (14) and (15), i.e.,

$$R_d = C_R \beta^{\frac{2}{2-n}} g^{-\frac{n}{2-n}}; \quad (23)$$

$$\tau_d = C_R^n \beta^{\frac{1}{2-n}} g^{-\frac{1}{2-n}} \quad (24)$$

It follows from (23) that the exponent of g in this formula may vary over quite wide limits depending on the value of n ; the variation range $n = 0.35$ to 0.75 corresponds to variation of the exponent in the relation $(R_d/R_{d1}) = g^{-k}$ in the limits $k = 0.21$ to 0.6 . /74

Comparison of estimates obtained for R_d and τ_d with experimental data. Expressions (23) and (24) were obtained for expanding spheres in ideal undisturbed liquid without account for surface tension forces. In real boiling conditions, the coefficients C_R and C_τ may be either larger or smaller than the values found from (23) and (24).

Let us make a rough estimate of the influence of liquid nonideality, calculating the drag force in terms of the energy dissipated

$$F_v \approx 12\pi\mu RS, \quad (25)$$

where ν is the kinematic viscosity.

If the solution of (19) for $n = 0.5$ for bubble motion in an infinite liquid has the form

$$S = \frac{g\tau^3}{2.5}, \quad (26)$$

then, with account for (25), we obtain

$$S \approx \frac{g\tau^3}{2.5 + 18\nu/\beta^2}. \quad (27)$$

It follows from (26) and (27) that liquid nonideality can be neglected if $\beta \ll \sqrt{8\nu}$. For water $\beta \ll 0.16$ cm/sec^{1/2}, for oxygen

and diethyl ether, $\beta \ll 0.11 \text{ cm/sec}^{1/2}$.

We see from comparison of (26) and (27) that, with decrease of β , the time τ_d of bubble contact with the wall increases, and consequently, the radius R_d increases. Account for surface tension forces yields a similar effect. On the other hand, the disturbances caused by neighboring bubble motion may reduce bubble lifetime to τ_0 . Short bubble lifetime τ_d is more probable than long, which leads to shift of the maximum on the bubble detachment frequency probability distribution curve in the direction of smaller time values [12]. On the basis that $\tau_g \approx 4.5 \tau_0$ we can conclude that the possible scatter of bubble detachment time and radii

$$\frac{\Delta \tau_d}{\tau_d} \approx \pm 60\%; \quad \frac{\Delta R_d}{R_d} \approx \pm 30\%. \quad (28)$$

In view of the fact that R_d is a more stable characteristic than τ_d , we shall compare the value of R_d calculated using (24) with the experimental data.

Table 1 shows the values of C_R calculated from the results of several studies. The growth modulus β was determined from the experimental data as $\beta = R_{de}/\sqrt{\tau_{de}}$. In those cases when the bubble growth time was not indicated in the studies, we took $\tau_d = 1/f$. The average value of C_R from all the studies amounts to about 1.8 with maximal scatter of about $\pm 40\%$, which is in agreement with the estimate (28). Table 1 also presents the values of the calculated radii.

TABLE 1*

DATA ON BUBBLE DETACHMENT CHARACTERISTICS

R_{dE} , mm	$\frac{1}{\tau_d}$, sec ⁻¹	θ , cm sec ^{1/2}	R_{dT} , mm	C_R	Liq., pressure	Source
1.0	36	0.6	0.9	2.0	Water, 1 bar	[30]
1.6	20	0.72	1.2	2.5	Ethyl alcohol, 40 bar	
					Film boiling	[30]
0.35	91	0.33	0.41	1.54	Freon-12, 1 bar	[23]
0.256	61	0.117	0.21	2.1	Freon-12, 0.97 bar	[23]
0.318	73	0.315	0.34	1.67	Freon-142	[23]
0.296	50	0.208	0.223	2.4	Freon-113, 0.965 bar	[23]
0.3	50	0.212	0.217	2.5	Nitrogen, 1 bar	[31]
1.25	62	0.93	1.63	1.4	Water, 1 bar	[12]
0.55	108	0.57	0.85	1.17	Ethyl alcohol, 1 bar	[12]
0.28	86	0.51	0.37	1.34	Water, 4 bar	[12]
0.16	85	0.32	0.195	1.6	Water, 9 bar	[12]
14.25	20.4	6.4	21.1	1.22	Ethyl alcohol, 0.06 bar	[11]
0.55	127	0.62	0.94	1.05	Ethyl alcohol, 1 bar	[11]
0.105	165	0.135	0.124	1.52	Nitrogen	[32]
0.15	72	0.129	0.118	2.29	Nitrogen	[32]
0.19	54	0.14	0.13	2.6	Nitrogen	[32]

*[Translator's Note: Commas in numbers indicate decimal points.]

Table 2 presents the experimental and calculated values of the detachment radii obtained under weak mass force field conditions (for $\eta = 1$). The calculation was made for $C_R = 1.8$. In all cases, the agreement with the experimental data is within the limits of a few percent [the applicability of (21) for low gravity is seen from Figure 1].

Bubble detachment frequency. The bubble detachment frequency f may be written in the form

$$f = \frac{1}{\tau_d + \tau_w} \quad (29)$$

The bubble detachment time τ_d is found from (22) or (24). For a rough estimate of the waiting time τ_w , we use the Gane-Griffiths relation for minimal bubble formation time (30):

TABLE 2*
DATA ON VAPOR BUBBLE DYNAMICS

Liquid	$\beta, \text{cm/sec}^{1/2}$	R_d, mm		Source
		Exp.	Calc.	
Water	1.35	3	2.7	[12]
Water	0.8	1.33	1.34	[13]
Oxygen	0.235	0.24	0.26	[14,15]
Diethyl ether	0.42	0.6	0.57	[15]

*[Translator's Note: Commas in numbers indicate decimal points.]

$$\tau_w \approx \frac{144}{\pi a} \left(\frac{T_s \sigma}{\rho^* L \Delta T} \right)^2 \quad (30)$$

The relative influence of τ_d and τ_w on the magnitude of the frequency may vary depending on the p , g , and q variation ranges. From comparison of τ_d and τ_w , it is easy to identify two limiting cases.

$$f \rightarrow f_d = \frac{1}{\tau_d} \approx 0.15 \left(\frac{\rho^* L}{\lambda \Delta T} \right)^{\frac{1}{3}} g^{\frac{2}{3}} \text{ for } g \rightarrow 0, \quad p \rightarrow p_{cr}; \quad (31)$$

$$f \rightarrow f_w = \frac{1}{\tau_w} \approx 0.022a \left(\frac{\rho^* L \Delta T}{T_s \sigma} \right)^2 \text{ for } g \rightarrow \infty, \quad p \rightarrow 0. \quad (32)$$

It follows from (31) and (32) that the frequency is more stable in magnitude and depends less on q for high pressures than for low pressures; the same conclusion on stability can also be drawn for small gravity force accelerations. For liquids such as the cryogenics or freons, a pressure $p > 1$ bar can be considered high, for water $p > 10$ bar is high.

Thus, in the case considered, we can use (21) and (22) to calculate R_d and τ_d , taking $C_R = 1.8$, and find the bubble detachment frequency as $f = \frac{1}{\tau_d}$.

Bubble motion after detachment from heater. The nature of bubble motion in stage III depends essentially on whether the bubble continues to expand or retains constant volume. It was shown previously that the presence of a resistance force for an expanding bubble leads only to change of the magnitude of its acceleration [see (21)] without altering the nature of the motion. The physical meaning of this is that the lift force increases for an expanding bubble approximately as R^3 (i.e., faster than the resistance force R or R^2). At the same time, the solution of (18) with account for F_v with $R = 0$ yields $S \rightarrow \text{const}$ for $\tau \rightarrow \infty$, i.e., for constant volume, the bubble acquires constant velocity. /76

Let us examine the drag force [29]

$$F_D = C_D \frac{\pi R^2 \rho \dot{S}^2}{2}. \quad (33)$$

We introduce into (17) a term expressing the drag in the form $F_D = 3C_D S^2/8$. For sufficiently small values of κ (for example, $\kappa < 0.3$), (17) will differ from (18) only in the presence of the second term, which may be neglected if $\kappa^4 < C_D/24$. Taking $C_D \approx 0.6$, we obtain $\kappa < 0.4$, $S < 1.25$. Since bubble detachment takes place for $S = 1.5 R$, in the case when, after detachment $R = \text{const}$, the equation of bubble motion reduces to the form

$$\frac{1}{2} \ddot{S} R + \frac{3C_D}{8} S^2 - gR = 0. \quad (34)$$

The solution of this equation for the velocity \dot{S} will have the form

$$\dot{S} = 2 \sqrt{\frac{2gR}{3C_D} \frac{\exp\left[2 \sqrt{\frac{3C_D g}{2R}} (\tau - \tau_d)\right] - \zeta}{\exp\left[2 \sqrt{\frac{3C_D g}{2R}} (\tau - \tau_d)\right] + \zeta}}. \quad (35)$$

where

$$\zeta = \frac{2 \sqrt{\frac{2gR}{3C_D}} - \dot{S}_d}{2 \sqrt{\frac{2gR}{3C_D}} + \dot{S}_d}, \quad \dot{S}_d = \dot{S}(\tau_d).$$

The magnitude of the acceleration for sufficiently large values of τ is

$$\ddot{S} \approx 8g\zeta \exp \left[-2 \sqrt{\frac{3C_D g}{2R}} (\tau - \tau_d) \right]. \quad (36)$$

We shall consider the time the bubble reaches constant velocity τ_c to be the instant of time at which its acceleration decreases by a factor of e^3 , i.e., by about a factor of 20; in this case, we obtain from (36)

$$\tau_c - \tau_d = \frac{3}{2} \sqrt{\frac{2R}{3C_D g}} \approx \sqrt{2.5 \frac{R}{g}}, \quad (37)$$

if $C_D \approx 0.6$.

The statements encountered in the literature that the bubble acquires constant velocity immediately after detachment [12, 13, 23], are valid in the limits of the estimate (37). For example, for liquid oxygen [14, 15], for $g \approx 10^3$ cm/sec², $R \approx 0.024$ cm, $C_D \approx 0.6$, we obtain $\tau_c - \tau_d \approx 8 \cdot 10^{-3}$ sec.

The Runge-Kutta method was used on an M-20 digital computer to solve (17), to the left side of which we added the term $3C_D S^2/8$, accounting for liquid nonideality with the additional condition $R = R_d$, $R = 0$ for $\tau \geq \tau_d$ (τ_d was determined from the condition $S_d = 1.5 R_d$). One of the solutions is shown in Figure 4 for $\beta = 0.2$ cm/sec^{1/2} and $g = 980$ cm/sec^{1/2}. It is not

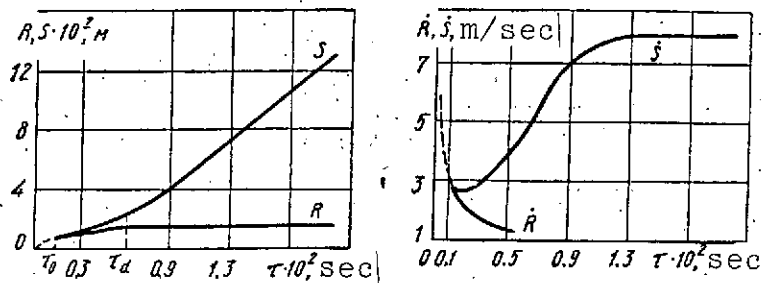


Figure 4. Bubble motion near wall in viscous liquid with constant value of the radius after detachment ($g = g_1$, $\beta = 0.2 \text{ cm/sec}^{1/2}$).

difficult to note the very good agreement of the time segments $\tau_c - \tau_d$ obtained from the exact solution (see Figure 3c) and the approximate estimate (37).

Heat transfer with developed nucleate boiling. The overwhelming majority of the known formulas describing heat transfer intensity for developed nucleate boiling were obtained by analysis of experimental data in dimensional criteria [8, 33, 34]. Most of these formulas were obtained for high-boiling liquids; however, some of them are quite general. For example, the formulas of Kutateladze [8, 33] and Borishanskiy-Minchenko [34] describe quite well boiling heat transfer of certain cryogenic liquids [35]. The results of these studies indicate that, in evaluating the heat transfer coefficient α for nucleate boiling, the viscosity can be neglected in the first approximation. Moreover, the formulas constructed using completely different systems of defining criteria (for example, those including or not including g as a parameter) yield equally good results when evaluating α in definite ranges of the regime parameters [33]. Hence we can conclude that the existing semi-empirical relations for evaluating the dependence of α on g are not applicable.

The similarity criteria system used in such relations is not complete, and even if the experiment and its analysis are conducted properly, several factors influencing the process may not be taken into account. The situation in this case differs radically from that which is observed in many problems of free convective heat transfer without boiling, when the dimensionless complex containing g is determined uniquely.

In order to evaluate the dependence of α on g for developed nucleate boiling, we shall try to obtain a formula for α on the basis of a simple physical model, using only the information on boiling "microstructure." If such a formula yields the correct dependence of α on the thermal flux density q and p , then we can be confident of the validity of the dependence on g if the dependence on g of the basic "microcharacteristics" (Z , R_d , f) appearing in the formula is correct.

Let us examine the case of developed nucleate boiling. We restrict the range of thermal flux densities by the following assumptions: 1) all the heat entering the liquid from the heater goes to vaporization; 2) the bubbles do not interact with one another; 3) the thermal flux density is proportional to the vaporization center density. With account for these assumptions, we obtain

$$q = \frac{4}{3} \pi R_d f L \rho'' Z. \quad (38)$$

It is not difficult to find from (38) the expression for the heat transfer coefficient $\alpha = q/\Delta T$, if the dependence of Z , R_d , and f on the physical quantities and temperature difference ΔT between the heater and liquid are known (all the arguments and derivations are made for a liquid boiling under saturation conditions).

Setting $f = 1/\tau_d$, and substituting (2), (21), (22), and (6) into (38), we obtain

$$q = B \lambda^{\frac{10}{3} n_\beta} a^{\frac{5-10n_\beta}{3}} g^{-\frac{1}{3}} (T_s \sigma)^{-n_z} (L \rho^n)^{\frac{3+3n_z-10n_\beta}{3}} \Delta T^{\frac{10n_\beta+3n_z}{3}}, \quad (39)$$

where

178

$$B = \frac{4}{3} \pi C_R C_\beta^{\frac{10}{3}} C_z.$$

Transforming (39), we find the heat transfer coefficient α in the form

$$\alpha = B_1 \frac{\lambda^{\frac{10n_\beta}{10n_\beta+3n_z}} a^{\frac{5-10n_\beta}{10n_\beta+3n_z}} (L \rho^n)^{\frac{3+3n_z-10n_\beta}{10n_\beta+3n_z}} q^{\frac{10n_\beta+3n_z-3}{10n_\beta+3n_z}}}{(T_s \sigma)^{\frac{3n_z}{10n_\beta+3n_z}} g^{\frac{1}{10n_\beta+3n_z}}}, \quad (40)$$

where $B_1 = B^{\frac{3}{10n_\beta+3n_z}}$.

Denoting

$$r = \frac{10n_\beta + 3n_z - 3}{10n_\beta + 3n_z}, \quad (41)$$

we obtain another form of (40)

$$\alpha = B_1 \frac{\lambda^{\frac{10n_\beta}{3}(1-r)} a^{\frac{5-10n_\beta}{3}(1-r)} (L \rho^n)^{1 + \left(1 - \frac{20}{3} n_\beta\right)(1-r)}}{(T_s \sigma)^{n_z(1-r)} g^{\frac{1}{3}(1-r)}} q^r. \quad (42)$$

In the limits of the selected physical boiling model (40) and (42) include all possible variants of connection between ΔT , q , T_s and the physical quantities characteristic for boiling. These formulas in essence include the case when the thermal flux density q is not proportional to Z . The concrete structure of

(40) will be determined when two of the three characteristic numbers n_β , n_z , r are specified.

Let us evaluate the possible dependence of α on g using (42). We see that the exponent r of q determines uniquely the exponent of g . Considering that r varies in the limits $r = 0.6$ to 0.9 , we find that α may depend on g as

$$\alpha \sim g^{-k}, \quad (43)$$

where $\frac{2}{15} > k > \frac{1}{30}$.

The experimental data can be compared with the estimate (43) only qualitatively. Under weak mass force field conditions, the experimental data are contradictory and unreliable [36], however, for horizontal heaters in the overwhelming majority of the studies, it was found either that α was independent of g [12 — 14, 37] or α increased slightly with decrease of g [38 — 43]. Marked decrease of α with reduction of g was observed only in [41], where boiling of water and alcohol on vertical wires was investigated. All the cited experimental studies were made either under conditions of brief weightlessness aboard airplanes, in a free-fall facility, or by simulating weightlessness under surface conditions. The accuracy of mass force field intensity and weightlessness realization in these experiments was in the range of $\pm(1 — 3)\%$ of the Earth's gravity force acceleration g_1 , and in nearly all cases, the error was positive only.

The largest heat transfer coefficient increase in weightlessness ($g/g_1 \approx 0.014$) was observed for water boiling on horizontal wires (about 30%) [41]. Based on the above discussion, we obtain $k \approx (1/12 \text{ to } 1/18)$, which does not contradict the estimate (43).

For comparison, we note that the Kutateladze or Borishanskiy-Minchenko formulas, where $k = -0.2$, yield for the same weightlessness realization accuracies, increase of α by a factor of two. Such a large change of α could not remain unnoticed in the experiments.

We shall restrict examination of the heat transfer intensity /79 question to cryogenic liquids (helium, hydrogen, nitrogen, oxygen) with $p > 1$ bar. For these cases, we will have $Ja < 10 - 20$, $r_*^{-1} > 10^6 \text{ m}^{-1}$ (as mentioned above, these same values of Ja and r_* are characteristic for the freons with $p > 1$ bar and for the high-boiling liquids with sufficiently high pressure, for example, for water with $p > 10$ bar).

Using (3), (21), (22), and (7), we obtain from (40)

$$\alpha = 0.094 \lambda^{\frac{5}{11}} (T_s \sigma)^{-\frac{6}{11}} (L \rho^*)^{\frac{4}{11}} g^{-\frac{1}{11}} q^{\frac{8}{11}}. \quad (44)$$

Let us compare (44) with the known experimental data. We note that disagreement between the absolute experimental and calculated values of α still does not indicate that the theory is incorrect. The experimental values of α may themselves differ considerably, depending on the material and condition of the heater surface, its geometry, and so on. For example, the heat transfer coefficients for freon boiling may differ significantly simply because of different heater roughness [23].

The coefficient B_1 will depend on the kind of liquid, heater surface condition, and so on, since these factors determine the constants C_β and C_z . Moreover, the values of C_β and C_z used in deriving (44) were taken from data for high

TABLE 3*
EXPERIMENTAL AND CALCULATED VALUES OF α

Liquid	p, bar	$T_s, ^\circ K$	$q, W/m^2$	$\alpha, W/m^2/deg$		Source
				Exp.	Calc.	
Oxygen	1	90	16 000	2400	5350	[44]
				4000		[45]
				5000		[35]
				10 300		[46]
Nitrogen	10	118,5	16 000	4840	9055	[44]
				3300		[47]
				10 800		[46]
				8200		[35]
Freon-12	1	77	20 000	4500	7000	[45]
						[47]
				7640		[47]
				960—3000		[23]
Water	10	103	20 000		15 400	[47]
						[23]
				12 500		[23]
				15 500		[48]
Water	100	583	233 000	26 800	32 000	[48]
				73 500		[48]
						[48]
						[48]

*[Translator's Note: Commas in numbers indicate decimal points.]

boiling liquids. Their values may be different for the cryogenic liquids.

In spite of these limitations, (44) provides very good agreement with the experimental data, even when calculating the absolute values of α (Table 3). For freon-12 and water, the calculated values fall in the experimental scatter limits. For nitrogen and oxygen with $p > 1$ bar, they practically coincide with the data obtained on flat heaters [35] and lie in the experimental scatter limits for cylindrical heaters [44 — 47].

More informative is the dependence of α on p . Table 4 shows the ratios $\alpha(p_2)/\alpha(p_1)$ for helium, nitrogen, oxygen, freon-12, and water, calculated using (44) and the known semi-empirical relations. It is not difficult to note that (44) describes the variation of α with p better than any of the relations examined

TABLE 4*

HEAT TRANSFER COEFFICIENT DEPENDENCE ON PRESSURE

Author	Helium	Nitrogen	Oxygen	Freon-12	Water	Water
	$p_1 = 0,5 \text{ bar}$ $p_2 = 1 \text{ bar}$	$p_1 = 1 \text{ bar}$ $p_2 = 10 \text{ bar}$	$p_1 = 1 \text{ bar}$ $p_2 = 10 \text{ bar}$	$p_1 = 1 \text{ bar}$ $p_2 = 18,7 \text{ bar}$	$p_1 = 1 \text{ bar}$ $p_2 = 10 \text{ bar}$	$p_1 = 10 \text{ bar}$ $p_2 = 100 \text{ bar}$
Borishanskiy-Minchenko	2,0	2,2	1,6	2,6	1,4	2,55
Kutateladze	2,2	2,25	1,8	2,7	1,7	2,8
Labuntsov	1,2	1,2	1,4	1,2	1,4	1,65
Kruzhilin-Averin	1,2	1,3	1,2	1,2	1,5	1,5
Kirichenko	1,6	2,2	1,8	4,7	2,15	3,1
Experimental values	1,7[49,50]	2,35[47]	2,1[44]	5,7; 4,7 [23,51]	1,51; 1,48 [52,48]	2,75; 2,7 [52,48]

*[Translator's Note: Commas in numbers indicate decimal points.]

for the liquids in question (the only exception is water in the /80 pressure range $p = 1 - 10 \text{ bar}$).

System of similarity criteria for developed nucleate boiling.

Applying the methods of dimensional analysis to (44), we obtain

$$\frac{T_s}{\Delta T} = 0.094 \left(\frac{L \rho^* \lambda T_s}{q \sigma} \right)^{\frac{4}{11}} \left(\frac{q \lambda T_s}{\sigma^2 g} \right)^{\frac{1}{11}} \quad (45)$$

The left side of (45) plays the role of a modified Nusselt number

$$\tilde{Nu} = \frac{\alpha l_0}{\lambda} = \frac{\alpha}{q} T_s = \frac{T_s}{\Delta T} \quad (46)$$

where the characteristic length

$$l_0 = \frac{\alpha \Delta T}{q} \cdot \frac{T_s}{\Delta T} \quad (47)$$

is the product of the thermal boundary layer thickness $\frac{\alpha \Delta T}{q}$ and the parametric criterion $K_* = \frac{T_s}{\Delta T}$.

The first dimensionless complex in the right side is the ratio of the thermal boundary layer thickness to the vapor bubble nucleus radius

$$K_r = \frac{l_0}{2r_*} K_T = \frac{L\rho^*\Delta T}{T_s\sigma} \cdot \frac{\lambda T_s}{q} \cdot \frac{T_s}{\Delta T} = \frac{L\rho^*\lambda T_s}{q\sigma}. \quad (48)$$

The second dimensionless complex is a modification of the Jakob number (with account for the magnitude of the vapor productivity of an individual vaporization center)

$$\tilde{Ja}_g^2 = Ja^2 K_T^2 K_r^2 \frac{a^2 q^3}{g\lambda^3 T_s^3} = \frac{q\lambda T_s}{g\sigma^2}. \quad (49)$$

The general form of (45) in dimensionless variables is

$$K_T = B_1 K_r^{n_1} \tilde{Ja}_g^{n_2} \tilde{Ja}^{n_3}, \quad (50)$$

where $\tilde{Ja} = Ja K_T$ is still another modification of the Jakob number. Within the framework of the adopted physical boiling model, the similarity criteria system (50) is complete. The influence of viscosity on boiling heat transfer can be taken into account with the aid of the Prandtl number $Pr = \frac{\nu}{a}$.

REFERENCES

1. Solid Propellant Rocket Engines. Moscow, Mir Press, 1966.
2. New Directions in Cryogenic Engineering. Moscow, Mir Press, 1966.
3. Fastovskiy, V. G., Yu. V. Petrovskiy, and A. Ye. Rovinskiy. Krogennaya tekhnika (Cryogenic Engineering). Moscow, Energiya Press, 1967.
4. Griffith, P., and J. D. Wallis. In the book: Physics of Boiling, Moscow, Mir Press, 1964.

5. Labuntsov, D. A. Teploenergetika, Vols. 12 and 19, 1959; 81
Vol. 5, 1960.
6. Nesis, E. I. UFN, Vol. 87, No. 4, 1965.
7. Zhukhov, K. A. In the book: Trudy TsKTI, 91. Aerodinamika
i teploobmen v rabochikh elementakh energooborudovaniya
(Transactions of the Central Boiler and Turbine Institute.
Aerodynamics and Heat Transfer in Powerplant Components).
Leningrad, 1969.
8. Kutateladze, S. S. Osnovy teorii teploobmena (Fundamentals
of Heat Transfer Theory). Novosibirsk, Nauka Press,
Siberian Division, 1970.
9. Fritz, W., and W. Ende. In the book: Physics of Boiling.
Moscow, Mir Press, 1964.
10. Kutateladze, S. S., and N. N. Mamontova. IFZh, Vol. 12,
No. 2, 1957.
11. Tolubinskiy, V. T., and J. N. Ostrovsky. Int. J. Heat
and Mass Transfer, Vol. 9, No. 10, 1966, p. 1463.
12. Usiskin, C. M., and R. S. Siegel. In the book: Weight-
lessness. Physical Phenomena and Biological Effects.
Moscow, Mir Press, 1964.
13. Siegel, R., and E. C. Keshösk. AIChE, J., Vol. 10, No. 4,
1964, p. 509.
14. Kirichenko, Yu. A., and A. I. Charkin. Reprint of a
paper presented at Fourth International Heat Transfer
Conference. Versailles, September, 1970.
15. Kirichenko, Yu. A., A. I. Charkin, and M. L. Dolgoy. In
the book: Issledovaniya dinamiki parovykh puzyrey v
uslovayakh slabykh poley massovykh sil (materialy IV
vsesoyuznoy konferentsii po teploobmenu i gidravlicheskomu
soprotivleniyu [Dynamics of Vapor Bubbles in Weak Mass
Force Fields (Fourth All-Union Conference on Heat Transfer
and Hydraulic Resistance)]. Leningrad, 1971.
16. Han Chi-Yeh, and P. Griffith. Techn. Rept. 19, Div.
Sponsored Res., Mass Institute Technology, Cambridge.
February, 1962.
17. Ruckenstein, E. Bul. Inst. Politech. Bucuresti, Vol. 33,
1966, p. 79.

18. Roll, J. B., and J. E. Myers. AICHE J., Vol. 10, No. 1, 1964, p. 530.
19. Labuntsov, D. A., and V. V. Yagov. In the Book: Eksperimental'noye issledovaniye kipeniya zhidkostey v usloviyakh svobodnogo dvizheniya pri ponizhennykh davleniyakh (materialy IV Vsesoyuznoy konferentsii po teploobmenu i gidravlicheskomu soprotivleniyu) [Experimental Study of Liquid Boiling in Free Flow at Low Pressures (Fourth All-Union Conference on Heat Transfer and Hydraulic Resistance)]. Leningrad, 1971.
20. Saddy. Ph. D. Thesis of the University of London. February, 1970.
21. Prisnyakov, V. F. PMTF (Applied Mechanics and Technical Physics), Vol. 5, 1970.
22. Strengé, P. H., A. Orell, and J. W. Westwater. In the book: Physics of Boiling, Moscow, Mir Press, 1964.
23. Danilova, G. N. Teploobmen pri kipenii freonov (Heat Transfer during Freon Boiling). (Author's summary of doctoral dissertation, Leningrad Technological Institute of the Refrigeration Industry). Leningrad, 1968.
24. Foster, G., and N. Zuber. In the book: Physics of Boiling. Moscow, Mir Press, 1964.
25. Plesset, M. S., and S. A. Zwick. In the book: Physics of Boiling. Moscow, Mir Press, 1964.
26. Labuntsov, D. A., et al. TVT (High Temperature Engineering). Vol. 2, No. 3, 1964.
27. Kupferberg, A., and G. J. Jameson. Trans. Instn. Chem. Engrs., Vo. 47, No. 7, 1969, T241.
28. Lamb, H. Hydrodynamics. Moscow-Leningrad, Gostekhnizdat Press, 1947.
29. Han, C. Y., and P. Griffith. IJHMT, Vol. 8, 1965, p. 887.
30. Mamontova, N. N. PMTF, Vol. 3, 1963.
31. Winter, Ye. R., A. K. Wong, and P. McFadden. In the book: Heat and Mass Transfer. Minsk, Nauka i tekhnika Press, Vol. 9, 1968.

32. McFadden, P., and P. Grassman. In the book: Physics of Boiling. Moscow, Mir Press, 1964.
33. Borishanskiy, V. M., A. P. Kozyrev, and S. A. Svetlova. In the book: Konvektivnaya teploperedacha v dvukhfaznom i odnofaznom potokakh (Convective Heat Transfer in Two-Phase and Single-Phase Flows). Moscow-Leningrad, Energiya Press, 1964.
34. Katto, P. IFZh, Vol. 7, No. 12, 1964.
35. Lyon, D. W., P. G. Kosky, and B. N. Harman. Adv. in Cryog. Engng., Vol. 9, 1964, p. 77.
36. Siegel, R. In the book: Advances in Heat Transfer. Moscow, Mir Press, 1970.
37. Kirichenko, Yu. A., et al. IFZh, Vol. 17, No. 2, 1969.
38. Sherley, J. E. Advances in Cryogenic Engineering. K. D. Timmerhaus, editor. Vol. 8. New York, Plenum., 1963, p. 495.
39. Merte, H., Jr., and J. A. Clark. J. Heat Transfer, Vol. 86, 1964, p. 351.
40. Clodfelter, R. G. Low-Gravity Pool Boiling Heat Transfer. APL-TDR-64-19 (DDC NAD-437803), 1964.
41. Siegel, R., and E. G. Kenshock. NASA TR-R-216, February, 1965.
42. Pappel, S. S., and O. C. Faber, Jr. NASA TND-3288, February 1966.
43. Kirichenko, Yu. A., and M. L. Dolgoy. TVT, Vol. 8, No. 1, 1970.
44. Kirichenko, Yu. A., V. V. Tsybul'skiy, and A. V. Kostromeyev. IFZh, Vol. 21, No. 2, 1971.
45. Ivanov, M. S., and N. K. Yelukhin. Kislород (Oxygen). Vol. 3, 1958.
46. Malkov, M. P., et al. In the book: Soobshcheniya mezhdunarodnoy konferentsii po mirnomu ispol'zovaniyu atomnoy energii (Reports of All-Union Conference on Peaceful Use of Atomic Energy). Second edition, Vol. 4, No. 17, 1958.

47. Tsybul'skiy, V. V., and Yu. A. Kirichenko. IFZh (in press).
48. Borishanskiy, V. M. Energomashinostroyeniye (Power Machinery Construction), Vol. 7, 1958.
49. Karagounis, A. Bull. Inst. Intern. Froid. Annexe-2, 1956, p. 195.
50. Lyon, D. V. Adv. in Cryog. Eng., Vol. 10, 1965, p. 371.
51. Ratiani, G. V., and D. I. Aviliani. Kholodil'naya tekhnika, Vol. 3, 1965.
52. Cichelly, M., and G. Bonilla. Trans. AIChE., Vol. 6, 1945.

N74-28017

RADIATIVE COOLING OF BODIES OF ARBITRARY SHAPE
AND VARIABLE VOLUME IN VACUUM

V. S. Novikov and V. L. Chumakov

On the basis of joint application of the Tolubinskii integral method and the perturbation method we construct the asymptotic unsteady temperature distribution for a region of arbitrary shape on the moving boundary of which there are located nonlinear heat sinks (sources), describing radiative cooling in a medium with zero temperature (in a vacuum).

An integral method for solving linear phenomenological transport problems on the basis of construction of the fundamental function (Green's function) was proposed in [6, 7]. The Green's function is assumed to be known for an infinite space and the superposition principle is postulated. The results presented in the cited studies are valid for a region of arbitrary shape and either constant or variable volume. /82

Using as an example the third boundary value problem of heat transport under vacuum conditions, we shall show the possibility of joint application of the Tolubinskiy integral method and the perturbation method for solving nonlinear heat conduction problems for bodies of arbitrary shape with moving boundary.

Let D be a convex region with uniform and isotropic medium with boundary moving in accordance with an arbitrary law $S(t)$, on which the Stefan heat transfer law is specified

$$q = \sigma_a T_{bo}^4 \quad (1)$$

where σ_a is the coefficient of heat transfer by radiation, T_{bo} is the temperature at the boundary of the body.

In the region D there is specified an initial temperature distribution $T(P, t)/_{t=0} = f(P)$ and a source distribution with intensity $F(P, t)$. We are required to determine the temperature field at point P at the instant of time t.

Specification of the boundary thermal flux q_s in accordance with the radiative cooling law [by virtue of nonlinearity of (1)], makes the unsteady heat transport problem essentially nonlinear, which hinders significantly analytic study of the radiative cooling process. Only approximate analytic methods for solving the radiative cooling problem for bodies of simple form and constant volume are available.

In order to construct the asymptotic unsteady temperature distribution, we use the perturbation method, whose application to problems with essential external nonlinearities in the boundary conditions has been described in [3, 4]. The basis of the application of this method is the assumption on smallness of the disturbing function, considered as the difference between the specified nonlinear heat flux at the boundary and its linear approximation. The solution of the linearized problem is taken as the zero approximation. In the refining recurrent system of monotypic linear boundary value problems, the linear flux disturbance is considered the analog of the variable media temperatures.

In order to approximate the nonlinear flux (1) by a linear relation, we can use, for example, integral linearization [11], for which the condition of minimum of the sum of the deviations of the approximating straight line from the specified curve in the temperature variation range ($T_{bo}^{(2)} \leq T_{bo} \leq T_{bo}^{(1)}$) is minimized

$$\left| \int_{T^{(2)}}^{T^*} [T^4 - (a + bT)] dT \right| + \left| \int_{T^*}^{T^{(2)}} [T^4 - (a + bT)] dT \right| = \min.$$

Here T^* is an intermediate point lying between $T^{(2)}$, at which $T^4|_{T=T^{(2)}} = a + bT|_{T=T^{(2)}}$, and the point $T^{(1)}$ and is defined by the expression

$$T^* = \frac{(\sqrt{2}-1)T^{(2)} + T^{(1)}}{\sqrt{2}}. \quad (2)$$

The approximating straight line $a + bT$ with coefficients

/83

$$\begin{aligned} a &= -T^{(2)2}T^* (T^{*2} + T^*T^{(2)} + T^{(2)2}); \\ b &= -T^{*3} + T^{(2)2}T^* + T^*T^{(2)2} + T^{(2)3} \end{aligned} \quad (3)$$

cross the T^4 curve at two points: $T^{(2)}$ and T^* . Introducing the perturbation parameter ϵ ($0 \leq \epsilon \leq 1$), we rewrite the boundary condition (1) in the form

$$q = b\sigma_a \left[\frac{a}{b} + \epsilon\Phi + T_{bo} \right] \quad (4)$$

where the perturbation

$$\epsilon\Phi = \epsilon \left[\frac{T_{bo}^4}{b} - \left(\frac{a}{b} + T_{bo} \right) \right] \quad (5)$$

on the temperature variation segment ($T_{bo}^{(2)} - T_{bo}^{(1)}$) is assumed to be small in comparison with the quantity a/b . For $\epsilon = 1$, the condition (4) is identical to the original nonlinear condition (1), while for $\epsilon = 0$, it is linear and corresponds to the heat

transport problem solution in the zero approximation $T_0(p, t)$. In accordance with the usual procedure of the perturbation method, the solution of the third boundary value problem is sought in asymptotic expansion form [5]

$$T(P, t; \varepsilon) = T_0(P, t) + \sum_{m=1}^{\infty} \varepsilon^m T_m(P, t). \quad (6)$$

We find the corrections $T_m(P, t)$, ($m = 1, 2, \dots$) to the zero approximation as the solutions of the corresponding system of boundary value problems sequentially on the basis of the integral method [6]. In the boundary value problem for T_m , the initial conditions become uniform, the source functions are equal to zero, and we take as the media temperatures the expressions

$$\begin{aligned} T_{1\text{amb}}(M, t) &= \Phi(T_{\text{bo}}|_{\varepsilon=0}, T_{\text{bo}}) \\ &\dots\dots\dots \\ T_{m\text{amb}}(M, t) &= \frac{1}{(m-1)!} \left(\frac{\partial^{m-1} \Phi}{\partial \varepsilon^{m-1}} \right) \bigg|_{\varepsilon=0} T_{\text{bo}} \end{aligned} \quad (7)$$

The integral equations for the fluxes ($m = 0, 1, 2, \dots$) are written in the form

$$\begin{aligned} q_0(M, t) &= b\sigma_{\text{ab}} \int_0^t d\tau \int_{S(\tau)} q_0(N, \tau) G(N, M, t-\tau) dN + b\sigma_{\text{ab}} T_0 + a\sigma_{\text{a}} \\ &\dots\dots\dots \\ q_m(M, t) &= b\sigma_{\text{ab}} \int_0^t d\tau \int_{S(\tau)} q_m(N, \tau) G(N, M, t-\tau) dN + b\sigma_{\text{ab}} T_m(M, t). \end{aligned} \quad (8)$$

Here $M[r_0(\theta, \varphi, t), \theta, \varphi] \in S(t)$; $N[r_0(\theta, \varphi, t), \theta, \varphi] \in S(t)$; $r_0 = \rho -$ is the surface motion law; ρ, θ, φ are spherical coordinates; the Green's function $G(N, M, t, \tau)$ for the variable-volume body is assumed to be known, the technique for constructing the fundamental function on the basis of the reflection principle was suggested in [6]

$$\psi_0 = k \int_D \int_{(0)} f(Q) G(Q, M, t, 0) dQ + \int_0^t d\tau \int_{D(\tau)} F(Q, \tau) G(Q, M, t - \tau) dQ, \quad Q \in D, \quad (9)$$

where $k = c\gamma$, c is the specific heat, γ is the density. If we examine a transport process described by a hyperbolic equation, /84
we must add in the right side of (9) the term [6]

$$\frac{1}{c^2} \int_D \int_{(0)} \left[\left. \frac{\partial T(Q, t)}{\partial t} \right|_{t=0} G(Q, P, t) + f(Q) \frac{\partial G(Q, P, t)}{\partial t} \right] dQ,$$

where c is the heat transport rate. Considering that $G \geq 0$ everywhere in D , we show that, for the instant t from the interval $0 \leq t \leq t_0$, where t_0 is found from the condition

$$\max_0 \int_0^{t_0} d\tau \int_{S(\tau)} G(N, M, t_0 - \tau) dN = \frac{1}{b\sigma_a}, \quad (10)$$

the series of sequential approximations for the expression q_m ($m = 0, 1, \dots$) as results of solution of the integral equations (8) and the series formed from the sequence q_0, q_1, q_2, \dots converge absolutely and uniformly. The proof of convergence for the series

$$q_m = \varphi_m + \varphi_{m_1} + \varphi_{m_2} + \dots + \varphi_{m_n} + \dots \quad (m = 0, 1, \dots) \quad (11)$$

is analogous to that presented in [1].

The following estimates hold

$$|\varphi_m| = |b\sigma_a T_{mamb}| \leq |a\sigma_a| \leq A_1 < \infty, \quad m = 1, 2, \dots$$

since by assumption

$$\left| \frac{b\Phi(T_{-})}{a} \right| < 1; \quad |\varphi_{m_1}| \leq b\sigma_a \int_0^t d\tau \int_{S(\tau)} |\varphi_0| G dS(\tau) < A_1 b_1 \quad (m = 1, 2, \dots)$$

where

$$b_1 = b\sigma_a \max_{\tau \in [0, t_0]} \int_0^t \int_{S(\tau)} G(N, M, t - \tau) dN < 1.$$

Sequential application of these estimates leads to a geometric progression with denominator $b_1 < 1$ which is the majorant for the series $\sum |q_m|$. This proves absolute and uniform convergence of the functional series (11) for q_m $m = 1, 2, \dots$) and similarly for q_0 .

We shall try to show convergence of the series formed from q_m ($m = 0, 1$). As a consequence of the sign-alternating nature of the function $T_m(M, t)$, it is necessary to study the functional series

$$|q_0| + |q_1| + \dots + |q_m| + \dots$$

For convenience, we approximate the complex $\Phi(T_{bo})$ by the linear relation $P(T_{bo}) = A + BT_{bo}$, so that

$$|\Phi(T_{bo})| \leq |A + BT_{bo}| = P_{amb} \quad (12)$$

Then, with account for (7), the estimates are valid

$$\left. \begin{aligned} |a\sigma_a| &\leq A_1; \\ |b\sigma_a P_1| &\leq A + B \frac{A_1}{b\sigma_a}; \\ |b\sigma_a P_2| &\leq AB + B^2 \frac{A_1}{b\sigma_a}; \\ &\dots \dots \dots \\ |b\sigma_a P_m| &\leq AB^{m-1} + B^m \frac{A_1}{b\sigma_a} \quad (m = 1, 2, \dots) \end{aligned} \right\} \quad (13)$$

For $B < 1$, the series $b\sigma_a \sum_{m=0}^{\infty} |P_m(M, t)|$ converges absolutely and uniformly, since A_1 is independent of t in the interval $0 \leq t \leq t_0$.

By virtue of the condition (12), this series is the majorant of /85

the series $b\sigma_a \sum_{m=0}^{\infty} |T_{amb}(M, t)|$ and, consequently, the latter series converges absolutely and uniformly in the region (M, t) . Returning to the estimates for the series $q_m = \sum_i \varphi_{m_i} (m = 0, 1, \dots)$, we conclude that the series $q_0 + q_1 + \dots + q_m + \dots$ also converges absolutely and uniformly, since, with account for the estimates (13), absolute and uniform convergence of the series $\sum_{m=0}^{\infty} \varphi_{m_i}$ ($i = 0, 1, \dots$) holds. The expressions (8) for the fluxes with account for the conditions (12) can be obtained from the following relation

$$\tilde{q}(M, t) = b\sigma_a L\tilde{q} + b\sigma_a [a/b + \varepsilon P(T_{bo})] + b\sigma_a \psi_0 \quad (14)$$

where L is an operator on the function q . Taking $E_q = q$, where E is the unit operator, we write (14) in the form

$$(E - b\sigma_a L)\tilde{q} = b\sigma_a [a/b + \varepsilon P(T_{bo})] + b\sigma_a \psi_0 \quad (15)$$

Expanding (15) into a series in powers of ε , we obtain the equality

$$\tilde{q} = (E - b\sigma_a L)^{-1} \{ b\sigma_a [a/b + \varepsilon(A + BT_0) + \varepsilon^2 BT_1 + \dots + \varepsilon^m BT_{m-1} + \dots] + b\sigma_a \psi_0 \}, \quad (16)$$

where $(E - \sigma_a bL)^{-1}$ is the inverse of the operator $(E - b\sigma_a L)$.

The terms of the series in the right side of (16), as follows from the estimates (13), will be smaller in absolute magnitude than the terms of a converging series with positive terms

$$(E - a\sigma_a L)^{-1} \left\{ \left[A_1 + \sum_{m=1}^{\infty} |\varepsilon^m| AB^{m-1} + B^m \frac{A_1}{a\sigma_a} \right] + b\sigma_a \psi_0 \right\}.$$

Consequently, for fixed ε satisfying the condition $|\varepsilon| < 1/B'$, the series (16) converges uniformly and (16) defines the asymptotic expression for the function \tilde{q} .

Since the sought temperature as a limiting function of the sum of a uniformly converging series of continuous functions q_m on the set (m, t) is also continuous [2], for the required value of the parameter $\varepsilon = 1$ and satisfaction of the condition $B < 1$, we obtain the sought asymptotic temperature distribution in the form of the expression

$$T(P, t) = \sum_{m=0}^{\infty} \int_0^t d\tau \int_{S(\tau)} q_m(M, \tau) G(M, P, t - \tau) dM + \\ + k \int_0^t \int_{D(\tau)} f(Q) G(Q, P, t) dQ + \int_0^t d\tau \int_{D(\tau)} F(Q, \tau) G(Q, P, t - \tau) dQ,$$

since the superposition principle is valid for each of the q_m calculation problems, and on the basis of the Weierstrass theorem on uniformly converging series [2], we can state that (17) is the limiting value of the temperature as the integral of a definite value of the thermal flux.

The subject problem is of interest for calculating and designing thermal protection for space vehicles of arbitrary geometric shape, since radiative cooling under space conditions may be considered nonlinear thermal sinks on the vehicle surface. Moreover, on the basis of the proposed synthesis of the integral method and the perturbation method, even more complex problems can be solved, for example, problems with account for temperature dependence of the thermophysical characteristics and nonlinear heat transport problems encountered in space investigations.

REFERENCES

1. Akhmediyev, V. M. *Izv. vusov., priborostroyeniye*, Vol. 1, 1971.
2. Hurwitz, A., and R. Courant. *Theory of Functions*, Moscow, Nauka Press, 1968.

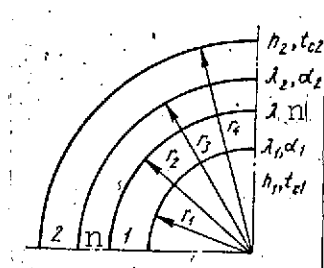
3. Kozdova, L. A., and V. L. Chumakov. In the book: Problema teplo- i massoperenosa (Heat and Mass Transfer). Moscow, Energiya Press, 1970.
4. Kozdova, L. A., and V. L. Chumakov. TVT, Vol. 8, No. 5, 1970.
5. Mitropol'skiy, Yu. A., and B. I. Moseyenko. Lektsii po primeneniyu asimptoticheskikh metodov k resheniyu uravneniy v chastnykh proizvodnykh (Lectures on Application of Asymptotic Methods to the Solution of Partial Differential Equations). Kiev, Press of the Institute of Mathematics, 1968.
6. Tolubinskiy, Ye. V. DAN SSSR, Vol. 160, No. 6, 1965.
7. Tolubinskiy, Ye. V. Teoriya protsessov perenosa (Theory of Transport Processes). Kiev, Naukova Dumka Press, 1969.

NONLINEAR UNSTEADY CONTACT HEAT CONDUCTION OF TWO-LAYER SHELLS
IN THE PRESENCE OF THERMAL RADIATION

V. S. Novikov and V. L. Chumakov

A technique is proposed for calculating the complex heat transfer of mated shells with the surrounding medium which also takes into account the temperature dependence of the contact thermal resistance between the shells. This technique can be used for thermal calculations and for calculations of the temperature stresses in two-layer space structure shells.

Two-layer structures find wide application in modern power /86 generation, space, and aircraft technology. The processes of heating and cooling of such structures with thermal stresses are very complex; therefore, it is usually necessary to introduce simplifying assumptions on the nature of the heat transfer between the individual layers and also between the structure and the surrounding medium in order to linearize the thermoelastic problems when calculating the stresses. For example, in [1], the layer contact thermal resistance is considered constant in calculating the temperatures and unsteady thermal stresses. However, it is well known that the contact thermal resistance depends significantly on the external load and may decrease by an order of magnitude with increase of the latter [2 — 4]. Using the results of [5], we propose a more general approach to the problem of temperature calculation in contacting layers. This approach makes it possible not only to account for variability of the quantity R_n in the process of heating or cooling of a



Schematic of junction of shells with intermediate connecting layer.

two-layer structure but also makes it possible to examine the high temperature case, when thermal radiation plays a significant role in heat transfer between a two-layer structure and the external medium.

We shall examine the unsteady heat conduction problem for two-layer cylindrical (spherical) shells with an intermediate layer which, as in [1], has zero thermal capacity. When the shells are heated (cooled), the magnitude of the contact pressure between them changes in the general case because of the difference between the shell coefficients of linear expansion and temperatures. As a consequence of this, the contact pressure at the shell interface and also the thermal resistance R_n of the intermediate layer are variable. The contact pressure can be expressed in the usual way in terms of the temperatures on the contacting surfaces and then, using the results of [3, 4], we can find the nonlinear dependence of R_n on these temperatures.

The unsteady heat conduction processes in the outside layers 1 and 2 (see figure) are described by the differential equations

$$\frac{\partial t_j(r, \tau)}{\partial \tau} = a_j r^{-k} \frac{\partial}{\partial r} \left[r^k \frac{\partial t_j(r, \tau)}{\partial r} \right], \quad r_1 < r < r_2, \quad 0 < \tau < \infty; \quad r_3 < r < r_4, \quad (1)$$

where $j = 1, 2$ is the layer index; a_j are the thermal conductivities, τ is time. For $k = 1, 2$, the equations (1) describe the symmetric temperature field, respectively, in a three-layer hollow infinite cylinder and hollow sphere. We consider the following conditions at the layer boundary and interfaces

$$-\lambda_1 \frac{\partial t_1(r_1, \tau)}{\partial r} = h_1 [t_{C_1}(\tau) - t_1(r_1, \tau)], \quad (2)$$

$$-2\pi r_2 \lambda_2 \frac{\partial t_1(r_2, \tau)}{\partial r} = \frac{t_1(r_2, \tau) - t_2(r_3, \tau)}{R_n}, \quad (3)$$

$$\lambda_1 r_2 \frac{\partial t_1(r_2, \tau)}{\partial r} = \lambda_2 r_3 \frac{\partial t_2(r_3, \tau)}{\partial r}, \quad (4)$$

$$\lambda_2 \frac{\partial t_2(r_4, \tau)}{\partial r} = h_2 [t_{C_2}(\tau) - t_2(r_4, \tau)], \quad (5)$$

$$t_1(r, 0) = t_2(r, 0) = t_0, \quad (6)$$

where the thermal resistance of the contact (intermediate) layer, having zero thermal capacity as in [1], is, in the general case, a function of t_1 and t_2 , i.e.,

$$R_n = R_n[t_1(r_2, \tau), t_2(r_3, \tau)]. \quad (7)$$

Because of the nonlinear relation (7), the condition (3) becomes nonlinear, which makes the entire heat conduction problem nonlinear. We can use the successive approximation method for its solution. We first separate in (7) the constant part and the part depending on t_1 and t_2 as follows

$$R_n = \bar{R}_n + \varphi[t_1(r_2, \tau), t_2(r_3, \tau)], \quad (8)$$

where \bar{R}_n is the integral mean (with respect to temperatures t_1 and t_2) value of the expression (7).

In the iteration method, neglect of the function φ leads to the basic solution of the linear problem, known for the cylinder from [1]. In order to calculate in the first approximation the influence of the function φ , the basic solution is substituted into the boundary condition (2), in which R_n is defined by the expression (8) (in this case, R_n is a function of time) and then we again find the solution of the system of equations (1) — (6). We shall describe the application of the perturbation (small parameter) method, which is somewhat more general in comparison with the iteration method. If the R_n variation law in (7) depends significantly on t_j , representation of R_n in the form of the expression (8), in which the φ approximation error is considered the perturbing function, makes it possible to reduce the nonlinear problem to one with unessential nonlinearity.

We introduce the parameter ω into (8) in the form of a multiplier of the function φ and represent the sought temperatures t_j in the form of series in powers of ω

$$t_j(r, \tau, \omega) = \sum_{m=0}^{\infty} \omega^m t_j^{(m)}(r, \tau), \quad j = 1, 2, \quad (9)$$

where the functions $t_j^{(m)}$ are to be determined. We substitute (9) into (1) — (6) and consider the representation (8). Since these equations are valid for any m , after some transformations, we obtain the system of boundary value problems for the bodies in question, in which, for the zero approximation $t_j^{(0)}$, the equations are identical to (1) — (6). Their solution in the multilayer cylinder case is the solution presented in [11] for $R_n = \bar{R}_n$.

The system of boundary value problems for finding the corrections $t_j^{(m)}$ to the m^{th} approximations m ($m = 1, 2, \dots$), is written in the following form

$$\frac{\partial t_j^{(m)}(r, \tau)}{\partial \tau} = a_j r^{-k} \frac{\partial}{\partial r} \left[r^k \frac{\partial t_j^{(m)}(r, \tau)}{\partial r} \right] \quad (j = 1, 2; \quad k = 1, 2); \quad (10)$$

88

$$\frac{\partial t_1^{(m)}(r, \tau)}{\partial r} = h_1 t_1^{(m)}(r_1, \tau); \quad (11)$$

$$-2\pi r_2 \lambda_2 \Phi_m = t_1^{(m)}(r_2, \tau) - t_2^{(m)}(r_2, \tau); \quad (12)$$

$$\lambda_1 r_2 \frac{\partial t_1^{(m)}(r_2, \tau)}{\partial r} = \lambda_2 r_2 \frac{\partial t_2^{(m)}(r_2, \tau)}{\partial r}; \quad (13)$$

$$\lambda_2 \frac{\partial t_2^{(m)}(r_4, \tau)}{\partial r} + h_2 t_2^{(m)}(r_4, \tau) = 0; \quad (14)$$

$$t_1^{(m)}(r, 0) = t_2^{(m)}(r, 0) = 0; \quad (15)$$

where

$$\Phi_m \left(\frac{\partial t_1^{(0)}}{\partial r}, \frac{\partial t_1^{(1)}}{\partial r}, \dots, \frac{\partial t_1^{(m-1)}}{\partial r}, t_1^{(0)}, \dots, t_1^{(m-1)} \right) = \frac{1}{(m-1)!} \times \\ \times \left(\frac{\partial^{m-1}}{\partial \omega^{m-1}} \left[\frac{\partial t_1}{\partial r} R_n \right] \right) \Big|_{\omega=0}^{t_1=t_1^{(0)}} \quad (16)$$

In those cases when $R_n \approx \bar{R}_n$, it is sufficient to consider only the first corrections $t_j^{(1)}$ to $t_j^{(0)}, j = 1, 2$. Then the condition (12) takes the form

$$-2\pi r_2 \lambda_2 \left\{ \frac{\partial t_1^{(0)}(r_2, \tau)}{\partial r} \Phi(t_j^{(0)}) + \frac{\partial t_1^{(1)}(r_2, \tau)}{\partial r} \bar{R}_n \right\} = t_1^{(1)}(r_2, \tau) - t_2^{(1)}(r_2, \tau); \quad (17)$$

where the term

$$\frac{\partial t_1^{(0)}(r_2, \tau)}{\partial r} \varphi(t_j^{(0)}), \quad j = 1, 2,$$

as a function of time is known from the basic solution $t_j^{(0)}$.

For solution of the monotopic sequence of boundary value problems (10) — (15), we can use the highly developed mathematical apparatus for solution of linear problems (for example, the operator method used in [1]).

Since for $\omega = 1$, (8) reproduces the relation (7) exactly, the final values of the temperature t_j ($j = 1, 2$) are obtained from the representation (9), taken for $\omega = 1$.

In order to determine the unsteady thermoelastic stresses which arise in the layers of the system, we use the results presented in [1], where the temperature is substituted in the form of the sum (9) with the first few terms.

The subject problem (1) — (6) can be extended to the case of high temperature levels such that radiative heat transfer begins to play a significant role. Then, in place of the linear conditions (2) and (5), we consider the nonlinear conditions

$$-\lambda_1 \frac{\partial t_1(r_1, \tau)}{\partial r} = h_1 [t_{c1} t_1(r_1, \tau)] + \sigma_{a1} [t_{c1}^4 - t_1^4(r_1, \tau)], \quad (18)$$

$$\lambda_2 \frac{\partial t_2(r_2, \tau)}{\partial r} = h_2 [t_{c2} - t_2(r_2, \tau)] + \sigma_{a2} [t_{c2}^4 - t_2^4(r_2, \tau)]. \quad (19)$$

The presence in conditions (18) and (19) of the difference of the fourth powers of the ambient and sought temperatures makes them very nonlinear. The use here of the exact analytic calculation methods is ineffective, since these methods are limited to the basic class of linear problems. This makes it necessary to develop adequately strong approximate methods.

In order to solve the problem with the conditions (18) and (19) (in the general formulation), we first linearize these conditions so that the neglected nonlinearities in the basic solution are small or, in other words, so that the linearized (unperturbed) solution, which plays the role of the basic solution, describes sufficiently well the true solution of the system. In this case, we can also use the perturbation method, /89 introducing the linearizing parameter q . To this end, we write the conditions (18) and (19) in the form

$$-\lambda_j \frac{\partial t_j(r_{1,4}, \tau)}{\partial r} = H_j [t_{c_j} + \omega \psi_j - t_j(r_{1,4}, \tau)], \quad j = 1, 2, \quad (20)$$

where

$$\begin{aligned} H_j &= \sigma_{aj} (p + t_{c_j}^3 + q_j); \quad p = \frac{h_j}{\sigma_{aj}}; \\ \psi_j &= \frac{\sigma_{aj} [t_{c_j}^3 t_j - t_j^4 - q_j (t_{c_j} - t_j)]}{H_j}; \\ q_j &= \frac{1}{t_{c_j} - t_0} \int_{t_0}^{t_{c_j}} (t_{c_j}^2 t + t_{c_j} t^2 + t^3) dt. \end{aligned}$$

Here the disturbance $\omega \psi_j$ with the disturbance parameter ω is small in comparison with t_{c_j} , which permits obtaining step-by-step an exact or at least approximate solution of the problem with perturbed boundary conditions (20).

The functions $\Psi_{j(m)} (m = 1, 2, \dots)$ are considered variable ambient temperatures and are found from the expression

$$\Psi_{j(m)} = \frac{1}{(m-1)!} \left(\frac{\partial^{m-1} \Psi(\omega)}{\partial \omega^{m-1}} \right) \Big|_{\omega=0}^{t_j=t_j^{(0)}}. \quad (21)$$

For $\omega = 0$, it is sufficient in practice to use only the first approximation. The function

$$\Psi_{j(1)} = \frac{t_{c_j}^3 t_j^{(0)} - t_j^{(0)4} - q_j (t_{c_j} - t_j^{(0)})}{p + t_{c_j}^3 + q_j} \quad (22)$$

is approximated well by an exponential relation, for which we can use the solution of [1].

The larger the convective heat transfer transport fraction in the overall heat exchange ($p > 0$), the smaller the contribution to the basic solution of account for nonlinearities in the boundary conditions of the subsequent approximations.

With introduction of the perturbation parameter ω as a multiplier of the nonlinear complexes Ψ_j and φ , we actually adopted an approach reminiscent of the "comparison" technique, which is used to solve ordinary differential equations [6] and to solve nonlinear oscillatory systems [7]. We used, as the simple comparison boundary value problem, the problem with $\omega = 0$, which has a known solution differing only slightly for small ω from the sought solution of the nonlinear problem. Preliminary linearization of the boundary conditions was necessary in order to reduce the influence of the initial nonlinearity on the problem solution, since we were interested in the final solution of the nonlinear problem corresponding to the parameter ω equal to unity. When seeking the solution in series form (9), the quantity ω is necessary only in order to know which coefficients must be compared with one another. When solving the recurrent system of equations (11) — (15) with the boundary conditions (20) relating $t_j^{(m)}, j = 1, 2$, it may be found that for certain φ dependences, the series (9) will converge only for $\omega < 1$. In this case, using the analytic continuation methods, we can convert from values of $\omega < 1$ to the value $\omega = 1$ (for example, by re-expansion of the series in terms of ω [8]). The accuracy of the solutions obtained can be evaluated by studying the solutions themselves.

REFERENCES

1. Pereversev, D. A. In the book: Teplovym napryazheniyama v elementakh konstruktsiy (Thermal Stresses in Structural Elements). Vol. 7. Kiev, Naukova Dumka Press, 1967.
2. Shlykov, Yu. P., and E. A. Ganin. Kontaktniy teploobmen /90 (Contact Heat Transfer). Moscow-Leningrad, Gosenergoizdat Press, 1963.
3. Novikov, V. S. IFZh, Vol. 19, No. 1, 1970.
4. Novikov, V. S. IFZh, Vol. 19, No. 2, 1970.
5. Novikov, V. S., and V. L. Chumakov. In the book: Nauchnoye soveshchaniye po teplovym napryazheniyam v elementakh konstruktsiy (Scientific Conference on Thermal Stresses in Structural Elements). Summaries of reports, Kiev, Naukova Dumka Press, 1970.
6. Vazov, V. Asimptoticheskiye razlozheniya resheniy obyknovennykh differentsial'nykh uravnenii (Asymptotic Expansions of Solutions of Ordinary Differential Equations). Moscow, Mir Press, 1968.
7. Mitropol'skiy, Yu. A., and B. N. Moseyenko. Lektsii po primeneniyu asimptoticheskikh metodov k resheniyu uravneniy v chastnykh proizvodnykh (Lectures on Application of Asymptotic Methods to Solution of Partial Differential Equations). Kiev, Press of the Institute of Mathematics of the Academy of Sciences of the UkSSR, 1968.
8. Kantorovich, L. V., and V. P. Krylov, Priblizhennyye metody vysshego analiza (Applied Methods of Higher Analysis). Moscow-Leningrad, GIFML (State Publishing House of Physical and Mathematical Literature), 1962.

N74-28019

CALCULATION OF THE HYDRODYNAMIC AND HEAT TRANSFER PROCESSES
OCCURRING DURING FILLING, PRESSURIZING, AND
EMPTYING OF CRYOGENIC VESSELS

I. S. Zhitomirskiy and V. I. Pestryakov

A method is proposed for calculating the heat transfer and hydrodynamic processes taking place during pressurization and pressure transfer of cryogenic fluids and filling of vessels with these fluids. It is assumed that the liquid and gas flow in the vessel takes place with velocities considerably less than the speed of sound. The finite difference method is used to solve the governing system of nonlinear partial differential equations. Programs in ALGOL-60 language are developed which can be used to calculate these processes on a digital computer. The results of some calculations are presented in comparison with experimental data.

The development of technology and particularly space exploration has posed new problems for cryogenics. A large number of cryogenic liquids are required, the questions of storage and transportations of these liquids have become very important, as have the associated problems of vessel precooling and filling.

/90

One of the liquid transfer techniques is pressure transfer. This technique involves creating a differential pressure in the gas cushion in the vessel above the liquid, which permits overcoming the hydraulic resistance of the system of connecting lines

and forcing the liquid from one vessel into another. When storing a liquid pressurization is often required, i.e., it is necessary to increase the pressure in the vessel and maintain this pressure at a definite level. Filling of vessels with liquid is also a quite complex problem, since the vessel wall temperature at the initial moment is much higher than the boiling point of the liquid, which leads to considerable intensification of the heat transfer processes inside the vessel.

There is a single common characteristic feature of all these processes. This is the fact that it is necessary to deal with a symmetric gaseous volume, variable in time, bounded by the walls on the sides and by a horizontal plane below — the liquid surface. Gas is either fed into this volume or removed from it and this gas, during its motion, interacts with the walls, giving up heat to the walls or taking heat from the walls. The gas inflow and outflow is accomplished differently in each of the processes.

In the pressure transport (or pressurization) case, the gas enters the vessel at the top from external systems. Evaporation or condensation may take place at the liquid surface and, depending on this, gas must be either supplied to or removed from the space in order to maintain the specified pressure variation regime. In addition, the gas may condense on the cold walls of the vessel and thus be removed from the space. During filling of the vessel with liquid, gas enters the gas space from below from the direction of the liquid surface as a result of boiling and is discharged through the vent system.

In designing liquid transporting and storing systems, it is very important to be able to predict in advance what amount of gas is necessary to carry out the pressurization or pressure transfer process while providing the specified pressure regime in

the vessel: what is the optimal temperature of the incoming gas; what are the temperature gradients and consequently the stresses which arise in the walls of vessels being emptied or filled with cryogenic liquid for a given process rate; is a /91
given filling rate possible for a given venting system handling capacity; what are the liquid losses in evaporation during filling and what time is necessary for filling the vessels; what amount of gas is required for precooling of the vessel prior to filling and how efficient is the particular filling procedure. In order to answer these questions, it is necessary to be able to calculate the heat transfer and hydrodynamics processes taking place in the vessels.

Many experimental and theoretical investigations have been made to study the above-mentioned processes. On the basis of experimental studies (see, for example, the survey of Clark [1]), we can draw the following conclusions:

1. The heat transfer from the gas to the vessel walls is described quite well by the natural convection laws. Some intensification of the heat transfer process takes place in the inlet diffuser region in the upper part of the vessel during pressurization and pressure transfer and in the interface region during filling of the vessel with the liquid.

2. With accuracy adequate for calculations, the interface temperature is equal to the saturation temperature corresponding to the pressure in the vessel. For not too rapid pressure changes, the lag in the temperature change is small.

3. Both condensation and evaporation may take place at the gas-liquid interface. The intensity of these transformations increases when entering gas stream disturbs the interface, which leads to agitation of the surface layer of the liquid.

4. During emptying of the vessel, the wall segments being uncovered may have a temperature below the saturation temperature and in this case, gas condensation will take place on the walls.

5. During vessel filling, liquid boiling takes place in regimes corresponding to the entire boiling curve.

In the investigations, considerable attention was devoted to theoretical analysis of the pressure transfer and pressurization processes and the phenomena taking place at the interface [1]. Considerably fewer studies have been made of the vessel filling processes [2, 3, 6].

The present article is a continuation of the series of studies made at FTINT AS UkSSR [3, — 6]. In these studies, as in [11, 12], the gas and liquid temperature, velocity, and pressure and wall temperature are investigated within the framework of the one-dimensional model. A generalization is made of the previously obtained computational schemes and a more detailed examination is made of the questions associated with condensation on the wall and with determining the unsteady thermal influx to the wall through the insulation.

The one-dimensional treatment, in which for all the gas flow and bounding wall parameters we can consider the dependence only on a single space coordinate, which we denote by x ($0 \leq x \leq l$), and averaging is performed with respect to the remaining coordinates, is applicable to a greater or lesser degree in examining the described problems.

If, as a result of heat exchange with the walls, the gas temperature and density vary significantly along the flow, and if it is also necessary to take into account gas conductivity

and thermal and friction losses during gas flow, we must use the system of nonlinear mass, energy, and momentum conservation equations to determine the flow parameters as functions of time t and the coordinate x

$$F \frac{\partial \rho}{\partial t} = - \frac{\partial}{\partial x} (\rho u F) - J; \quad (1)$$

$$F \frac{\partial (\rho e)}{\partial t} = - \frac{\partial}{\partial x} \left[F u \rho \left(e + \frac{p}{\rho} \right) - F \lambda \frac{\partial T}{\partial x} \right] - J \left(e + \frac{p}{\rho} \right) + Q; \quad (2)$$

$$F \frac{\partial (\rho u)}{\partial t} = - \frac{\partial}{\partial x} (p + \rho u^2) - \xi \frac{\rho u |u|}{2d} - J \frac{u}{F}; \quad (3)$$

and the equations of state

92

$$\rho = \rho(p, T); \quad e = e(p, T). \quad (4)$$

Here F is the channel cross section area; ρ is the density of the gas; u is velocity; e is the specific internal energy of the gas; λ is the thermal conductivity of the gas; ξ is the hydraulic resistance coefficient; d is the hydraulic diameter,

Moreover, we need an additional relation determining the heat influx Q to the gas from the channel wall and the change of the mass flow rate J as a result of condensation on the wall, both referred to unit channel length. The system (1) — (4) is supplemented by the initial and boundary conditions

$$T(x, 0) = f(x); \quad p(x, 0) = \varphi(x); \quad u(x, 0) = \psi(x); \quad (5)$$

$$F_0 \left(T, \frac{\partial T}{\partial x}, p, u \right) \Big|_{x=0} = 0; \quad (6)$$

$$F_t \left(T, \frac{\partial T}{\partial x}, p, u \right) \Big|_{x=l} = 0; \quad | \quad (7)$$

$$\Phi_0(p, u, T) \Big|_{x=0} = 0; \quad | \quad (8)$$

$$\Phi_l(p, u, T) \Big|_{x=l} = 0. \quad | \quad (9)$$

In the general case, major difficulties arise in solving this system of equations, but in many cases, we can identify a considerable class of gas flows — "slow" flows — whose description and consequently, solution can be simplified significantly.

It can be shown [6] that, if the flow is characterized by velocities considerably less than the speed of sound ($M \ll 1$), and the accelerations in the flow are not large, the pressure change along the coordinate x in such flows can be neglected and we can consider the pressure p as a function of time only: $p = p(t)$. Since, in this case, the number of unknown functions which depend on the two variables (x, t) decreases by one, the system (1) — (9) becomes overdetermined.

The analysis performed in [6] made it possible to conclude that the equation of motion for low Mach numbers is nearly identically degenerate and may be excluded from consideration. The differential order with respect to the variable x for the remaining system of equations (1), (2), (4), makes it necessary to specify three boundary conditions. However, the presence of the unknown function $p(t)$ leads to the necessity for specifying still another constraint which is satisfied at every instant of time. The conditions (6) — (9) provide the required number of constraints for the considered problem formulation. However, if the function $p(t)$ is known (specifically, $p = \text{const}$), one of the

conditions (8) or (9) becomes superfluous. It should be noted that, in connection with exclusion of (3), the necessity for specifying the initial velocity distribution disappears.

If we examine gas flow in a channel with the walls of which the gas exchanges heat, the term Q in (2), describing convective heat exchange between the gas and the wall, has the form

$$Q = \alpha P (T_w - T), \quad (10)$$

where α is the coefficient of heat transfer from the gas to the wall; P is the channel cross section perimeter; T_w is the wall temperature; T is the gas temperature.

In this case, we must add to the system (1), (2), (4) the equation of energy conservation in an element of the wall.

If the temperature variation through the thickness of the wall can be neglected, this equation may be written in the form

$$\rho c F_w \frac{\partial T_w}{\partial t} = \frac{\partial}{\partial s} \left(\lambda F_w \frac{\partial T_w}{\partial s} \right) + \alpha P (T - T_w) + qP, \quad (11)$$

where q is the specific thermal flux to the outer surface of the wall element through the thermal insulation of the vessel; c is the specific heat of the wall material; F_w is the wall cross section area; s is the arc length of the vessel wall middle surface, measured along the meridian, /93

If the vessel has the form of a circular cylinder with vertical generator, the coordinate s coincides with the coordinate x . If the vessel is spherical, measuring s from the pole we have

$$x = R \left(1 - \cos \frac{s}{R} \right),$$

R is the radius of the sphere, $F_W = 2\pi r\sigma_W$, $F_{Wl} = 2\pi r\sigma_{Wl}$, $P = 2\pi r$; $r = \sqrt{2Rx - x^2}$ and (11) becomes

$$\rho c \delta_{Wl} \frac{\partial T_{Wl}}{\partial t} = -\frac{\delta_{Wl}}{R^2} \frac{\partial}{\partial x} \left(\lambda r^2 \frac{\partial T_{Wl}}{\partial x} \right) + \alpha (T - T_{Wl}) + q. \quad (12)$$

When introducing the equation (11), it is necessary to specify the initial condition

$$T_{Wl}(x, 0) = f_1(x) \quad (13)$$

and two boundary conditions which define the heat transfer at the ends of the wall

$$\varphi_0 \left(T_{Wl} \frac{\partial T_{Wl}}{\partial x}, T, q \right) \Big|_{x=0} = 0; \quad (14)$$

$$\varphi_L \left(T_{Wl} \frac{\partial T_{Wl}}{\partial x}, T, q \right) \Big|_{x=L} = 0. \quad (15)$$

For complete determinancy of the posed problem, we must know in (11) the magnitude of the heat influx through the insulation to the outer surface of the wall.

Let us examine some simplified computational models for cases of evacuated-powder and evacuated-multilayer insulation of a cryogenic vessel. In the case of the evacuated-powder insulation, which is an isotropic body, in view of the fact that the temperature gradient along the wall height is considerably less than the gradients through the insulation thickness, heat transfer in the insulation in the direction along the wall can be neglected.

We denote by y the coordinate directed across the insulation (Figure 1), so that $y = 0$ corresponds to the outer surface of the vessel wall and $y = l_1$ corresponds to the outer surface of

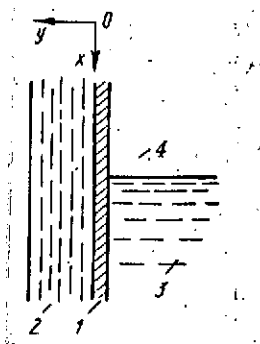


Figure 1. Computational scheme of insulation layer on cryogenic vessel.

1- wall; 2- thermal insulation; 3- liquid; 4- gas.

the insulation. Then we have, for the insulation temperature $T_i = T_i(x, y, t)$

$$c_i(T_i) \rho_i \frac{\partial T_i}{\partial t} = \frac{\partial}{\partial y} \left[\lambda_i(T_i) \frac{\partial T_i}{\partial y} \right], \quad (16)$$

the boundary conditions

$$\lambda_i \frac{\partial T_i}{\partial y} = \alpha (T_a - T_i) \text{ for } y = l_1 \quad (17)$$

$$T_i = T_w(x, t) \text{ for } y = 0 \quad (18)$$

and the initial condition

$$T_i = T_0(y) \text{ for } t = 0. \quad (19)$$

Here c_i , ρ_i , and λ_i are, respectively, the specific heat, density, and thermal conductivity of the insulation; T_a is the ambient temperature.

The boundary condition (18) contains the coordinate x as a parameter. Thus, in order to determine the heat influx to the vessel wall

$$q(x, t) = -\lambda_i \frac{\partial T_i}{\partial y} \Big|_{y=0} \quad (20)$$

it is necessary to solve the one-parameter set $(0 \leq x \leq l_1)$ of one-dimensional unsteady heat conduction problems (16) — (19).

Since the quantity $T_w(x, t)$ in the condition (18) is not known in advance, all these heat conduction problems must, strictly speaking, be solved together with the system (1), (2), /94

(4) — (15). However, for economy of both computer memory and computer time, it is advisable to utilize an approximate splitting of these problems. To this end, we first solve the problems (16) — (19), replacing the condition (18) by the condition

$$T_{-1} = T_b(t) \quad \text{for } y = 0, \quad (18')$$

where $T_b(t)$ is a specified family of time-dependent functions which depends on the parameter b .

The functions $T_b(t)$ are selected so that the nature of the functions $T_w(x, t)$, considered as functions of time for different fixed values of x , is reproduced as closely as possible.

For each value of the parameter b , we calculate the heat flux $q_b(t)$ using a formula analogous to (20). Excluding the parameters b and t from the relations $q = q_b(t)$, $T = T_b(t)$, $\frac{dT}{dt} = T'_b(t)$, we obtain the function $q = q\left(T, \frac{dT}{dt}\right)$, which can be substituted into (11) as the approximate value of the heat influx from the insulation. Satisfactory accuracy can be obtained, for example, by selecting as the family $T_b(t)$ the values $T_b(t) = T_w(b, t)$ obtained from solution of problem (1), (2), (4), (5) for $q = 0$.

Another common insulation is the evacuated-multilayer type, in which the heat conduction along the layers is considerably greater than in the transverse direction. For example, the thermal conductivity of evacuated-barrier insulation along the layer, depending on the pressure in the insulation, is higher than the conductivity in the transverse direction by 10^3 — 10^4 times [7]. This implies that, in this case, the insulation temperature varies significantly along the x coordinate only in a thin layer immediately adjacent to the vessel wall. Specifying

the thickness δ_1 of this layer and neglecting the heat capacity of the insulation mass enclosed in this layer, we obtain from the heat balance condition at the layer surface the relation

$$\lambda_{11} \left(T_{11} \right) \left. \frac{\partial T}{\partial y} \right|_{y=0} = \frac{1}{L \delta_1} \int_0^L (T_{11} - T_W) \lambda_{11} \left(\frac{T_{11} + T_W}{2} \right) dx, \quad (18'')$$

which replaces the boundary condition (18) in the previously examined problem for the evacuated-powder insulation. The problem (16), (17), (18''), (19) can be solved together with (1), (2), (4) — (9), (11), (13) — (15).

The following technique is used in constructing the algorithm for solving the system (1), (2), (4), (5) — (9). If we assume that (8) and (9) can be solved for the velocities in the bounding sections, then using the equation of state $\rho = \rho(p, T)$ and the two boundary conditions (8) and (9), after integrating the left and right sides of (1) with respect to the coordinate in the limits $0 \rightarrow l$, we obtain a relation which is convenient for calculating the pressure $p(t)$ [5]

$$\frac{dp}{dt} = \frac{(\rho u F)_{x=0} - (\rho u F)_{x=l} - \int_0^l \left[J + F \left(\frac{\partial \rho}{\partial t} \right)_p \frac{\partial T}{\partial t} \right] dx}{\int_0^l F \left(\frac{\partial \rho}{\partial p} \right)_T dx}. \quad (21)$$

Since it is not possible in the general case to obtain an exact solution of this problem, a numerical solution method was developed using the finite difference apparatus. The considered interval of the x axis was broken down into N elements with step equal to h . The finite step τ was taken with respect to time. For each moment of time $t_k = k\tau$, $k = 0, 1, 2, \dots, M$, we sought the value of the unknown functions at each point of the region $x_m = mh$, $m = 0, 1, 2, \dots, N$. We introduce the notations for the arbitrary function $y(x, t)$

$$\begin{aligned}\hat{y} &= y(x_m, t_k + \tau); \quad \check{y} = y(x_m, t_k - \tau); \quad \overset{+}{y} = y\left(x_m + \frac{1}{2}h, t_k\right); \\ \bar{y} &= y\left(x_m - \frac{1}{2}h, t_k\right) \\ y_t &= (\hat{y} - y)/\tau; \quad y_{\bar{t}} = (y - \check{y})/\tau \\ y_x &= (y(x_m + h) - y(x))/h; \quad y_{\bar{x}} = (y(x_m) - y(x_m - h))/h.\end{aligned}$$

195

We replace the relations (1), (2), (11), (8), (9) by differences and consider (21) an ordinary differential equation in the pressure $p(t)$, whose right side depends on the values of the functions on the difference grid appearing therein

$$T_t = -\frac{U}{F} \hat{T}' + \frac{P\alpha}{F\rho c_p} (T_{\bar{w}} - \hat{T}) + \frac{\overset{+}{\lambda} F \hat{T}_x - \bar{\lambda} F \hat{T}_{\bar{x}}}{F\rho c_p h} + \frac{T}{\rho^2 c_p} \left(\frac{\partial \rho}{\partial T} \right)_p P_t, \quad (22)$$

where

$$\hat{T}' = \begin{cases} \hat{T}_{\bar{x}} & \text{for } U \geq 0, \\ T_x & \text{for } U < 0; \end{cases}$$

$$T_{\bar{w}} = \frac{P\alpha}{\rho_w F_w c} (\hat{T} - \hat{T}_w) + \frac{q}{\rho_w F_w c} + \frac{\overset{+}{\lambda}_w F_w \hat{T}_{wx} - \bar{\lambda}_w F_w \hat{T}_{\bar{w}\bar{x}}}{F_w \rho_w c h}; \quad (23)$$

$$P_t = \frac{(\rho U)_{x=0} - (\rho U)_{x=Nh} - h \sum_{m=0}^N \left[J + F \left(\frac{\partial \rho}{\partial T} \right)_p T_t \right]}{h \sum_{m=0}^N F \left(\frac{\partial \rho}{\partial p} \right)_T}, \quad (24)$$

where

$$\begin{aligned}\rho &= \rho(p, \hat{T}); \\ (U\rho)_{\bar{x}} &= -F\rho_{\bar{t}} + J, \\ \rho &= \rho(\bar{p}, \hat{T}).\end{aligned} \quad (25)$$

The conditions (5) — (9), (14), (15) are replaced similarly by difference relations. The resulting system (22) — (25) with the boundary conditions represented in difference form is solved

as follows. Having the values of all the variables on the k^{th} time layer, we find from (22) by the "marching" method, the temperature distribution in the gas at the $(k + 1)^{\text{th}}$ layer. Here we use the wall temperatures, gas density and velocity, and time derivative of the pressure taken from the k^{th} layer,

Using the calculated gas temperatures, we find from (23) the temperature distribution in the wall at the $(k + 1)^{\text{th}}$ layer,

Equation (24) is considered an ordinary differential equation in the unknown function $p(t)$ with use of the gas and wall temperatures calculated at the $(k + 1)^{\text{th}}$ layer. The solution of this equation on the time interval (t_k, t_{k+1}) is sought by the Runge-Kutta method with time step τ/j , where j is an integer.

The necessity for using a more exact method with smaller time step for solving (24) is associated with the fact that the characteristic time scale for the processes which determine the pressure variation (basically the variation of the discharge characteristics at the boundary) is considerably shorter than the characteristic heat transfer process scale.

After determining the pressure, we find from (25) the velocity distribution at the $(k + 1)^{\text{th}}$ layer.

As an example of application of the described method, we consider the process of filling a vessel with a cryogenic liquid, characterized by the fact that the vessel wall temperature is considerably higher than the temperature of the incoming liquid. Therefore, the liquid boils intensely as it enters the vessel. The resulting vapor cools the vessel walls and the liquid gradually

fills the vessel and completes the wall cooling process. We assume that, as a result of intense agitation, the liquid temperature is the same throughout the volume and equal to the boiling temperature corresponding to the pressure in the vessel.

196

In accounting for heat transfer, the heat transfer coefficients were introduced into the calculation as follows. For the heat transfer from the gas to the wall, we took as the basis the relation for free turbulent convection at a vertical wall [9]. The heat transfer coefficient calculated from this relation was multiplied by a correction factor varying linearly from two in the interface region to one at the top of the vessel. The heat transfer coefficients for liquid boiling were calculated using the Kutateladze relation for nucleate boiling and using the Breen-Westwater relation [10] for film boiling. In the transient regime zone, the heat transfer coefficient was calculated on the basis of the assumption that the logarithm of the heat flux density in this zone varies linearly as a function of the logarithm of the difference between the wall temperature and the saturation temperature.

The formulation of the boundary conditions (6) — (9) corresponding to this problem can be found in [6].

We shall present the results of calculation of the process of filling an experimental vessel with liquid nitrogen with flow rate 260 liters/hour. Figure 2 shows the curves obtained as a result of calculation of the temperature variation at five wall points located at different levels and at points located in the gas region at the same levels, and also the corresponding experimental data obtained at the State Institute of Applied Chemistry. Figure 2a shows the calculated liquid level variation as a function of time in comparison with the experimental results.

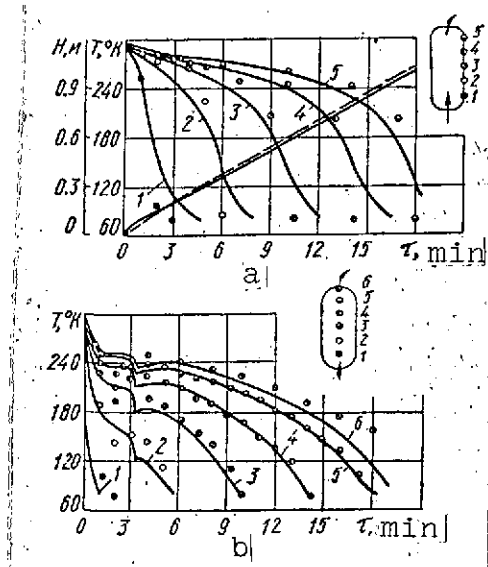


Figure 2. Temperature variation in vessel wall (a) and gas region (b) when filling with liquid nitrogen.

The numbers correspond to the vessel sections (solid curves are computed values, points are experimental data).

The liquid losses in evaporation during filling amounted to 6.69 kg according to the calculation, which differs by 3% from the experimental result.

Let us examine application of the proposed model to calculation of the process of cryogenic liquid pressure transfer from a vessel. As indicated above, the pressure transfer process consists in creating above the surface of the liquid in the vessel a differential pressure which acts on the liquid as a piston, forcing the liquid from the vessel. A particular case of this process is pressurization, when the liquid is not removed from the vessel but the differential pressure obtained in the vessel at the initial moment is maintained for a definite time interval.

Usually we are required to determine either the gas flow rate necessary to maintain the pressure in the given regime or for a specified flow rate (or for given connection between flow rate and pressure) of the gas supplied to the vessel determine the pressure in the vessel as a function of time. In either case, we can consider that the incoming gas temperature is known.

As the gas enters the vessel, it exchanges heat with the walls, to the outer surface of which heat is applied from the surrounding medium through the insulation.

We assume that, as the pressure in the vessel changes, a temperature equal to the saturation temperature corresponding to this pressure is established instantaneously at the gas-liquid interface. Therefore, phase transformations may take place at the interface. The direction of these processes (i.e., whether the gas condenses or the liquid evaporates) depends on the relationship between the thermal flux supplied to the interface through the gas space and the thermal flux removed into the liquid.

We assume that, during the pressure transfer time, the liquid does not boil, since the pressure increase in the vessel leads to a situation in which the liquid is overcooled in relation to the saturation temperature corresponding to this pressure. If the wall temperature becomes lower than the saturation temperature corresponding to the pressure in the vessel, gas condensation may take place at the wall. In this case, the corresponding wall segment is covered by a draining liquid film. Here we shall consider that the heat released during condensation is all absorbed by the wall and the gas yields heat to the film convectively.

Under pressure transfer conditions, the condensing vapor may be superheated and the relations describing heat transfer during condensation of saturated vapor may yield a large error.

Knowing the condensate film thickness, we can calculate the heat transfer and, at the same time, the mass removal J . In the following, we assume the generalized Nusselt model [8], describing superheated vapor condensation on a vertical wall.

Taking the basic assumptions of the Nusselt model but considering the thermal flux supplied from the vapor to the film, for description of the process of film flow on the vertical

wall, we can write the equations of momentum, energy, and mass conservation, directing the x axis vertically downward and the y axis along the normal to the wall

$$\eta \frac{\partial^2 w}{\partial y^2} = -\rho_l g; \quad (26)$$

$$\frac{d^2 \theta}{dy^2} = 0; \quad (27)$$

$$\frac{d(\rho_l \bar{w} \delta)}{dx} = \dot{m}; \quad (28)$$

$$\dot{m}r = \frac{\lambda l}{\delta} (T_s - T_w) - \alpha (T - T_s). \quad (29)$$

Here w is the flow velocity in the condensate film; \bar{w} is its average value; θ is the temperature in the condensate film; T_s is the saturation temperature; r is the heat of vaporization; \dot{m} is the mass flow rate in phase transformations.

After suitable transformations, the film thickness $\delta(x)$ may be determined from the equation

$$\delta^3 \frac{d\delta}{dx} = a(x) \delta + b(x), \quad (30)$$

where

$$a(x) = \frac{-\alpha \eta}{r \rho_l^2 g} (T - T_s); \quad b(x) = \frac{\lambda l \eta}{r \rho_l^2 g} (T_w - T_s).$$

Generally speaking, the solution of (30) does not reduce to quadratures. In the numerical solution of this equation, complications may arise associated with the fact that the point (0, 0) for (30) is singular (the coefficient of the derivative

vanishes — the initial conditions are specified at the point $x = 0$, at which $T_w = T_s$ and it is assumed that $\delta(0) = 0$).

Analysis of the problem shows that (30) has two solutions passing through the singular point. One of them has an infinite derivative at zero and must be discarded, since it leads to negative film thickness values.

The second solution has a finite derivative and for small values of ξ may be written in the form /98

$$\delta(\xi) \approx F(\xi) - [F'(0)]^2 \xi^3, \quad (31)$$

where

$$\xi = \int_0^x d(x) dx, \quad J(\xi) = -\frac{\delta[x(\xi)]}{d[x(\xi)]}.$$

We shall solve (30), taking as the initial thickness its value calculated using (31), and then apply the finite difference method. This model is applied to the pressure transfer process as follows.

Solving (30) together with (1), (2), (4) — (15), we find the coefficient of heat transfer to the wall in the condensation zone $\alpha_{\text{con}} = \lambda_l / \delta$ and at the same time, we find the specific mass removal from the gas region

$$J = \frac{\lambda_l [\delta(T_s - T_w)] - \alpha(T - T_s)}{r}. \quad (32)$$

The calculation sequence is as follows: at each time step, we determine the zone where the wall temperature T_w is below the saturation temperature T_s . We use (31) to find the initial film thickness σ_0 . The space step h [in (22) — (25)] is broken down into L parts and the film thickness at the nodes of the basic

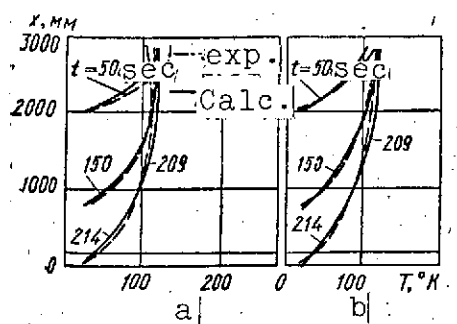


Figure 3. Temperature distribution in gas (a) and wall (b) in the case of pressure transfer of liquid hydrogen from a vessel.

grid on the condensation segment is found by the "predictor-corrector" finite-difference method with step h/L . After this, we find α_{con} and J . Formulation of the initial and boundary conditions is made on the basis of the assumptions presented above and is described in [6].

As an example, we present the results of calculation of the process of liquid hydrogen pressure transfer by gaseous hydrogen from a vessel having the form of a vertical cylinder of diameter 0.8 meters and height 2.85 meters. The vessel material is the AZ5G aluminum alloy, the wall thickness is 0.001 meter. The experiment was described in [12]. The calculation is compared with the data of experiment No. 11 of [12]. The initial temperature distribution in the gas and wall was not indicated in the description of the experiment.

The gas temperature at the entrance to the vessel varied in quite wide limits. The temperature variation law is not known. The liquid flow rate also varied during the pressure transfer process. As the initial values in the calculation, we took uniform temperatures of 35 and 20.4° K in the gas and the wall, respectively.

The gas temperature at the entrance was considered to be constant and equal to 116° K, which is the average value of the three entrance temperature values indicated on the experimental curves.

Figure 3 shows curves of the temperature distribution in the gas and wall at 50, 150, and 214 seconds after process initiation from the experimental (dashed lines) and calculated (solid lines) data. In spite of the indeterminacy noted above in the initial values, the comparison results are quite acceptable.

On the basis of this discussion, we can draw the following conclusions.

The subject technique for calculating the processes of pressurization, pressure transfer, and filling of a vessel with a cryogenic liquid is quite satisfactory, as indicated by comparison of the calculated and experimental data. The method may be used to calculate the hydrodynamic and heat transfer processes in the case of concurrent separate flow of cryogenic liquid and vapor when the flow velocity is significantly lower than the speed of sound. Of significant importance in the calculation is /99 the choice of the relations describing the heat transfer processes with boiling of the liquid and gas interaction with the wall. Therefore, refinement of these relations for specific processes in order to compare the calculated and experimental data is very important, and the conduct of special calculations of two-dimensional (axisymmetric) models from which we can find the heat transfer coefficients directly is also urgent.

REFERENCES

1. Clark, J. A. Adv. in Cryog. Eng., Vol. 10, 1965, p. 259.
2. Jacobs, R. B. Adv. in Cryog. Eng., Vol. 8, 1963, p. 529.
3. Zhitomirskiy, I. S., L. L. Al'tshuler, and I. V. Saychuk. In the book: Teplo- i massoperenos (Heat and Mass Transfer), Vol. 4, Minsk, 1968.

4. Pestryakov, A. A., P. G. Makedonskaya, and L. A. Ishchenko.
In the book: Teplo- i massoperenos, (Heat and Mass
Transfer), Vol. 1. Moscow, Energiya Press, 1968.
5. Zhitomirskiy, I. S., L. A. Ishchenko, and V. A. Pestryakov.
In the book: Voprosy gidrodinamiki i teploobmena v
kriogennykh sistemakh (Hydrodynamics and Heat Transfer
in Cryogenic Systems), Vol. 1, Kharkov, 1970.
6. Zhitomirskiy, I. S., and V. A. Pestryakov. In the book:
Voprosy gidrodinamiki i teploobmena v kriogennykh
sistemakh (Hydrodynamics and Heat Transfer in Cryogenic
Systems), Vol. 1, Kharkov, 1970.
7. Lebedev, D. P., Ye. K. Zlobin, and V. V. Alekseyev. IFZh,
Vol. 21, No. 5, 1971.
8. Grober, H., S. Erk, and U. Grigull. Fundamentals of
Heat Transfer. Moscow, Foreign Literature Press, 1958.
9. McAdams, W. H. Heat Transmission. Moscow, Metallurgizdat
Press, 1961.
10. Brentari, E. G., and R. V. Smith. Adv. in Cryog. Eng.,
Vol. 10, 1965, p. 325.
11. Epstein, M., H. K. Georgins, and R. E. Anderson. Int,
Adv. in Cryog. Eng., Vol. 10, 1965, p. 290.
12. Bourgarel, M., K. Clement, and M. Segel, Proc. Sec.
Intern. Cryogenic Eng. Conf. Brighton, United Kingdom,
1968, 89.
13. Zhitomirskiy, I. S., et al. In the book; Voprosy gidro-
dinamiki i teploobmena v kriogennykh sistemakh (Hydro-
dynamics and Heat Transfer in Cryogenic Systems), Vol. 2,
Kharkov, 1971.

Translated for National Aeronautics and Space Administration
under Contract No. NASw-2483, by SCITRAN, P. O. Box 5456,
Santa Barbara, California 93108.